UNIVERSITÉ DE MONTRÉAL

TRIBO-MECHANICAL AND ELECTRICAL PROPERTIES OF BORON-CONTAINING COATINGS

JINCHENG QIAN

DÉPARTEMENT DE GÉNIE PHYSIQUE

ÉCOLE POLYTECHNIQUE DE MONTRÉAL

THÈSE PRÉSENTÉE EN VUE DE L'OBTENTION

DU DIPLÔME DE PHILOSOPHIÆ DOCTOR

(GÉNIE PHYSIQUE)

MARS 2015

UNIVERSITÉ DE MONTRÉAL

ÉCOLE POLYTECHNIQUE DE MONTRÉAL

Cette thèse intitulée:

TRIBO-MECHANICAL AND ELECTRICAL PROPERTIES OF BORON-CONTAINING COATINGS

présentée par : QIAN Jincheng

en vue de l'obtention du diplôme de : Philosophiæ Doctor

a été dûment acceptée par le jury d'examen constitué de:

M. YELON Arthur, Ph. D., président

Mme KLEMBERG-SAPIEHA Jolanta-Ewa, Doctorat, membre et directrice de recherche

M. ZHANG Wenjun, Ph. D., membre et directeur de recherche

M. MARTINU Ludvik, Ph. D., membre et codirecteur de recherche

M. WANG Zuankai, Ph. D., membre

M. MEUNIER Jean-Luc, Ph. D., membre externe

M. WANG Ning, Ph. D., membre externe

UNIVERSITÉ DE MONTRÉAL

ÉCOLE POLYTECHNIQUE DE MONTRÉAL

Tribo-Mechanical and Electrical Properties of Boron-Containing Coatings

Submitted to

Département de Génie Physique

École Polytechnique de Montréal

in Partial Fulfillment of the Requirements

for the Degree of Doctor of Philosophy

awarded by École Polytechnique de Montréal

for successful completion of the joint programme with

City University of Hong Kong

by

JINCHENG QIAN

March 2015

DEDICATION

To my parents and grandmother.

ACKNOWLEDGMENTS

This thesis work resulted from the double-diploma Ph.D. program under cotutelle between City University of Hong Kong and École Polytechnique de Montréal. A lot of people's efforts helped to initiate this program, and many people helped my work.

First, I would like to thank my four supervisors. Professors Wenjun Zhang and Igor Bello gave me the opportunity of starting my Ph.D. study at CityU. Professors Jolanta Sapieha and Ludvik Martinu brought me the opportunity of joining this double-diploma Ph.D. program and of studying at Polytechnique. I am grateful for all their guidance, patience and support throughout my Ph.D. study. They are always there to help and encourage me when I have difficulties and feel confused. Their attitudes towards research and life influenced me significantly both on professional and personal levels. I am blessed to meet these four great persons in my life.

I would like to extend my gratitude to all the members of COSDAF at CityU and of FCSEL at Polytechnique, particularly to Shrawan Jia, Yan Ce, Chen Zhenhua, Wang Hongen, Liu Chaoping, Karen Ng at COSDAF, to Etienne Bousser, Thomas Schmitt, Oleg Zabeida, Duanjie Li, and Marwan Azzi at FCSEL, and to others I did not mention here. I am thankful to the technicians Felix Wong at COSDAF and Sébastien Chenard and Francis Turcot at FCSEL. I would not finish my projects without your technical support.

I would like to give my special thanks to Prof. Lawrence Li (from MEEM CityU) for providing the magnetron sputtering deposition system and to Dr Zhifeng Zhou for his assistance on the coating deposition. I would like to thank all the co-authors of my papers; I really enjoyed the collaboration.

I would also like to thank Prof J. A. Zapien, Ms. Line Dubé, and Ms. Nathalie M. Pelletier who helped this double-diploma Ph.D. program work.

Last but not least, I sincerely thank my parents and my husband Mr. Zuo Dawei, who have been supporting me all the time. Thank you for all your love, understanding, and company in my life.

RÉSUMÉ

Le développement de nouveaux revêtements protecteurs durs ayant une performance de pointe est très important pour le progrès scientifique relié à de plusieurs domaines industriels. L'application de revêtements protecteurs durs peut augmenter significativement la performance de pièces et composantes, étendre leur durée de vie ainsi que sauver de l'énergie dans maintes industries incluant l'aérospatial, l'automobile, les manufactures et bien d'autres. De plus, la multifonctionnalité des revêtements représente une valeur ajoutée dans d'autres domaines tels que l'optique, la microélectronique, le biomédical, le stockage magnétique de données, etc. Ainsi, les revêtements protecteurs avec des propriétés tribo-mécaniques améliorées et une résistance à la corrosion augmentée sont très en demande.

Les caractéristiques des revêtements peuvent être ajustées en contrôlant leur microstructure sur une échelle répandue dans différents ordres de grandeur. Par exemple, les films avec des nanostructures, comme les super-réseaux, les nanocolonnes et les systèmes nanocomposites, montrent des caractéristiques très distinctes par rapport aux matériaux à une seule phase. Ils montrent des propriétés tribo-mécaniques supérieures grâce à la présence d'interfaces internes rigides et différentes fonctions peuvent être accomplies avec un matériau multi-phase.

Les matériaux contenant du bore ont d'excellentes propriétés mécaniques et des caractéristiques électroniques très intéressantes, ce qui en fait de bons candidats pour les revêtements protecteurs fonctionnels durs. Par exemple, le nitrure de bore cubique (*c*-BN), le carbure de bore ($B_{1-x}C_x$) et le diborure de titane (TiB_2) sont très connus pour leur grande dureté, leur haute stabilité thermique et leur caractère chimique inerte. Un exemple intéressant est le nitrure de carbure de bore (BCN) qui possède plusieurs propriétés attrayantes grâce à la similarité structurale avec le carbone (graphite et diamant) ainsi que le nitrure de bore (BN en phase hexagonal ou cubique).

L'objectif principal de cette recherche est de développer plus en détail la famille de revêtements contenant du bore, incluant le $B_{1-x}C_x$, le Ti−B−C et le BCN déposés par pulvérisation magnétron, pour améliorer leur performance sur mesure et obtenir de nouvelles fonctions en contrôlant leur microstructure à l'échelle nanométrique. Leurs propriétés tribo-mécaniques, leur résistance à la corrosion ainsi que leurs propriétés électriques sont étudiées en relation avec la composition et la microstructure, en gardant toujours en mire l'amélioration de

leur performance pour des revêtements multifonctionnels protecteurs par la conception de microstructures.

Premièrement, des revêtements $B_{1-x}C_x$ ($0 < x < 1$) avec des propriétés tribo-mécaniques adaptées ont été déposées par pulvérisation magnétron en utilisant une cible de graphite et deux de bore. La dureté du revêtement de $B_{1-x}C_x$ a été mesurée à 25 GPa, soit la même dureté pour ceux composé à majorité de bore ou de carbone, alors que le coefficient de friction et le taux d'érosion peuvent être ajustés respectivement de 0,66 à 0,13 et de $6{,}4\times10^{-5}$ mm^3/Nm à $1{,}3\times10^{-7}$ mm^3/Nm, en changeant la proportion de carbone de 19 % à 76 % atomique. La variation de dureté est étroitement liée à la microstructure alors que le coefficient de friction faible et le taux d'érosion réduit du $B_{0.24}C_{0.76}$ sont causés par une plus grande proportion de la phase de carbone amorphe. Aussi, l'application du revêtement $B_{0.81}C_{0.19}$ améliore significativement la résistance à la corrosion de l'acier M2, indiqué par la chute du courant de corrosion de presque quatre ordres de grandeur.

Basé sur l'optimisation des revêtements $B_{1-x}C_{x,}$ des revêtements nanostructurés de Ti−B−C avec différentes compositions ont été déposés en ajoutant du titane par la pulvérisation simultanée d'une cible de diborure de titane. Nous avons trouvé que la microstructure du revêtement consiste en des nanocristaux de TiB_2 insérés dans une matrice de carbure de bore amorphe. La dureté du revêtement varie de 33 à 42 GPa avec différentes concentrations de titane, ce qui est relié au changement de microstructure, particulièrement à la grandeur et à la concentration des nanocristaux de TiB_2. Le coefficient de friction et le taux d'érosion varient respectivement entre 0,37 et 0,73 ainsi que $3{,}3\times10^{-6}$ et $5{,}7\times10^{-5}$ mm^3/Nm, ce qui est affecté par les propriétés mécaniques et l'état chimique de la surface. En appliquant le revêtement de Ti−B−C, la résistance à la corrosion de l'acier M2 a augmenté significativement, comme démontré par la réduction du courant de corrosion de deux ordres de grandeur.

Les revêtements de BCN ont été produits par pulvérisation magnétron avec une simple cible de B_4C dans une atmosphère de N_2: Ar. Le revêtement de BCN a une structure amorphe et contient un mélange de liens B−C, B−N et C−N. Il montre une conductivité de type p avec une bande interdite optique de 1,0 eV. Par la suite, des nanotiges de ZnO ont été produites sur le revêtement de BCN en utilisant une synthèse hydrothermique pour former des nanotiges de BCN/ZnO en hétérojonctions p-n. La performance de ces jonctions est évaluée par la

caractérisation *I-V*, qui montre une rectification du comportement avec un ratio de 1500 à un voltage en bias de ±5V.

ABSTRACT

The development of new hard protective coatings with advanced performance is very important for progress in a variety of scientific and industrial fields. Application of hard protective coatings can significantly improve the performance of parts and components, extend their service life, and save energy in many industrial applications including aerospace, automotive, manufacturing, and other industries. In addition, the multifunctionality of protective coatings is also required in many other application fields such as optics, microelectronics, biomedical, magnetic storage media, etc. Therefore, protective coatings with enhanced tribo-mechanical and corrosion properties as well as other functions are in demand.

The coating characteristics can be adjusted by controlling the microstructure at different scales. For example, films with nanostructures, such as superlattice, nanocolumn, and nanocomposite systems, exhibit distinctive characteristics compared to single-phase materials. They show superior tribo-mechanical properties due to the presence of strong interfaces, and different functions can be achieved due to the multi-phase characteristics.

Boron-containing materials with their excellent mechanical properties and interesting electronic characteristics are good candidates for functional hard protective coatings. For instance, cubic boron nitride (*c*-BN), boron carbide ($B_{1-x}C_x$), and titanium diboride (TiB_2) are well known for their high hardness, high thermal stability, and high chemical inertness. An interesting example is the boron carbon nitride (BCN) compound that possesses many attractive properties because its structure is similar to that of carbon (graphite and diamond) and of boron nitride (BN in hexagonal and cubic phases).

The main goal of this work is to further develop the family of Boron-containing films including $B_{1-x}C_x$, Ti−B−C, and BCN films fabricated by magnetron sputtering, and to enhance their performance by controlling their microstructure on the nanoscale. Their tribo-mechanical, corrosion, and electrical properties are studied in relation to the composition and microstructure, aiming at enhancing their performance for multi-functional protective coating applications via microstructural design.

First, $B_{1-x}C_x$ ($0 < x < 1$) films with tailored tribo-mechanical properties were deposited by magnetron sputtering using one graphite and two boron targets. The hardness of the $B_{1-x}C_x$ films

was found to reach 25 GPa both for boron-rich and carbon-rich films, and the friction coefficient and wear rate can be adjusted from 0.66 to 0.13 and from 6.4×10^{-5} mm^3/Nm to 1.3×10^{-7} mm^3/Nm, respectively, by changing the carbon content from 19 to 76 at.%. The hardness variation is closely related to the microstructure, and the low friction and wear rate of the $B_{0.24}C_{0.76}$ film are due to the high portion of an amorphous carbon phase. Moreover, application of the $B_{0.81}C_{0.19}$ film improves the corrosion resistance of the M2 steel substrate significantly, indicated by the decrease of the corrosion current by almost four orders of magnitude.

Based on the optimization of the $B_{1-x}C_x$ films, nanostructured Ti−B−C films with different compositions were deposited by adding titanium by simultaneously sputtering a titanium diboride target. We found that the film microstructure features TiB_2 nanocrystallites embedded in an amorphous boron carbide matrix. The film hardness varies from 33 to 42 GPa with different titanium contents, which is related to the changes in microstructure, namely, the size and concentration of the TiB_2 nanocrystallites. The friction coefficient and wear rate are in the ranges of 0.37−0.73 and of 3.3×10^{-6}−5.7×10^{-5} mm^3/Nm, respectively, which are affected by the mechanical properties and the surface chemical states of the films. By applying the Ti−B−C films, the corrosion resistance of the M2 steel substrate is significantly enhanced as documented by a reduction of the corrosion current density by two orders of magnitude.

BCN films were synthesized by magnetron sputtering using a single B_4C target in an N_2: Ar gas mixture. The BCN films exhibit an amorphous structure and contain a mixture of B−C, B−N, and C−N bonds. The films show p-type conductivity with an optical band gap of 1.0 eV. Subsequently, ZnO nanorods were grown on the BCN films using hydrothermal synthesis to form BCN/ZnO nanorods p-n heterojunctions. The performance of the junctions is evaluated by the *I-V* characterization, which shows a rectification behavior with a rectification ratio of 1500 at the bias voltages of ±5 V.

TABLE OF CONTENTS

LIST OF TABLES

LIST OF FIGURES

LIST OF ACRONYMS AND SYMBOLS

Abbreviations:

a-C	Amorphous carbon
a-C:H	Hydrogenated diamond-like carbon
$AlMgB_{14}$	Aluminum magnesium boron
a-Si_3N_4	Amorphous silicon nitride
$B_{1-x}C_x$	Boron carbide
B_2O_3	Boron oxide
BCN	Boron carbon nitride
BE	Binding energy
Boron-containing	B-containing
c-BN	Cubic boron nitride
c-BCN	Cubic boron carbon nitride
CE	Counter electrode
CN_x	Carbon nitride
COSDAF	Centre of Super-Diamond and Advanced Films
CVD	Chemical vapor deposition
DC	Direct current
DLC	Diamond-like carbon
EDS	Energy dispersive X-ray spectrometry
FCSEL	Functional Coating and Surface Engineering Laboratory
FESEM	Field emission scanning electron microscope
FTIR	Fourier transform infrared spectroscopy
FWHM	Full width at half maximum
GDP	Gross domestic product
H_3BO_3	boron acid
h-BCN	Hexagonal boron carbon nitride
h-BN	Hexagonal boron nitride
HDI	Head-disk interfacial
HPHT	High pressure and high temperature

HVOF	High velocity oxy-fuel
KE	Kinetic energy
NACE	National Association of Corrosion Engineers
nc-TiN	Nanocrystalline titanium nitride
OCP	Open circuit potential
PECVD	Plasma enhanced chemical vapor deposition
PLD	Pulsed laser deposition
PVD	Physical vapor deposition
RBS	Rutherford backscattering spectroscopy
RE	Reference electrode
RF	Radio frequency
RH	Relative humidity
RT	Room temperature
SCE	Standard calomel electrode
SEM	Scanning electron microscopy
SZM	Structure zone model
ta-C	Tetragonal carbon
TiB_2	Titanium diboride
TM	Transition metal
TiN_x	Titanium nitride
UHV	Ultrahigh vacuum
WE	Working electrode
XANES	X-ray absorption near-edge spectroscopy
XPS	X-ray photoelectron spectroscopy
XRD	X-ray diffraction
ZnO	Zinc oxide
ZnO NRs	Zinc oxide nanorods

Symbols

a	Lattice constant
A	Projected contact area
at.%	Atomic percent
B	Fitting constant in Oliver and Pharr model
c	Lattice constant
c_{crack}	Length of radial crack
d	Interplanar spacing
d_g	Grain size
E	Young's modulus
E^*	Normalized delivered energy flux
E_{BD}	Breakdown potential
E_i	Elastic modulus of indenter
E_r	Reduced modulus
E_s	Elastic modulus of sample
F	Frictional force
H	Hardness
h	Planck's constant
h_{depth}	Indentation depth
h_{max}	Maximal penetration depth
h_r	Depth of residual impression
I	Current
I_0	Saturation current
i_{corr}	Corrosion current density
I_i	XPS peak intensity
J_{Ar+}	Incident Ar ion flux
J_{Ti}	Ti flux
K	Wear rate
k	Boltzmann constant
k_1	Hall-Petch material constant
K_c	Fracture toughness

m	Fitting constant in Oliver and Pharr model
n	Ideality factor
n_1	Integer
P	Applied load
P_{max}	Maximum indentation load
q	Electronic charge
r	Contacting sphere radius
R	Elastic recovery
s	Sliding distance
S	Stiffness
S_i	Sensitivity factor
T	Absolute temperature
T^*	generalized substrate temperature
T_a	Annealing temperature
T_m	Melting point
T_s	Subsrate temperature
U_s	Substrate bias
V	Voltage
V_{loss}	Volume loss
V_t	Thermal voltage
W_e	Energy due to elastic deformation
W_p	Energy due to plastic deformation
wt.%	Weight percent
X_i	Atomic concentration

Greek symbols

α	Absorption coefficient
α_1	Empirical constant related to the indenter geometry
Γ	Full width at half maximum intensity
$\Delta\upsilon$	Frequency difference
ε	Strain
θ	Diffraction angle
λ	X-ray wavelength
λ_{period}	Superlattice period
μ	Friction coefficient
$\overline{\mu}$	Mean friction coefficient
ν	Frequency of the photon
ν_{i}	Poisson's ratio of indenter
ν_{s}	Poisson's ratio of sample
ν_{vib}	Vibrational frequency of a molecule
σ	Stress
σ_0	Intrinsic yield stress
σ_{prop}	Proportionality limit
σ_{y}	Yield strength
υ	Vibrational quantum number
$\Phi_{\text{spectrometer}}$	Work function of the spectrometer

CHAPTER 1 INTRODUCTION

1.1 Hard protective coatings

Hard protective coatings are generally applied on the surfaces of bulk materials with the intention of protecting them from damage or failure. The development of hard protective coatings is increasingly stimulated by the demands for enhanced surface tribo-mechanical properties of parts and components in various fields of application such as automotive, aerospace, microelectronics, and numerous others. More than $1 trillion USD (6.1% of the GDP) were lost as a result of corrosion in the USA in 2013 according to the report from NACE (National Association of Corrosion Engineers) [1]. In addition, one-third of the fuel energy is used to overcome the friction in engines, transmissions, tires, and brakes in passenger cars. For instance, around 360 million tons of oil was consumed globally in relation to friction in passenger cars in 2009 [2]. Such losses can be significantly reduced by applying hard protective coatings with improved tribo-mechanical and corrosion properties [3-7].

Chemical vapor deposition (CVD) and physical vapor deposition (PVD) are two important techniques extensively employed for hard protective coating fabrications [8-11]. The non-equilibrium nature of the deposition processes makes it possible to change the film properties by tuning the composition and the microstructure. Historically, the first CVD processes were developed for applications such as cutting tools [12]. This was followed by PVD; nowadays, arc deposition and magnetron sputtering are widely used techniques for hard coating fabrication owing to the relative ease of compositional and structural control, low substrate temperature without harmful gases, and generally good film adhesion.

A typical structure of hard protective coatings is schematically shown in Figure 1.1 (a). In general, substrate surfaces are processed with appropriate treatments before deposition to remove surface contamination and to enhance substrate hardness in order to match the mechanical properties of the subsequently applied coatings. Commonly, an adhesion enhancement layer is used between the substrate and the coating. For example, duplex treatment is commonly used to improve interfacial adhesion. This process consists of two independent steps: surface treatment leading to surface hardening, usually accomplished by nitriding or carburizing, followed by the deposition of a protective layer, often including an adhesion layer [10]. The main coating can

possess different architectures or nanostructures as illustrated in Figure 1.1 (b). With appropriate design, the coating performance can be enhanced with respect to the tribo-mechanical, corrosion, and other properties to meet specific requirements (see Figure 1.2).

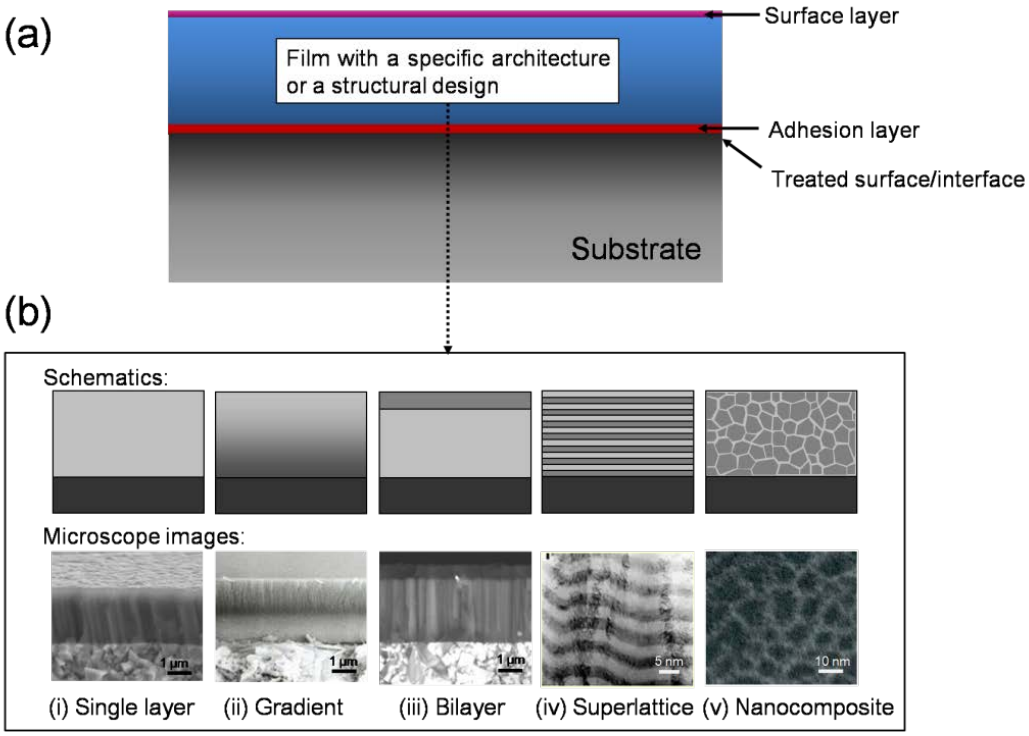

Figure 1.1 (a) Typical structure of hard protective coatings; (b) different architectures or nanostructures of coatings illustrated by the schematics and the corresponding microscope images.

Hard protective coatings with high wear resistance and high thermal stability have been extensively used on cutting tools for component machining. Application of such coatings, typically 3−5 µm thick, can enhance the durability of the tool, the machining speed, as well as the quality of the cutting process. Coatings of transition metal carbides and nitrides, such as TiC and TiN, are widely employed.

Components with strengthened and lubricious surfaces are required in the automotive industry. The very high energy consumption caused by friction can be reduced by applying coatings with low friction. In addition, the lifetime of components can be improved significantly by using hard and wear resistant coatings [2, 13]. For instance, diamond-like carbon (DLC) coatings have been successfully applied on different automotive parts such as piston rings to reduce friction, and hence to lower fuel consumption and enhance the overall efficiency [14, 15].

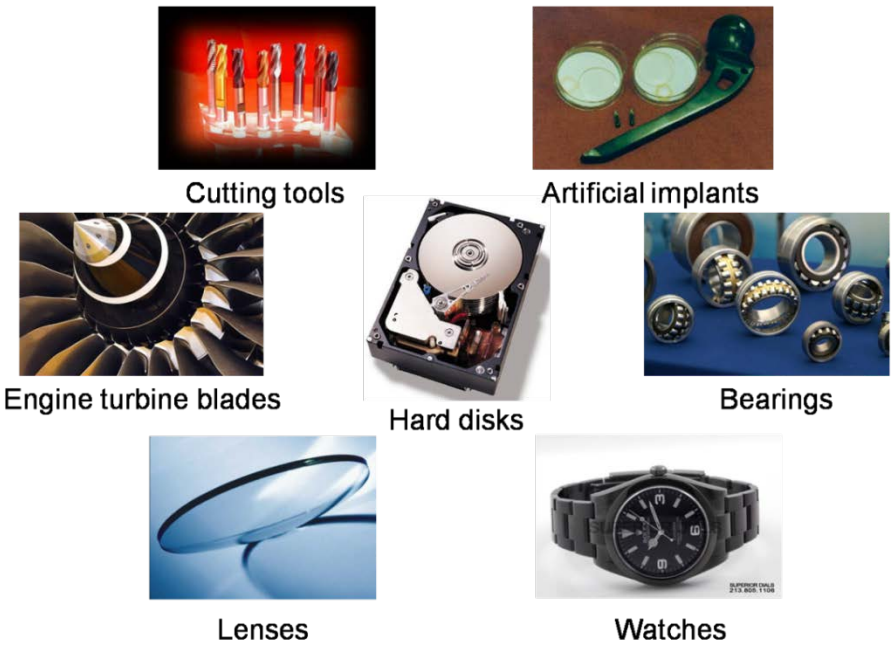

Figure 1.2 Examples of the applications of multi-functional protective coatings.

Protective coatings with multi-functional characteristics (see Figure 1.3) combining film properties, such as selective optical absorption, color, or electrical conductivity with the mechanical, tribological, and corrosion protection, open new applications in other areas including optics, microelectronics, biomedical, magnetic storage media, and consumer products as shown in Figure 1.2. Of particular interests are the following applications.

(i) Optics. Tribo-mechanical properties of the optical coatings on the components such as lenses or glass screens need to meet the minimum requirements to prevent damage such as scratches. In addition, optical coatings with very low permeability of moisture is also very important as the absorption of water vapor can significantly affect the optical characteristics and induce stress which may cause coating delamination and long term instability [16].

(ii) Biomedical applications. The protective coatings for biomedical devices such as artificial implants are required to possess low friction and high wear resistance. In addition, the coatings need to be biocompatible and withstand the effect of highly corrosive environments including body cells and fluids. DLC coatings meeting these requirements have been used to in such applications [17].

(iii) Magnetic storage media. Hard disks are usually coated with protective layers which can decrease the friction and wear of occasional head-disk contacts and the corrosion of the head and

of the magnetic media [18]. With the requirement of increasing the storage density, the thickness of the protective layers is limited by the head-disk interfacial (HDI) spacing. Therefore, smooth and dense coatings with enhanced tribo-mechanical and corrosion properties and high thermal stability such as DLC [19, 20] and carbon nitride (CN_x) [21, 22] are widely used in hard disks.

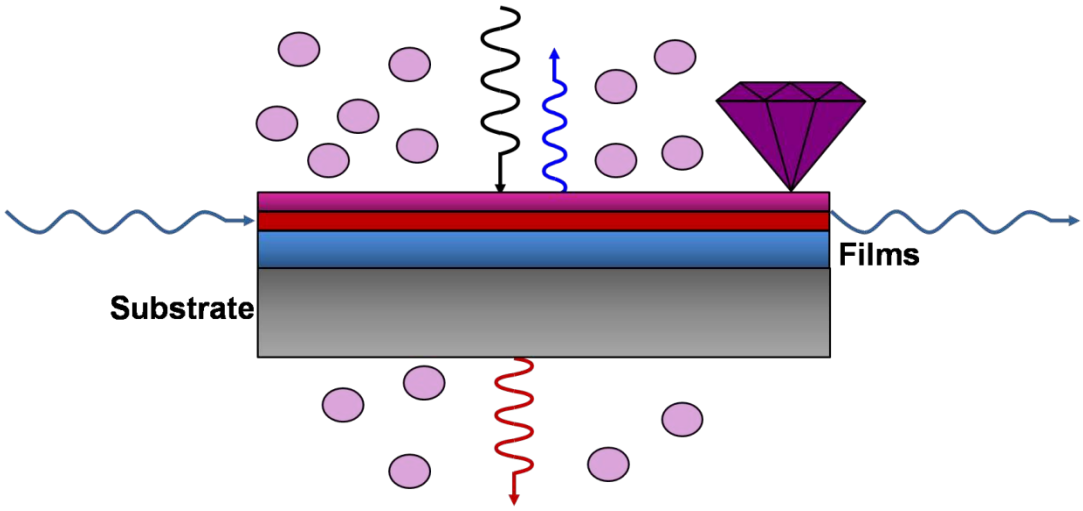

Figure 1.3 Schematic illustration of a functional coating system, modified from [23].

1.2 Motivation of the present work

It is very important to control the coating properties by the design of coating architecture and microstructure as illustrated in Figure 1.1 (b). Single layer coatings with homogeneous composition can provide primary protection of the substrate. However, the coating performance such as adhesion and strength can be further improved by applying different microstructures. For example, gradient coatings with gradual transitions of the coating properties across the thickness and without sharp interfaces exhibit adhesion superior to that of single layer coatings [24]. Moreover, strengthening of conventional materials following the Hall-Petch relationship [25] is limited when the grain size is close to 10 nm and below. This limitation can be overcome by developing nanostructured materials including superlattices and nanocomposites. Superlattice films consist of two different alternating layers with a period typically of 5−10 nm, whereas nanocomposite coatings are composed of nanocrystallites embedded in an amorphous or a nanocrystalline matrix. Both of these systems exhibit superior mechanical performance compared to single phase materials. This is generally explained by the increase of interface density. For superlattice films, sharp interfaces between alternating layers with different elastic moduli can

hinder dislocation movements and consequently enhance the mechanical properties. For nanocomposites, the strong interfaces between the different crystalline phases can prevent grain boundary sliding and hence achieve strengthening. However, it is still a challenge to determine more precise rules to control the film structure and properties. The main reason tends to be that the coating properties are determined by the structures at different scales, including the bonding states and the microstructure which are rather complex, and are affected by the many factors.

The development of new and novel protective coatings with high hardness, high wear resistance, and additional functions are strongly stimulated by the industrial demands such as extension of the part lifetime, energy-saving, cost reduction, and performance enhancement. Numerous materials, such as diamond, transition metal nitrides and carbides, and DLC have been used as protective coatings in different fields, but there are still numerous problems to be solved. For example, poor adhesion and high deposition temperature of diamond coatings restrict their application despite their high hardness of ~100 GPa. *c*-BN coatings with a hardness of 50−70 GPa are good candidates for hard protective coatings, but the high built-in compressive stress limits the applicable coating thickness and gives rise to poor adhesion. TiN is widely used as hard and wear resistant coating for cutting tools; however, the low oxidation resistance (< 500 ºC) restricts its high temperature applications. DLC films are very popular for automotive tribo-components and biomedical devices due to their relatively high hardness and elasticity, low friction, and low wear rate. However, their applications are limited by the low thermal stability (< 300 ºC) and frequently poor adhesion caused by high compressive stress.

1.3 Objectives

Boron-containing (B-containing) materials such as boron carbide ($B_{1-x}C_x$) and titanium diboride (TiB_2) are very attractive, due to their excellent mechanical properties. For example, B_4C with a hardness of ~40 GPa is the third hardest traditional bulk material at room temperature after diamond and *c*-BN. Its high thermal stability, up to 1700 K, makes it a good candidate for tribo-mechanical applications at high temperature. Its low mass density of 2.52 g/cm^3, low thermal expansion coefficient of 4.3×10^{-6} K^{-1}, high chemical stability, and good wear resistance make B_4C a suitable candidate for different industrial applications. For comparison, TiB_2 is a ceramic compound well known for its high hardness of ~30 GPa, high thermal conductivity of 96 W/mK, and chemical inertness. Moreover, the electronic characteristics of B-containing materials

are very interesting as well. Boron carbon nitride (BCN) exhibits adjustable optical and electrical properties due to its structural similarity to carbon (graphite and diamond) and boron nitride (BN in hexagonal and cubic phases). Therefore, the present thesis is primarily motivated by the prospects of the performance of B-containing materials in the form of thin films and coatings with the goal of providing attractive properties as hard protective coatings and multi-functionality, for example with their electrical and optoelectronics characteristics.

In relation to the above, the main objectives of this thesis can be formulated as follows: to develop hard B-containing nanocomposite protective coatings using magnetron sputtering, to enhance the coating performance by controlling the microstructure on the nanoscale including nanocomposite, nanocolumn, nanorod, and multilayer features, to study the effect of composition and microstructure on their tribo-mechanical and corrosion behaviors, and to explore their potential for new applications due to their multi-functional characteristics.

Specific objectives can be summarized as follows:

- To tailor the tribo-mechanical properties of boron carbide films via the $B_{1-x}C_x$ composition;
- To study the structural evolution and the tribo-mechanical properties by doping $B_{1-x}C_x$ with Ti to obtain Ti−B−C nanocomposite films;
- To develop high quality BCN/ZnO-nanorods p-n heterojunctions based on magnetron sputtered BCN films.

1.4 Organization of the thesis

The thesis is composed of seven chapters. The research subject is introduced in the present Chapter 1. Chapter 2 offers background knowledge on the development of hard protective coatings and a review of the characteristics of B-containing films. The methodologies related to the deposition and characterization techniques in this work are described in Chapter 3. The principal results with respect to the tribo-mechanical and electrical properties of the B-containing coatings are presented in the form of three peer-reviewed articles in Chapters 4, 5, and 6 in the following logical sequence of thought: First, the tribo-mechanical properties of $B_{1-x}C_x$ films are tailored by controlling the carbon content (Article 1, Chapter 4). Based on the optimized $B_{1-x}C_x$ composition, Ti is added into the $B_{1-x}C_x$ system to form Ti−B−C nanocomposite in order to enhance their tribo-mechanical properties for hard protective coating applications (Article 2,

Chapter 5). Finally, BCN films are obtained by introducing nitrogen into the $B_{1-x}C_x$ system (Article 3, Chapter 6). Their optical and electrical properties are studied with the purpose of exploring new applications of the B-containing films.

Chapter 4 (Article 1) describes the microstructure and tribo-mechanical properties of the $B_{1-x}C_x$ films deposited by magnetron sputtering. The tribo-mechanical behaviors of the $B_{1-x}C_x$ films are tailored by adjusting the carbon content, and the corresponding hardening and tribological mechanisms are discussed.

Chapter 5 (Article 2) presents the effect of adding the third element, Ti, to form Ti−B−C nanocomposite films. The mechanical properties of the Ti−B−C nanocomposites are controlled by the titanium content and the microstructural features, while their tribological properties are closely related to the surface chemical states and the mechanical properties.

Chapter 6 (Article 3) reports the optical and electrical characteristics of sputtered BCN films as well as their application in electronic devices. ZnO nanorods were grown over the BCN films to form BCN/ZnO nanorods p-n heterojunctions, the performance of which is assessed by the rectification ratio determined from the *I-V* characteristics.

Finally, Chapter 7 offers a general discussion and the main conclusions of the work accomplished throughout the thesis. Future perspectives and promising directions are proposed as well.

This thesis work gave rise to numerous publications. Specifically, Table 1.1 lists the three publications representing the heart of this thesis as well as other publications accomplished in collaboration with others. The results of this work were also presented in oral and poster forms at various international conferences and symposia as summarized in Table 1.2.

Table 1.1 Publications resulting from this Ph.D. project and collaborations

Papers in peer-reviewed journals

J. C. Qian, Z. F. Zhou, C. Yan, D. J. Li, K. Y. Li, S. Descartes, R. Chromik, W. J. Zhang, I. Bello, L. Martinu, and J. E. Klemberg-Sapieha, "Tailoring the mechanical and tribological properties of sputtered boron carbide films via the $B_{1-x}C_x$ composition", *Surface & Coatings Technology*, **267** (2015) 2 (Article 1).

J. C. Qian, Z. F. Zhou, K. Y. Li, W. J. Zhang, I. Bello, L. Martinu, and J. E. Klemberg-Sapieha, "Microstructure and tribo-mechanical properties of Ti−B−C nanocomposite films prepared by magnetron sputtering", *Surface & Coatings Technology*, **270** (2015) 290 (Article 2).

J. C. Qian, S. K. Jha, B. Wang, E. V. Jelenković, I. Bello, J.E. Klemberg-Sapieha, L. Martinu, and W.J. Zhang, "High quality boron carbon nitride/ZnO-nanorods p-n heterojunctions based on magnetron sputtered boron carbon nitride films", *Applied Physics Letters*, **105** (2014) 192104 (Article 3).

C. Yan, **J. C. Qian**, T. W. Ng, Z. F. Zhou, K. Y. Li, W. J. Zhang, I. Bello, L. Martinu, J. E. Klemberg-Sapieha, "Sputter deposition of hard quaternary Al−Mg−B−Ti nanocomposite films", *Surface & Coatings Technology*, **232** (2013) 535.

C. Yan, S. K. Jha, **J. C. Qian**, Z. F. Zhou, B. He, T. W. Ng, K. Y. Li, W. J. Zhang, I. Bello, J. E. Klemberg-Sapieha, and L. Martinu, "Electronic structure and electrical transport in ternary Al−Mg−B films prepared by magnetron sputtering", *Applied Physics Letters*, **102** (2013) 122110.

Z. H. Chen, S. Y. Yeung, H. Li, **J. C. Qian**, W. J. Zhang, Y. Y. Li, and I. Bello, "Controlled growth of $ZnO/Zn_{1-x}Pb_xSe$ core-shell nanowires and their interfacial electronic energy alignment", *Nanoscale*, **4** (2012) 3154.

S. Jha, **J. C. Qian,** O. Kutsay, J. K. Jr, C. Y. Luan, J. A. Zapien, W. J. Zhang, S. T. Lee, and I. Bello, "Violet-blue LEDs based on p-GaN/n-ZnO nanorods and their stability", *Nanotechnology*, **22** (2011) 245202.

S. Descartes, **J. C. Qian**, R. Chromik, Z. F. Zhou, K. Y. Li, and J. E. Klemberg-Sapieha, "Effect of carbon content on the tribological properties of sputtered boron carbide ($B_{1-x}C_x$) films", in preparation.

Papers in conference proceedings

J. C. Qian, Z. F. Zhou, C. Yan, D. J. Li, K. Y. Li, S. Descartes, R. Chromik, W. J. Zhang, I. Bello, L. Martinu, and J. E. Klemberg-Sapieha, "Tailoring the mechanical and tribological properties of sputtered boron carbide films via the $B_{1-x}C_x$ composition", 57th Ann. Tech. Conf. Proc., Society of Vacuum Coaters (SVC), Chicago, IL, USA, May 2014.

Table 1.2 Oral and poster presentations at conferences and symposium

Oral presentations
J. C. Qian, Z. F. Zhou, C. Yan, D. J. Li, K. Y. Li, S. Descartes, W.J. Zhang, I. Bello, L. Martinu, J.E. Klemberg-Sapieha, "Tailoring the mechanical and tribological properties of boron carbide films by adjusting the BC_x stoichiometry", ICMCTF, May 2013. San Diego, CA USA.
J. C. Qian, C. Yan, Z. F. Zhou, K. Y. Li, W. J. Zhang, I. Bello, L. Martinu, and J.E. Klemberg-Sapieha, "Mechanical and tribological properties of B-containing hard protective nanocomposite coatings deposited by magnetron sputtering", SVC Conference, May 2014. Chicago, IL USA.
Poster presentation
J.C. Qian, Z. F. Zhou, C. Yan, S. Descartes, K. Y. Li, W. J. Zhang, I. Bello, R. Chromik, L. Martinu, and J. E. Klemberg-Sapieha, "Effect of structure evolution on tribo-mechanical properties of B-containing nanocomposite deposited by magnetron sputtering for hard protective coatings", 7th Symposium on Functional Coatings and Surface Engineering (FCSE), Jun 2014. Montréal, QC Canada.

1.5 Statement of contributions

In this thesis, the main results are presented in a form of three articles that have a certain number of co-authors as dictated by the collaborative character of this thesis. Clearly, the candidate (Jincheng Qian) is the principal (first) author in all of them; her specific contributions to each of the articles are described below.

Chapter 4 (Article 1):

J. C. Qian participated in the definition of the project, experiment design, analysis of all the samples, plotting all the graphs, interpretation of results, and preparation of the manuscript. Z. F. Zhou assisted with the coating deposition. C. Yan helped in the XRD measurements (Figure 4.5). D. J. Li and S. Descartes assisted with the measurements of the tribological properties (Figure 4.3 (a)). K. Y. Li provided the magnetron sputtering deposition system. R. Chromik provided the pin-on-disk tribometer (reciprocating mode). W. J. Zhang, I. Bello, L. Martinu, and J. E. Klemberg-Sapieha supervised the project, they commented on the results interpretation and they helped to assure a good quality of English.

Chapter 5 (Article 2):

J. C. Qian participated in the definition of the project, experiment design, analysis of all the samples, plotting all the graphs, interpretation of results, and preparation of the manuscript. Z. F. Zhou assisted with the coating deposition. K. Y. Li provided the magnetron sputtering deposition system. W. J. Zhang, I. Bello, L. Martinu, and J. E. Klemberg-Sapieha supervised the project, and commented on the results interpretation and on the preparation of the article.

Chapter 6 (Article 3):

J. C. Qian participated in the definition of the project, experiment design, analysis of all the samples, plotting all the graphs, interpretation of the results, and preparation of the manuscript. S. K. Jha participated in the preparation and analysis of the p-n junction (Figure 6.4), and preparation of the manuscript. B. Wang participated in the preparation of the ZnO nanorods (Figure 6.4). E. V. Jelenković participated in the Hall measurements. I. Bello, J.E. Klemberg-Sapieha, L. Martinu, and W.J. Zhang supervised the project, and they commented on the analysis of the results and on the preparation of the article.

CHAPTER 2 LITERATURE REVIEW

This chapter reviews the background knowledge of this thesis work, based on theory and on literature reviews. The development of hard protective coatings including intrinsic and nanostructured hard coatings is introduced. The dependence of hardness upon the structure at different scales is illustrated by different coatings and coating systems, and the feasible approaches to hardness improvement are discussed. Finally, B-containing coatings are addressed with respect to their structural, tribo-mechanical, and electrical properties.

2.1 Hard protective coatings

2.1.1 Mechanical properties

The mechanical properties of a material refer to its elastic and plastic response when external forces are applied. They are generally characterized by the relationship between stress, σ, and strain, ε, as shown in Figure 2.1. The elastic response of the material is represented by the linear part of the σ-ε curve which can be described by Hooke's law, with the elastic or Young's modulus, E:

$$\sigma = E\varepsilon. \tag{2.1}$$

In this regime, the deformation of a material is reversible.

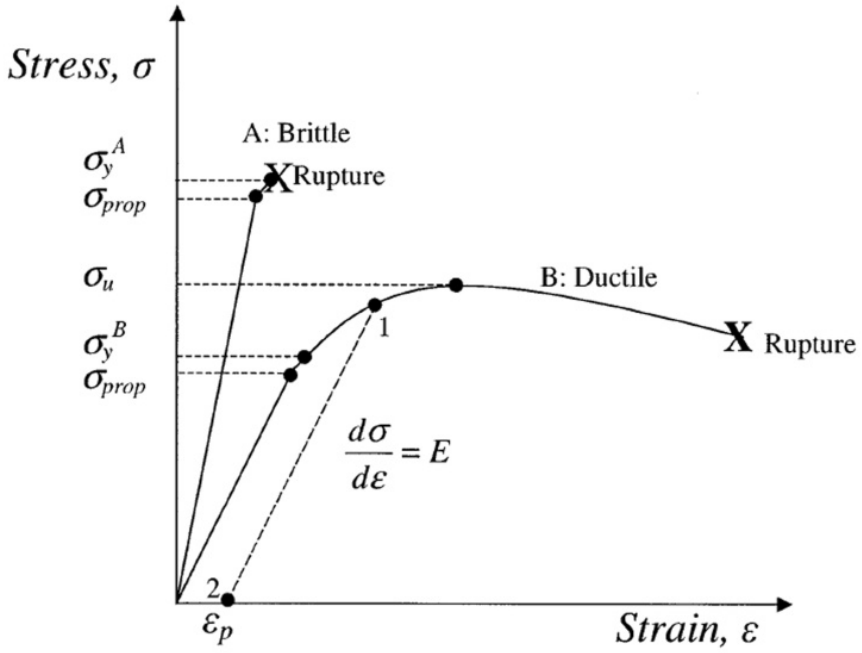

Figure 2.1 Schematic presentation of the stress-strain relation for brittle and ductile materials. Adapted from [26].

When the stress is higher than the proportionality limit, σ_{prop}, the material cannot fully recover its original shape, and Hooke's law is not applicable. Yield strength, σ_y, is defined as the stress at which plastic deformation occurs, and it represents the strength of the material. However, it is difficult to determine σ_y of a surface or a thin film in practice. Instead, hardness, H and E are measured using indentation tests, and accordingly other mechanical properties can be obtained from the H and E values. H is generally defined as the ratio of the applied load over the projected contact area, which is essentially the contact pressure as an indenter is pressed into a material surface. It represents the resistance of a solid material to both elastic and plastic deformations. The resistance of a coating to plastic deformation is proportional to H^3/E^2 since the yield pressure, P_y, in a rigid-ball contact can be determined by the equation [27, 28],

$$P_y = 0.78 r^2 \left(\frac{H^3}{E^2}\right), \tag{2.2}$$

where r is the contacting sphere radius.

Fracture toughness, K_C, is another important factor for evaluating the mechanical properties of hard materials. It indicates the resistance to crack propagation. K_C can be obtained by measuring the surface radial cracks created during indentation as described by the relation [27]:

$$K_C = \alpha_1 (\frac{H}{E})^{1/2} (\frac{P_{max}}{c_{crack}^{3/2}}) \ , \tag{2.3}$$

where P_{max} is the maximum indentation load, c_{crack} is the length of radial crack, and α_1 is an empirical constant related to the indenter geometry. Equation 2.3 indicates that every increase of the H/E ratio can improve the coating fracture toughness.

The hardness of a material is determined by its intrinsic hardness and by its microstructural characteristics [29]. Intrinsic hard materials are generally characterized by their high cohesive energy, short bond length, and a high degree of covalent bonding [30-32]. The dependence of hardness on the cohesive energy per molar volume, as illustrated in Figure 2.2, demonstrates that higher H values can be achieved with higher cohesive energy and shorter bond length. The deformation mechanisms of materials are also affected by their microstructural features, such as grain boundaries, dislocations, impurity atoms, and vacancies. In general, materials can be strengthened by increasing the defect density and reducing the grain size as a result of hindering dislocation movement. In consequence, the H values of thin films are often higher than those of corresponding bulk materials, due to the higher defect concentration and the smaller grain size in the films, particularly when they are deposited at low temperature with respect to their melting point [25, 29].

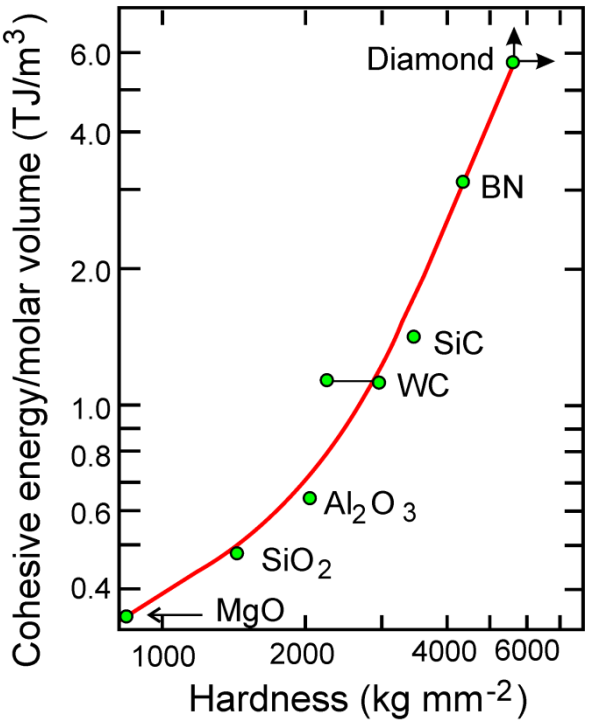

Figure 2.2 Relationship between hardness and cohesive energy per molar volume. Modified from [30].

The mechanical properties of materials are determined not only by the nature of their atomic bonds but also by their structure at different scales. Conventional metallic materials can be strengthened by plastic deformation because the growth of dislocation density during such process can increase the interaction between dislocations, and thus lead to a higher hardness [33]. Strengthening can also be achieved by increasing the grain boundary fraction, which can hinder the multiplication and movement of dislocations [25]. Therefore, hardening can be achieved by grain refinement, and such effect can be described by the Hall-Petch relationship [25],

$$\sigma_{\mathrm{y}} = \sigma_0 + k_1 \frac{1}{\sqrt{d_{\mathrm{g}}}}, \tag{2.4}$$

where σ_0 is the intrinsic yield stress, d_{g} is the grain size, and k_1 is a constant. However, this relationship is not valid when the crystallite size is lower than about 10 nm [34].

The microstructure of thin films can be controlled by the deposition conditions such as pressure, substrate temperature, and the energy of ion bombardment. The structure zone model (SZM) is used to describe the effect of deposition parameters on the thin film morphology and

microstructure. The latest SZM proposed by A. Anders [35] is illustrated in Figure 2.3. The film microstructure in three-dimensional space varies with two parameters, generalized substrate temperature, T^*, and normalized delivered energy flux, E^*. The microstructural evolution can be divided into four zones. In zone 1, the film has a high density of porous grain boundaries and defects due to the low adatom mobility and shadowing effects. In zone T, the film possesses a transition structure consisting of densely fibrous grains. Such densification is caused by the rising mobility at higher temperature and higher ion energy fluxes. In zone 2, the film exhibits a columnar structure, and the grain size increases with the temperature. In zone 3, the high energy enables bulk diffusion and recrystallization, which leads to the increase of the grain size.

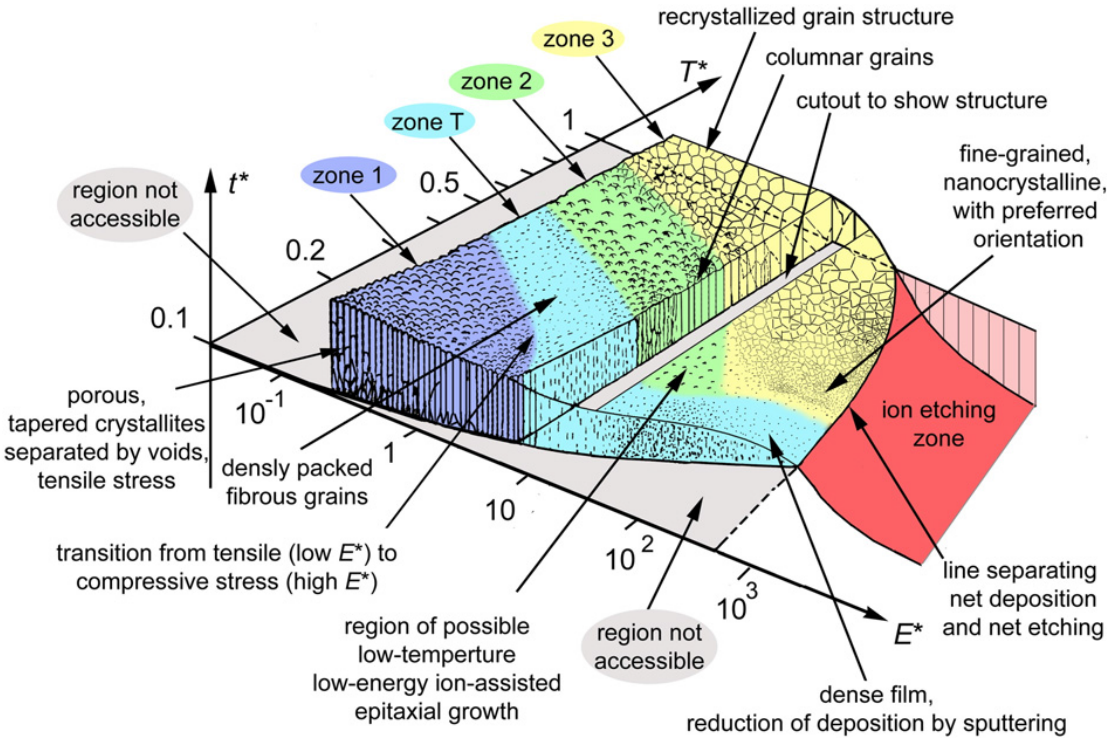

Figure 2.3 Structure zone diagram applicable to energetic deposition. Adapted from [35].

The SZM demonstrates that the film microstructure can be adjusted by the substrate temperature and ion bombardment. Hard protective coatings are usually deposited at low temperatures, which are generally less than 0.2−0.3 of the melting point, T_m, in K [36]. Therefore, ion bombardment is commonly used to modify the film microstructure during plasma-assisted growth. In general, defects created by the energetic particle bombardment can induce stress which has a close relation with the mechanical properties of the films. For magnetron sputtering

deposition, the energetic particles are commonly generated from sputtering gas and accelerated towards the growing films by a negative substrate bias [25, 37], and the intrinsic stress typically increases with the square root of the bombarding particle energy [25, 38].

According to their hardness, coatings can be divided into three groups: (i) Hard coatings with $H > 20$ GPa; (ii) Superhard coatings with $H > 40$ GPa; and (iii) Ultrahard coatings with $H > 70$ GPa [27]. The mechanical properties for the most frequently studied hard coatings are compared in Figure 2.4. Further in this chapter, these coatings are reviewed in detail with respect to their deposition process, structural characteristics, and tribo-mechanical properties.

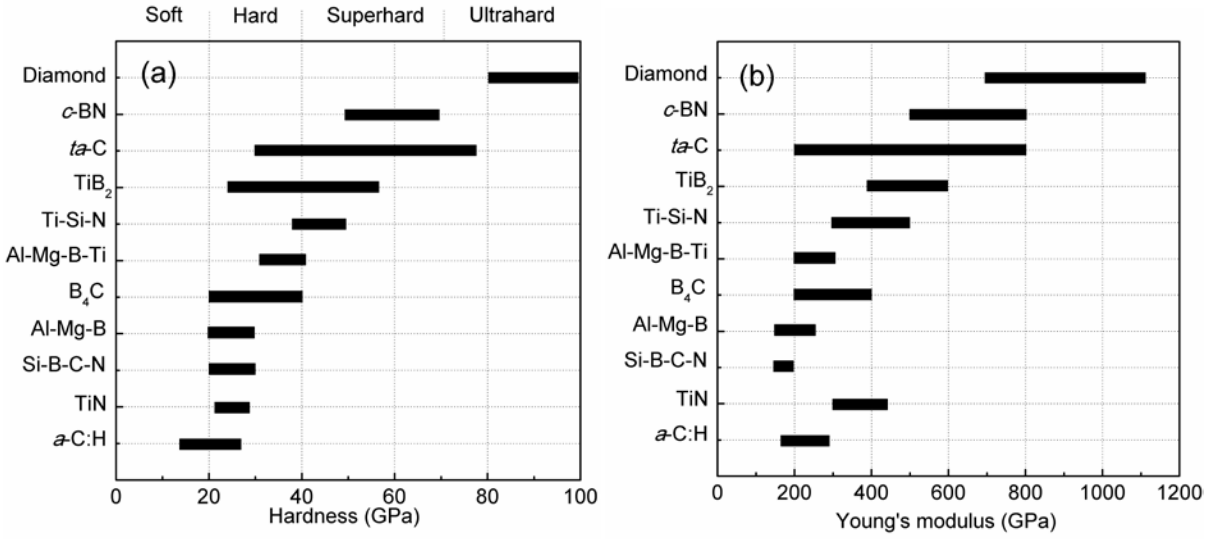

Figure 2.4 Mechanical properties for the most frequently studied hard coatings: (a) hardness, modified from [23]; (b) Young's modulus.

2.1.2 Tribology

The tribological properties, namely the friction coefficient, μ, and the wear rate, K, are also very important factors for the evaluation of the performance of hard protective coatings. Friction coefficient is defined as the ratio of the frictional force, F, over the normal applied force, P,

$$\mu = \frac{F}{P} \ . \tag{2.5}$$

The wear rate is described as the volume loss, V_{loss}, divided by P and the sliding distance, s,

$$K = \frac{V_{loss}}{P \times s}. \tag{2.6}$$

The tribological process involving two contacting surfaces in relative motion is very complex because both physical and chemical changes take place and lead to different friction-, wear-, and deformation mechanisms at different scales. Therefore, it is necessary to analyze the tribological changes including the mechanical changes on both macro- and micro- scales as well, the chemical effects, and the material transfer at the interfaces as illustrated in Figure 2.5 [39].

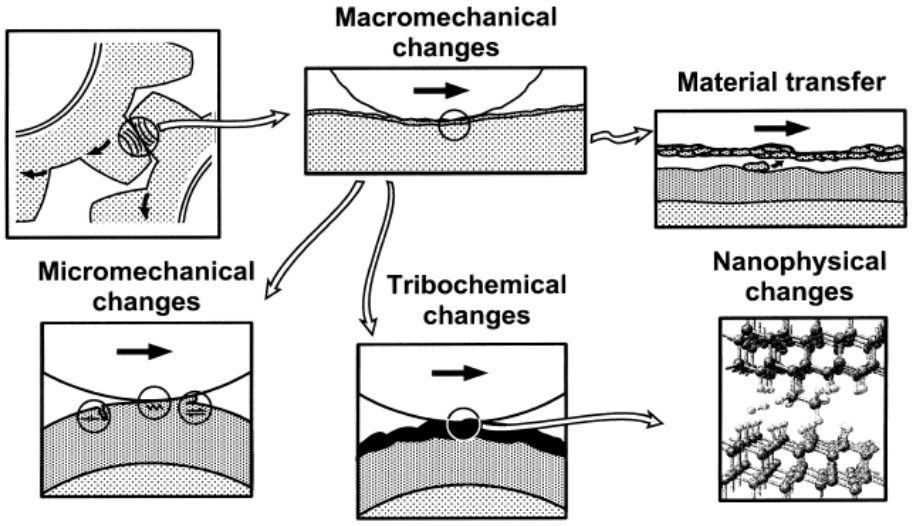

Figure 2.5 Different tribological changes that can affect the tribological contact mechanisms. Adapted from [39].

The macromechanical mechanisms relate the tribological properties to the σ-ε distribution in the contact area, the elastic-plastic deformations, and the formation of wear particles (debris, tribofilms) and its dynamics. Four main parameters are used to analyze the tribological contact behavior [39]: (i) the coating-to-substrate hardness relationship; (ii) the film thickness; (iii) the surface roughness; and (iv) the debris in the contact. When a hard spherical surface slides on a coating, twelve typical contact conditions featured by specific tribological contact mechanisms with respect to the above four parameters have to be taken into account as schematically shown in Figure 2.6.

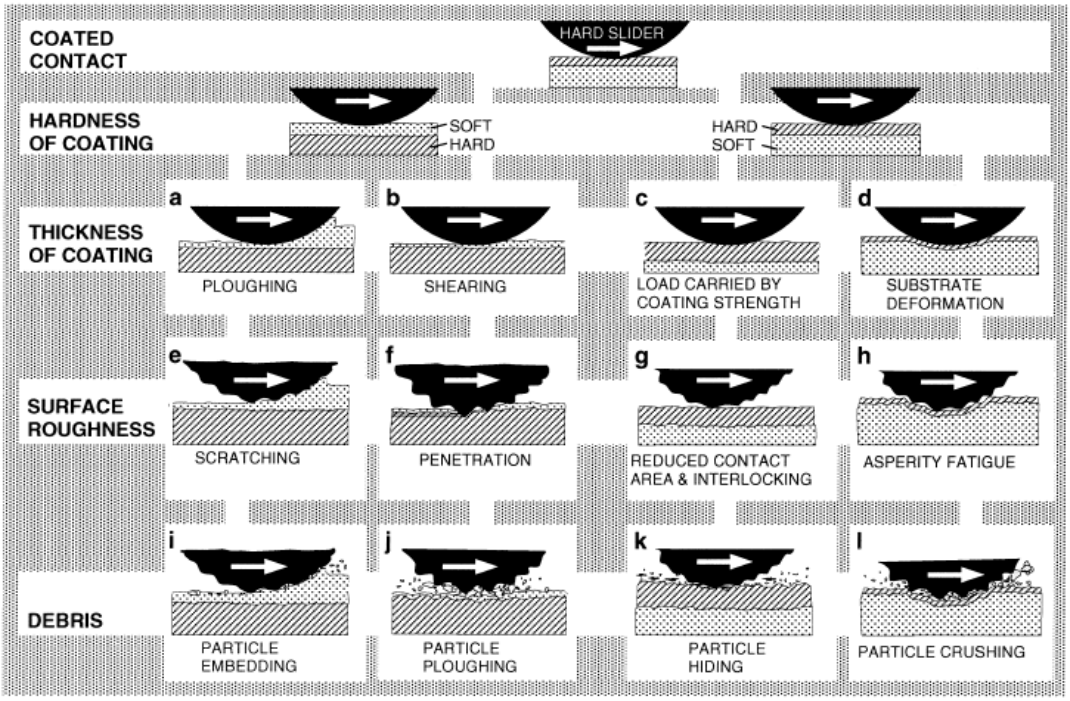

Figure 2.6 Macromechanical contact conditions for different mechanisms which influence friction when a hard spherical slider moves on a coated flat surface. Adapted from [39].

In the present work, we focus on the contact conditions of hard coatings on softer substrates. The hard coatings can decrease friction and wear by preventing ploughing, and the residual compressive stresses often existing in the coatings. Increase of the substrate hardness can reduce the friction and wear as the load support is improved, and thus deflections and ploughing are inhibited. Thick hard coatings can also increase load carrying capacity of soft substrates. Rough surfaces may reduce the real contact area, although the asperities may participate in abrasive or fatigue wear. Particles or debris are commonly formed during the tribological process. Their effect on friction and wear depends upon the particle size, the coating thickness, the surface roughness, and the hardness relationship of the particle, coating, and substrate. Under certain circumstance, tribo-chemical effects have also to be taken into account. The friction for the most frequently studied hard coatings corresponding to Figure 2.4 are shown in Figure 2.7.

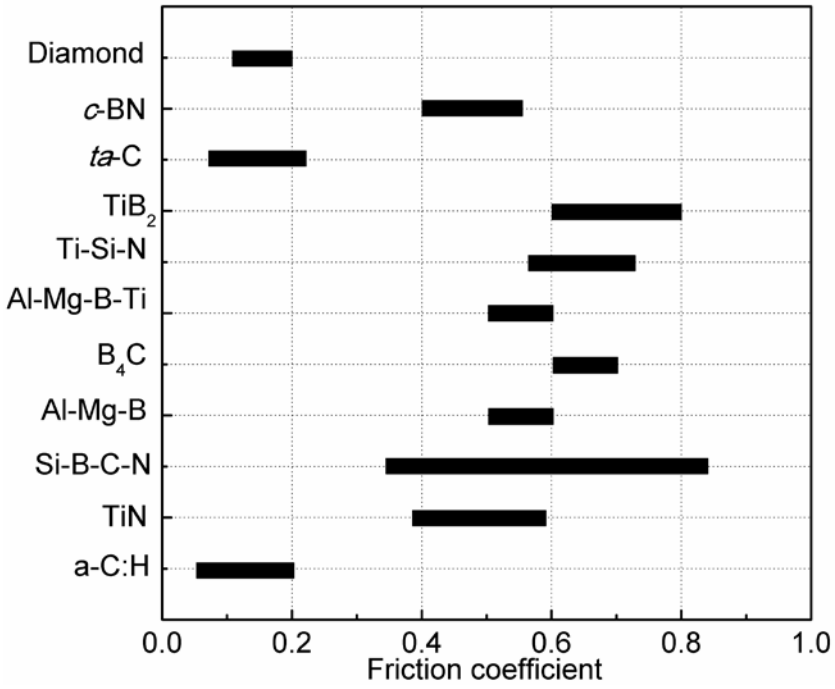

Figure 2.7 Friction coefficient for the most frequently studied hard coatings.

2.1.3 Diamond and *c*-BN films

Diamond and *c*-BN with very similar structure are described as ultrahard materials. Their attractive mechanical, thermal, optical, and electronic properties make them suitable for numerous applications including hard protective coatings.

- **Diamond films**

Diamond is well known as the hardest naturally occurring material as shown in Figure 2.2. It is made up of carbon atoms with a variation of the face-centered cubic crystal structure called a diamond lattice. The fourfold covalent bonds with small size of atoms are strong and short, which leads to the highest atomic density (1.17×10^{17} cm^{-3}) and extremely high *H* values, ranging from about 80 to 100 GPa [40]. The tribological properties of diamond are also very attractive as indicated by their low friction coefficient in humid air or dry nitrogen and high wear resistance due to its high hardness and elasticity [41]. However, the applications of diamond such as cutting tools are limited by its high deposition temperature and the high solubility of carbon in iron and in many other metals.

In the 1950s, diamond was first synthesized by high pressure and high temperature (HPHT) methods, which simulate the conditions for natural diamond growth [42, 43]. The development of CVD techniques made it feasible to deposit diamond films in nanocrystalline and polycrystalline forms on substrates which can endure CVD environment and temperature [44-46]. The typical deposition temperature of diamond films is in the range of 1000 to 1400 K [47]. Generally, pretreatments, such as polishing the substrate surfaces with diamond powder and bias enhanced nucleation with a carbon source, are used to increase the nucleation density [41].

- ***c*-BN films**

Single crystal *c*-BN with an *H* value of ~75 GPa is synthetic, and is the second known hardest material [48]. *c*-BN exhibits a structure similar to that of diamond, and its atomic density is smaller by only 4.3% than that of diamond. Consequently, the high atomic density and strong chemical bonds lead to the superhard feature of *c*-BN. In addition, the thermal stability and chemical inertness of *c*-BN even surpass that of diamond. For example, *c*-BN is chemically inert against molten ferrous materials [49] and very stable to oxidation at high temperature [50]. Nevertheless, *c*-BN coatings have not been used in practice so far, mainly due to the poor adhesion induced by the high compressive stress in the coatings.

The severe conditions of the HPHT methods and the size limitation of the *c*-BN grains promote the synthesis of *c*-BN thin films by ion-assisted PVD or CVD techniques [46, 51-53]. The *H* values of *c*-BN thin films are typically in the range of 50–70 GPa. As in the bias enhanced nucleation for diamond film deposition, ion bombardment with an energy ranging from 50 to 1000 eV is essential for the nucleation and growth of *c*-BN films. However, a high compressive stress of 5−20 GPa is inevitably induced. In consequence, delamination of *c*-BN films usually takes place when the film thickness is greater than 200 nm due to the high internal stress. Considerable effort has been devoted to overcoming the thickness limitation, including reduction of the ion energy [54, 55], increase of the substrate temperature [54, 56], post-deposition treatment [57], a two-step process with reduced bias [54], and utilization of buffer or gradient layers [48, 52, 58]. Using one or a combination of these methods, thicknesses of ~2 μm can be achieved for *c*-BN films on certain substrates such as silicon and tungsten carbide [59].

2.1.4 DLC and CN_x films

- **DLC films**

DLC is a metastable form of amorphous carbon, which contains a significant fraction of sp^3 type carbon bonds. It exhibits the high hardness, low friction coefficient, low wear rate, and chemical inertness. DLC films can be classified into two major groups, namely hydrogenated and hydrogen-free DLC films. Generally, the hydrogenated DLC (*a*-C:H) films are characterized by a hydrogen content in the range of 10−50 at.% [7, 60-63] and an sp^3 bond fraction smaller than 50%; hydrogen-free tetragonal carbon (*ta*-C) films are characterized by a small amount of hydrogen and a high sp^3 bond fraction of more than 85% [63]. The structure and properties of DLC films are determined by the hydrogen concentration and the sp^3/sp^2 ratio of the carbon bonds [64]. A simulated atomic structure of a typical *a*-C:H film is shown in Figure 2.8. It can be described as a network of carbon atoms bonded in sp^2 and sp^3 hybridization, with some bonds terminated by hydrogen [65, 66].

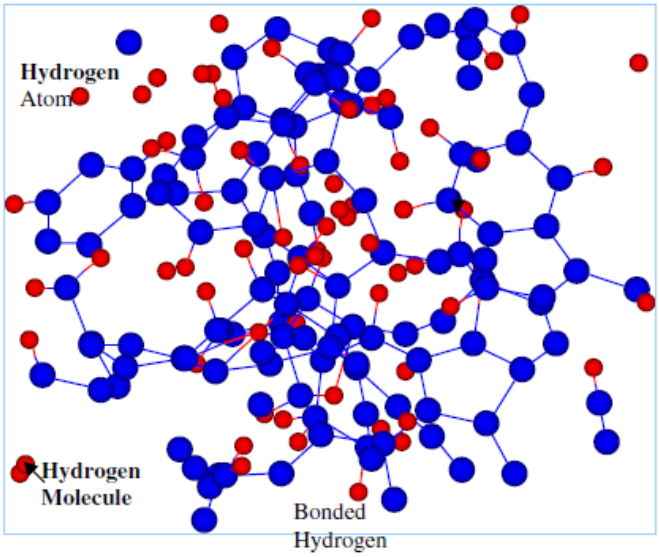

Figure 2.8 A simulated atomic structure of a typical *a*-C:H film. Adapted from [66].

The mechanical properties of DLC films are directly related to the fraction of sp^3 bonds. Specifically, the hardness and the internal stress increase with higher sp^3/sp^2 ratio [67, 68]. Typical *H* values for DLC films are between 10 and 30 GPa [63, 69], and the internal stress varies in the range of 0.5−7 GPa [63]. N, Si, O, or metals [70] may be incorporated in the DLC

films to reduce the stress, although this is usually associated with a decrease of hardness [71]. The *H* values of *ta*-C can be increased to 80 GPa, but the stress is increased as well to a high value of 13 GPa [72]. Therefore, the film thickness is limited to 1 μm due to such high internal stress. Stress reduction for *ta*-C films can be achieved by doping with metals or by multilayered structure.

DLC films present very interesting tribological properties. The reported friction coefficient varies from 0.001 to 0.7 greatly depending upon the film composition, the deposition technique, and the testing environment [64, 73, 74]. The wear rate of DLC films with high hardness can be as low as 10^{-11} mm^3/Nm [75], whereas films with low hardness can be scratched easily. The great disparity in their tribological properties can be attributed both to intrinsic and to extrinsic factors. Intrinsically, the sp^2/sp^3 ratio, the hydrogen content, and the incorporation of other elements can greatly affect the tribological behavior of DLC films. Extrinsically, the tribological performance is also influenced by the roughness of the film surfaces, the tribotest conditions, and the chemical environment, such as humidity and atmosphere. For instance, *a*-C:H films present super low friction coefficients (< 0.01) in vacuum or inert gases [76]. In contrast, higher friction coefficient values (~0.2) were observed in ambient air (30%−60% RH) [62]. Mechanistically, the extremely low friction is caused by the formation of a highly passive surface which does not interact chemically or physically with the counterfaces [66].

DLC films have been widely used in various industrial applications due to their impressive tribo-mechanical properties. For example, DLC films have been coated on magnetic media in hard disks to provide mechanical and corrosion protection [77, 78]. In addition to their excellent tribo-mechanical properties, the biocompatibility of DLC films allows them to be applied as protective coatings for biomedical devices and tools [17, 79]. DLC films have been applied in the automotive industry as well. DLC coatings on the surfaces of mechanical components can effectively reduce the friction forces under oil-lubricated conditions and consequently improve the fuel efficiency [80-82].

- **CN_x films**

Numerous theoretical investigations have explored novel materials with high intrinsic hardness. A hypothetical C_3N_4 phase has been predicted to be harder than diamond [83-85]. Such high hardness has never been demonstrated experimentally, since the compositional C/N ratio of

3 to 4 cannot guarantee the C_3N_4 structure [86, 87]. The *H* values of CN_x films prepared by varieties of PVD and CVD methods were reported to be in the range of 15 to 50 GPa [88-90], and the elastic recovery is up to 85% [89]. CN_x films with low N concentration exhibit very attractive tribological properties, namely low friction coefficient and high wear resistance [88, 91]. Compared to DLC films, CN_x films present comparable tribo-mechanical properties and even some superior characteristics such as the reduced stress [73, 92]. Therefore, CN_x films are very promising for appicatoin as the protective coatings on hard disks [19, 93].

A number of ternary and quaternary hard coatings such as Si−C−N and Si−B−C−N films have been developed based on the studies on CN_x. For example, Si−C−N films deposited by plasma enhanced chemical vapor deposition (PECVD) present a high *H* value of 33 GPa, a high elastic recovery of 85%, and a low compressive stress of 1.1 GPa [11]. In addition, their optical properties can be adjusted through the control of the film composition. The refractive index and the extinction coefficient (at 550 nm) can be varied from 1.85 to 2.10 and from 1.0×10^{-4} to 4.5×10^{-2}, respectively. Quaternary Si−B−C−N coatings attracted considerable attention, due to their high thermal stability. The *H* and elastic recovery of Si−B−C−N films deposited by reactive magnetron sputtering are 31 GPa and 81%, respectively, and no degradation was observed after annealing in helium up to 1300 ºC [94]. In addition, no mass loss is detectable after annealing in air at temperatures up to 1300 ºC. This indicates their high oxidation resistance.

2.1.5 Transition-metal nitride and carbide films

The chemical bonds of transition-metal (TM) nitrides and carbides are a mixture of covalent, metallic and ionic components [95], and are well known for their high hardness, high melting point, and chemical inertness. TM nitrides and carbides are interstitial compounds. That is the small nitrogen and carbon atoms are embedded in the gaps of the metallic lattice. Such a structure is not closely packed, since the metallic unit cells are expanded by the interstitials [96]; therefore their *H* values are lower than that of diamond and *c*-BN. The interstitial compounds can be formed with different stoichiometries, such as M_4X, M_2X, MX, and MX_2, where M represents the metal elements, and X represents the C or N interstitials. In general, the TM nitrides and carbides, such as TiN, CrN, and TiC [96] here used for hard coatings are MX type with a face centered cubic B1 NaCl structure. We consider titanium nitride films, a typical representative with respect to mechanical properties and the corresponding hardening mechanisms.

Titanium nitride (TiN_x) exhibits a NaCl structure with a wide compositional range ($0.6 < x < 1.2$), and its *H* value is in the range of 20−22 GPa. TiN_x films have been extensively used for hard protective coatings due to their attractive tribo-mechanical properties. They are also applied as decorative coatings owing to their golden color. In addition, they can function as a diffusion barrier for Al, Cu, or Ag interconnects in microelectronics, and serve as biocompatible wear-resistant coatings for biological devices and implants [97]. However, the oxidation resistance of TiN_x is limited at temperature higher than 500 ºC. This restricts its application in the machining industry. Adding other metallic elements, such as Al, to form a single phase (Ti, Al)N solid solution was proposed to enhance the oxidation resistance since Al can form a stable compact oxide of Al_2O_3 on the surface at high temperature and protect the underlying (Ti, Al)N coatings from oxidation [98].

The strengthening mechanism of hard protective coatings can be illustrated by the influence of the microstructural evolution on the mechanical properties of TiN and CrN films as shown in Figure 2.9 [99, 100]. Figure 2.9 (a) presents the linear relationship between the residual compressive stress and the *H* value of the TiN and CrN films deposited by magnetron sputtering. Such a dependence can be explained by the dislocation mechanism, that is the defects acting as barriers for dislocation movements can improve the hardness. Therefore, TiN and CrN films with higher defect density as reflected by a higher residual stress present higher *H* values. The strengthening effect of TiN and CrN films can also be demonstrated by their hardness variation with grain size as shown in Figure 2.9 (b). The hardness of TiN films increases with smaller grain size, which follows the Hall-Petch relationship. On the contrary, the hardness variation of CrN films exhibits an inverse Hall-Petch relationship when the grain size is lower than a critical value, since the hardening mechanism based on dislocations is invalid at such small grain size.

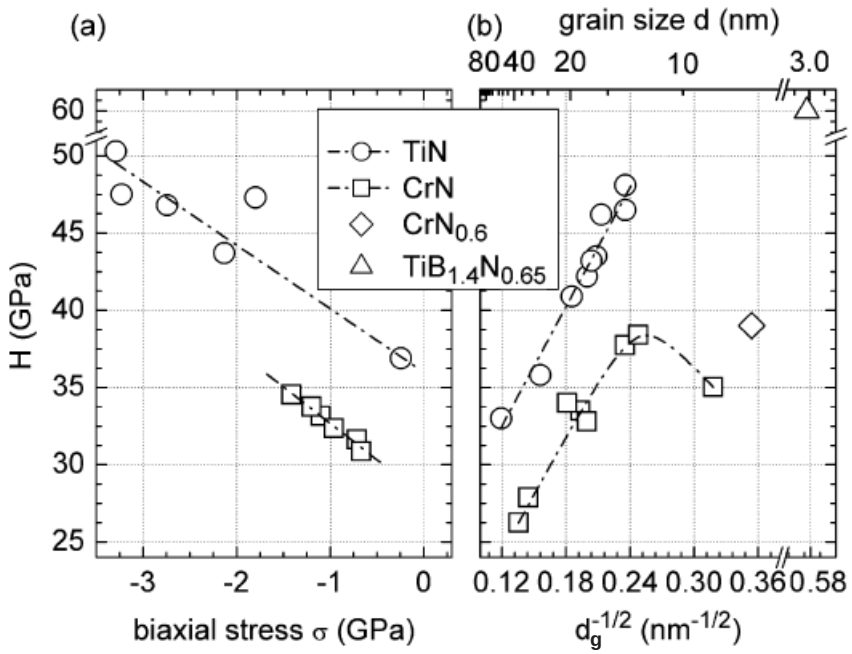

Figure 2.9 Interrelationship between (a) hardness, H, and biaxial coating stress, σ, and (b) H and grain size, d_g, for sputtered TiN, CrN, $CrN_{0.6}$, and $TiB_{1.4}N_{0.65}$ films [99, 101]. Adapted from [25].

Hardness enhanced by ion bombardment is only valid at a relatively low deposition temperature of about ≤ 300 °C. The strengthening effect reduces at higher temperature and vanishes above 600−700 ºC [102]. The H values can be reduced to that of the ordinary bulk materials after post annealing due to the relaxation of the ion-induced stress at high temperature. The dependence of hardness and defect density on the annealing temperature for TiN films deposited at 300 °C is presented in Figure 2.10. As the annealing temperature increases, the compressive stress is relaxed, as indicated by the reduction of lattice parameter and the growth of grain size. Thus, the hardness reduction after post annealing is caused by defect annihilation and stress reduction, induced by the higher diffusivities at higher temperature.

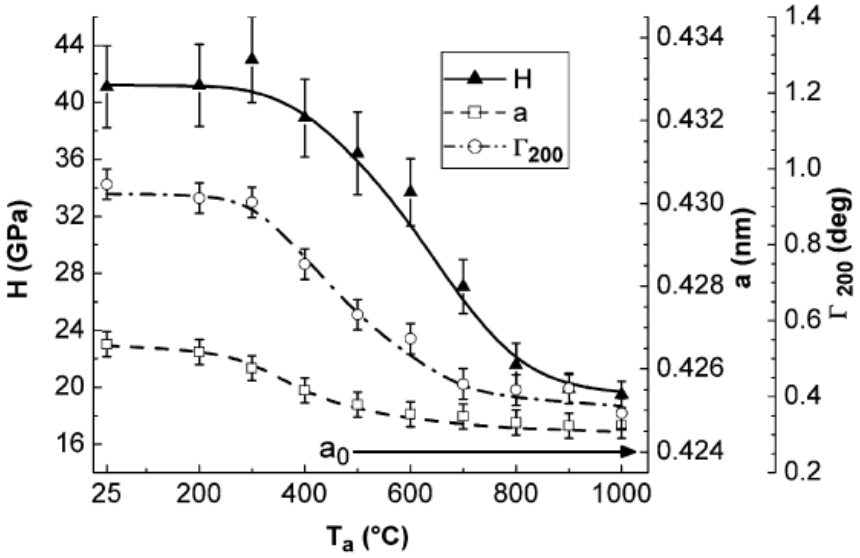

Figure 2.10 *H*, lattice parameter, *a*, and full width at half maximum (FWHM) intensity, *Γ*, of the (200) XRD peak of TiN films reactively grown at 300 ºC as a function of annealing temperature, T_a. Adapted from [25, 103]

2.1.6 Nanostructured hard coatings

Nanostructured materials, featured by their structural elements such as clusters or crystallites being at least one dimension less than 100 nm [104], represent a new generation of materials. Nanostructured coatings with proper microstructural design show superior tribo-mechanical properties compared to traditional materials. Therefore, considerable effort has been devoted to developing nanostructured coatings with structures which improve their performance and functionality. Two typical coating nanostructures used for hardness enhancement are superlattice and nanocomposite, as shown in Figure 1.1 (iv) and (v), respectively. Superlattice coatings are nanometer-scale multilayers made up by two different alternating layers. The superlattice period, λ_{period}, defined as the bilayer thickness of two materials is typically in the range of 5 to 10 nm. Nanocomposite coatings are characterized by a heterogeneous structure composed of nanocrystallites in an amorphous or nanocrystalline matrix.

Superlattice coatings can be classified into five types, according to the composition of the bilayer: (a) metal superlattice, (b) nitride superlattice, (c) carbide superlattice, (d) oxide superlattice, (e) nitride, carbide, or oxide/metal superlattice. The superlattice coatings composed of nitrides or carbides usually present a relatively high hardness. For example, nitride superlattice

coatings, such as TiN/VN [105] and TiN/NbN [106], exhibit *H* values in the range of 45−55 GPa, which are greater than those of the individual layers. The corresponding hardening effect is explained by hindrance of dislocation movements by the sharp interfaces between layers with different *E*. Nitride/metal superlattice coatings, such as TiN/Ti and WN/W [107], have been developed. The ductility of the metal can enhance the coating toughness, while the nitride layers can retain *H* values higher than 30 GPa.

The study of superlattice coatings is significant for the development of hard coatings and the understanding of hardening mechanisms. However, the hardness of superlattice coatings is strongly affected by λ_{period}, and it is very difficult to maintain the same thickness of each layer during the deposition in industrial machines, particularly on substrates with complex geometries. In addition, the interdiffusion of elements between layers at high substrate temperature will degrade mechanical performance. Such problems impede the applications of superlattice coatings in practice. However, these disadvantages can be avoided when the superlattice coatings are replaced by nanocomposite coatings.

The hardness of nanocomposite coatings with proper microstructural design can reach hard, superhard, or even ultra-hard level, significantly exceeding that given by the law of mixture. In addition to the high hardness, it is also possible to adjust other properties due to the characteristics of the multi-phase. Therefore, they are excellent candidates for hard protective coatings [108]. For conventional materials with the number of atoms in the grains much greater than that in grain boundary regions, the hardening mechanism is described by the Hall-Petch relationship as discussed in Section 2.1.3, but it is invalid for nanocrystalline materials with grain size smaller than 10 nm. As the grain size is reduced below 10 nm, the number of atoms in the grains is comparable to that in boundary regions, thus the mechanical properties are determined by grain boundary sliding rather than dislocation movement. In consequence, the hardness decreases with decreasing grain size, due to the fast diffusion of atoms and vacancies under stress induced by the large quantity of defects in the grain boundaries [109]. Nanocomposite coatings comprising different crystalline phases with strong interfaces can hinder grain boundary sliding and consequently enhance the mechanical properties.

Successful examples of superhard nanocomposite coatings, such as the Ti−Si−N and Ti−B−N systems, have been demonstrated in previous studies. Ti−Si−N coatings deposited by

CVD present *H* values of 60−70 GPa, as first reported by S. Li [110]. The Ti−Si−N system was further developed by S. Veprek with the idea of forming nanocrystalline-TiN (*nc*-TiN) imbedded in an amorphous-Si_3N_4 (*a*-Si_3N_4) matrix [111]. The *nc*-TiN/*a*-Si_3N_4 films with crystallite size as small as 3 nm exhibit the highest *H* value of 50 GPa [112] as well as a high thermal stability [113]. Figure 2.11 shows the hardness of *nc*-TiN/*a*-Si_3N_4 coatings deposited by PECVD as a function of the silicon nitride fraction [23, 114]. Silicon-free TiN films exhibits a nanocolumnar structure and an *H* value of ~25 GPa as shown in inset A. As the Si_3N_4 content is increased to 7–10 at.%, a nanocomposite is formed with a structure of TiN nanocrystallites (~8 nm) separated by a few monolayers of silicon nitride, as shown in the inset B in Figure 2.11. The corresponding hardness is significantly improved to superhard level. Further increase of the silicon nitride fraction leads to ordinary crack propagation in the Si_3N_4 phase and the reduction of *H* values to that of single-phase Si_3N_4 [115].

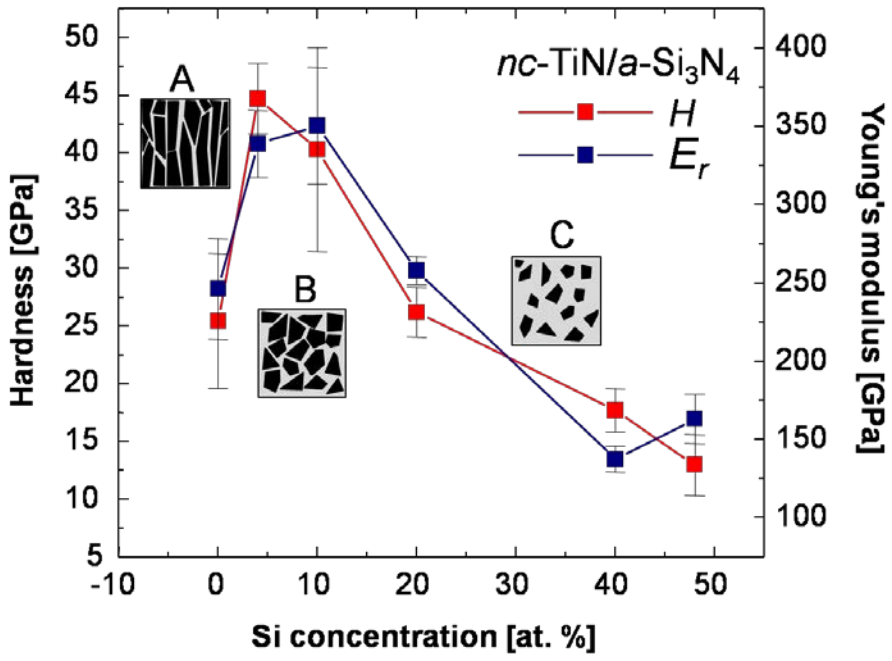

Figure 2.11 Hardness of *nc*-TiN/*a*-Si_3N_4 films as a function of Si concentration. Schematic structures of the films with different silicon concentrations are illustrated in the insets. Modified from [23, 114].

2.2 B-containing films

Boron is the only non-metal in Group 13 of the periodic Table. B-containing materials have attracted a lot of attention due to their unique structural, mechanical, and electronic properties. It exhibits many similarities to its neighbor, carbon, and its diagonal relative, silicon, such as the marked propensity to form covalent bonds [116]. B-containing materials, such B_4C, TiB_2, and aluminum magnesium boron ($AlMgB_{14}$), exhibit very high hardness. Moreover, their electronic characteristics are also very interesting. For instance, BCN is well-known for its semiconducting characteristics with a controllable band gap [117]. In this section, the tribo-mechanical, optical, and electrical properties of B-containing materials will be reviewed in detail.

2.2.1 Boron carbide films

Crystalline boron carbide ($B_{1-x}C_x$, usually denoted as B_4C) is a covalent compound well known for its excellent mechanical properties. With a *H* value of ~40 GPa, it is the third hardest material after diamond and *c*-BN at room temperature [118]. Moreover, it also presents a low density of 2.52 g/cm^3, a low thermal expansion coefficient of 4.3×10^{-6} K^{-1}, a very high thermal stability (no phase segregation up to 1400 ºC) [119], and very high chemical inertness, which make it suitable for many industrial applications such as grinding, cutting tools, ceramic bearing, wire drawing, etc [120-122].

The lattice structure of $B_{1-x}C_x$ (see Figure 2.12) is known as a rhombohedral unit cell (space group *R-3m*) consisting of 12-atom icosahedral units at the vertices and a 3-atom chain connecting the nodes along the (111) axis. Boron carbide is usually described as "stoichiometric formula" B_4C, but it can maintain its single phase rhombohedral structure with the carbon concentration varying from 8.8 to 20 at.%. When the carbon content is higher than 20 at.%, a segregated carbon phase is detected [113, 123, 124]. However, the detailed arrangement of boron and carbon is still ambiguous [125, 126] since ^{11}B and ^{12}C cannot be well distinguished by X-ray and neutron diffraction due to their similarity in electron density and nuclear cross-section [125-129].

B_4C was described earlier as B_{12} icosahedra at each corner and C−C−C chains along the diagonals [130]. However, it is now well accepted that the lattice structure is $B_{11}C$ icosahedron located at each node, and one linear C−B−C chain connects the nodes along the (111) axis [131-

133]. As the carbon concentration gradually decreases from 20 to 8.8 at.%, the C−B−C chains are firstly replaced by C−B−B chains, and the $B_{12}C$ icosahedra will further be replaced by B_{12} icosahedra as the C−B−C chains are nearly depleted [131-133].

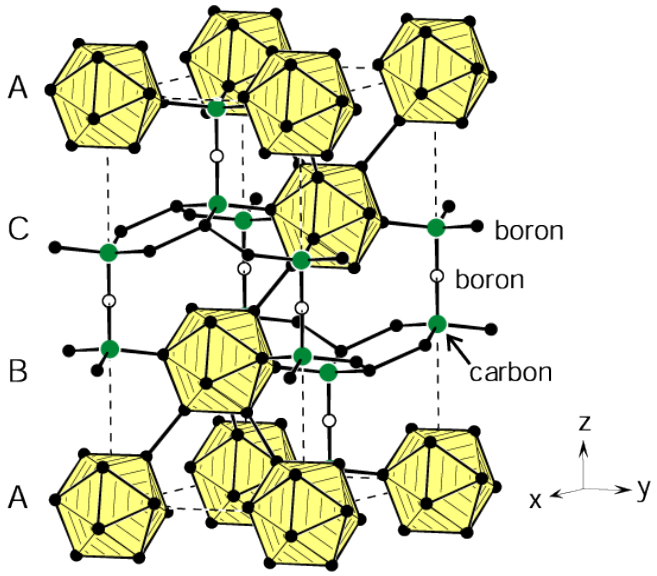

Figure 2.12 Crystal structure of B_4C in hexagonal setting consisting of icosahedra formed by boron atoms (solid circles) and linear C−B−C units. The ABC stackings of the rhombohedral structure are indicated at the left-hand side. Adapted from [134].

In addition to its attractive mechanical properties, B_4C also presents very interesting tribological properties. The friction coefficient of B_4C can vary in a large range depending on the relative humidity of the surrounding air [135, 136]. B_4C presents a high friction coefficient of 0.7 in dry air, but a low friction coefficient of 0.2 in humid atmosphere due to the formation of boron acid (H_3BO_3) with layered crystal structure and an ultra low friction [137]. The friction coefficient can be reduced to 0.03−0.05 after flash annealing at 600−800 ºC in air. A very thin layer of boron oxide (B_2O_3) is formed in the upper surface during annealing, as a result of oxidation of B_4C. During cooling in air, the surface B_2O_3 reacts with moisture to form H_3BO_3.

Numerous studies have focused on the development of $B_{1-x}C_x$ films due to the attractive tribo-mechanical properties of bulk $B_{1-x}C_x$. A variety of deposition techniques, such as CVD [138-140], magnetron sputtering [141-143], ion beam assisted deposition [144], and pulsed laser deposition [145] were used for the synthesis of $B_{1-x}C_x$ films. The effect of composition and

microstructure on their mechanical properties was investigated, aiming at applications for protective coatings [18].

Magnetron sputtering is the most widely used technique for the deposition of $B_{1-x}C_x$ films [146, 147]. The mechanical properties of amorphous and crystalline B_4C films deposited by magnetron sputtering were studied by V. Kulikovsky et al. [146]. Its hardness dependence on the substrate temperature, T_s, (see Figure 2.13 (a)) shows that the H value increases from 27 to 35 GPa as the T_s increases from room temperature (RT) to 940 ºC. The hardness is closely related to the crystallinity of the B_4C films as indicated by their Raman spectra in Figure 2.13 (b). It is found that crystalline B_4C films can be formed only at T_s higher than 900 ºC due to the very high T_m, and the films synthesized at lower temperature are amorphous or nanocrystalline [146, 147]. Therefore, a gradual improvement of the atomic structure at increasing T_s leads to the strengthening of the B_4C films.

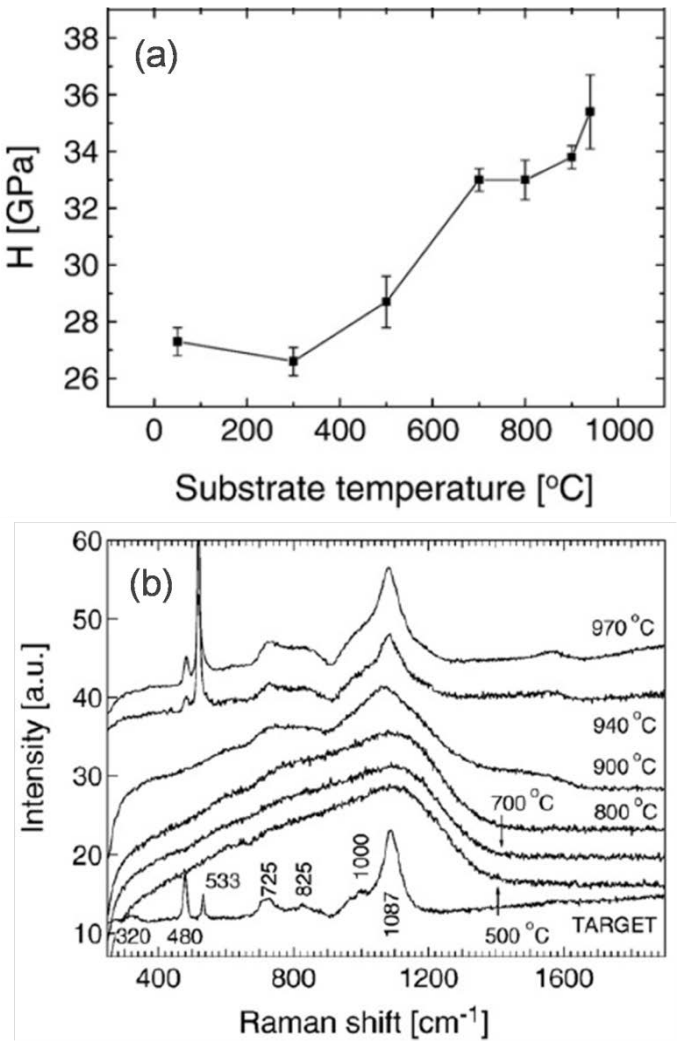

Figure 2.13 (a) H of B_4C films deposited by magnetron sputtering as a function of substrate temperature, T_s; (b) Raman spectra of B_4C films deposited at different T_s, and that of boron carbide target material is shown for comparison. Adapted from [146].

The electronic properties of $B_{1-x}C_x$ were also well studied. The band gap of single crystal $B_{1-x}C_x$, calculated in theoretical studies, is > 2.7 eV [148, 149], which is not consistent with the value (0.47 eV) determined from the experimental optical absorption spectra [150]. Such a discrepancy is attributed to the defects in real $B_{1-x}C_x$, a problem not considered in the idealized structure. These defects induce high-density gap states and give rise to a narrow band gap [151].

Based on the interesting optical and electrical properties of bulk $B_{1-x}C_x$, much effort has been devoted to the investigation at those properties. $B_{1-x}C_x$ films were reported to be p-type semiconductors, and their band gap can be tuned by adjusting the ratio of boron to carbon [152].

The band gap of $B_{1-x}C_x$ films deposited by PECVD varies from 0.8 to 1.8 eV with increasing B/C ratio as presented in Figure 2.14. Regarding the high thermal stability and the semiconductor properties, $B_{1-x}C_x$ films may be applied in electronic devices operated in a high temperature environment [122].

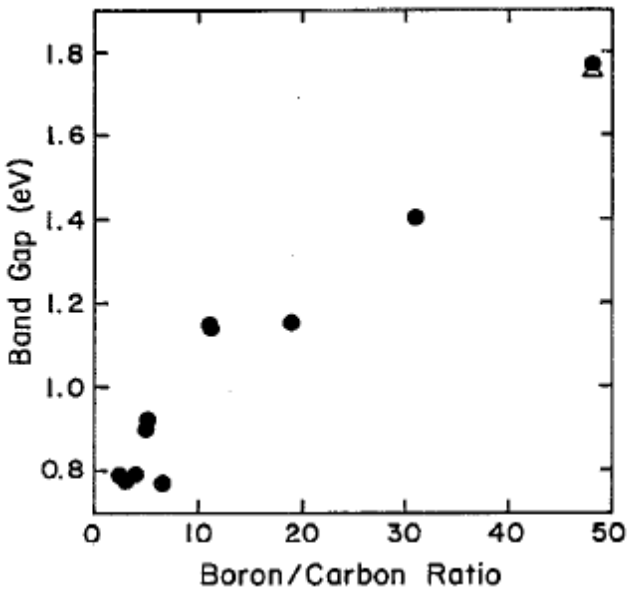

Figure 2.14 Band gap values of the $B_{1-x}C_x$ films deposited by PECVD in dependence on the B/C ratio. Adapted from [152].

Due to the high neutron absorption cross section of boron, various p-n junctions based on $B_{1-x}C_x$ have been study for potential applications in solid neutron detectors [153]. Heterojunctions were formed by p-type $B_{1-x}C_x$ films with n-type semiconductors such as n-Si and n-SiC [154, 155]. $B_{1-x}C_x$/n-SiC devices present good semiconductor diode performance from room temperature to 351 ºC indicating the possibility of operating $B_{1-x}C_x$ based devices at high temperature. An N-type Ni-B_5C film achieved by doping B_5C film with Ni was used to form a p-B_5C/n-Ni-B_5C homojunction [156] demonstrating the feasibility of constructing $B_{1-x}C_x$ homojunctions via metal doping.

2.2.2 TiB_2 films

TiB_2 is known for its high T_m of 3225 ºC and high H value of ~25 GPa [157]. It exhibits a hexagonal crystal structure (space group *P6/mmm*), in which boron atoms are in the interstices between the (0001) close-packed Ti planes [158, 159] as shown in Figure 2.15. TiB_2 has a

relatively narrow single-phase field with boron content ranging from 65.6 to 66.7 at.%, due to the strong covalent bonding in the B network [159]. The alternation of strongly bonded boron and metallic titanium planes along the *c* axis leads to the high electrical conductivity of ~10^5 S/cm, the thermal conductivity of 96 W/mK, as well as the high hardness and chemical stability [158]. Therefore, it is capable at working at high temperature for cutting tools, impact resistant armor, and wear applications [157].

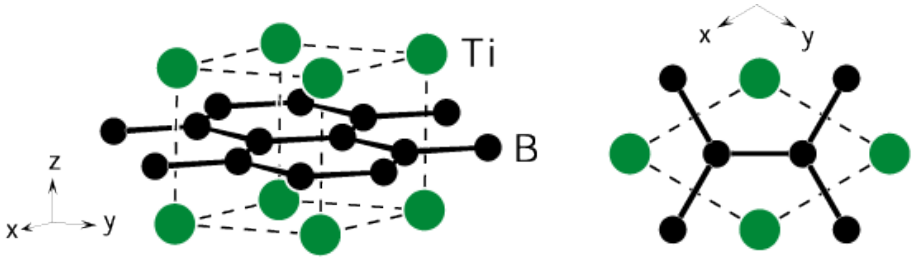

Figure 2.15 Hexagonal structure of TiB_2 with a perspective view on the left and a projection along the hexagonal axis on the right. Adapted from [134].

The development of TiB_2 films is inspired by the excellent mechanical properties and high thermochemical stability of bulk TiB_2. TiB_2 films have been synthesized by a variety of deposition techniques, such as CVD [160], pulsed laser deposition (PLD) [161], reactive sputtering [162], and magnetron sputtering [158, 159, 163]. The *H* values of TiB_2 films were reported to be in the range of 48 to 77 GPa, much higher than that of bulk TiB_2, and the corresponding mechanisms were widely studied. The effect of sputtering conditions including substrate bias and temperature on the microstructure and mechanical properties of TiB_2 films was reported by M. Mikula et al. [164]. It is found that the *H* values of the TiB_2 films varies in the range of 34−73 GPa, and highest compressive residual stress is up to around 5.4 GPa, as shown in Figure 2.16 [164]. The TiB_2 films exhibit a (001) preferred orientation which is largely dependent on the substrate bias. The compressive stress can be reduced by increasing the substrate temperature and decreasing the negative substrate bias, and consequently, the corresponding hardness decreases as well. However, the *H* values of TiB_2 films with low compressive stress can still reach superhardness level implying that the compressive stress induced by ion bombardment is not the only source of the high hardness.

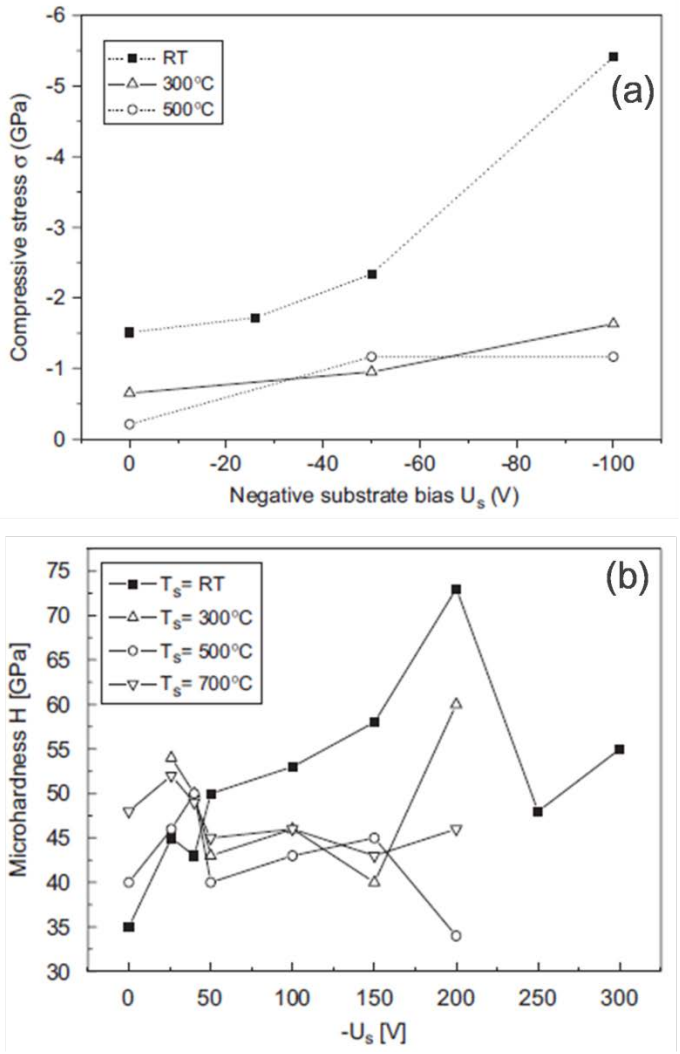

Figure 2.16 (a) Compressive stress in the TiB_2 films sputtered on Si (001) substrates as a function of substrate bias, U_s, at different T_s; (b) Microhardness of the TiB_2 films sputtered on WC substrates as a function of U_s at different T_s. Adapted from [164].

P. H. Mayrhofer et al. demonstrated that the superhardness of TiB_2 films can be obtained only with overstoichiometric TiB_2 films exhibiting a columnar structure and (001) preferred orientation. The superhardness is correlated with the formation of nanocolumnar structure [159]. In their work, TiB_x films were deposited by magnetron sputtering from a stoichiometric TiB_2 target. The film composition strongly depends upon the ratio of incident ion to metal flux (J_{Ar+}/J_{Ti}). Overstoichiometric $TiB_{2.4}$ film presents a microhardness of 60 GPa. The XRD patterns, the lattice constants c, and the full width at half maximum (FWHM) intensity values Γ_{0001} of the $TiB_{2.4}$ film before and after annealing at different temperatures, T_a, are presented in Figure 2.17 (a)

and (b). It is found that the compressive stress is relaxed by annealing as indicated by the lattice constant *c* decreasing to that of bulk TiB_2, and the (0001) diffraction peak shifting to higher angles. However, the *H* value of the $TiB_{2.4}$ film remains constant after annealing at $T_a \leq 700$ ºC, which excludes the compressive stress as the origin of the superhardness. TEM investigations reveal that the $TiB_{2.4}$ film exhibits a complex self-organized nanocolumnar structure which is thermally stable to $T_a \leq 700$ °C. The columns with diameters of ~20 nm and (0001) preferred orientation are encapsulated in an excess of boron, and consist of a bundle of ~5 nm diameter stoichiometric TiB_2 subcolumns separated by a thin 1−2 monolayer B-rich tissue phase. Therefore, the superhardness of $TiB_{2.4}$ film can be attributed to the nanocolumnar structure inhibiting nucleation and glide of dislocations during the plastic deformation, as well as the high cohesive strength of the thin B-rich tissue phase preventing grain boundary sliding as well [159].

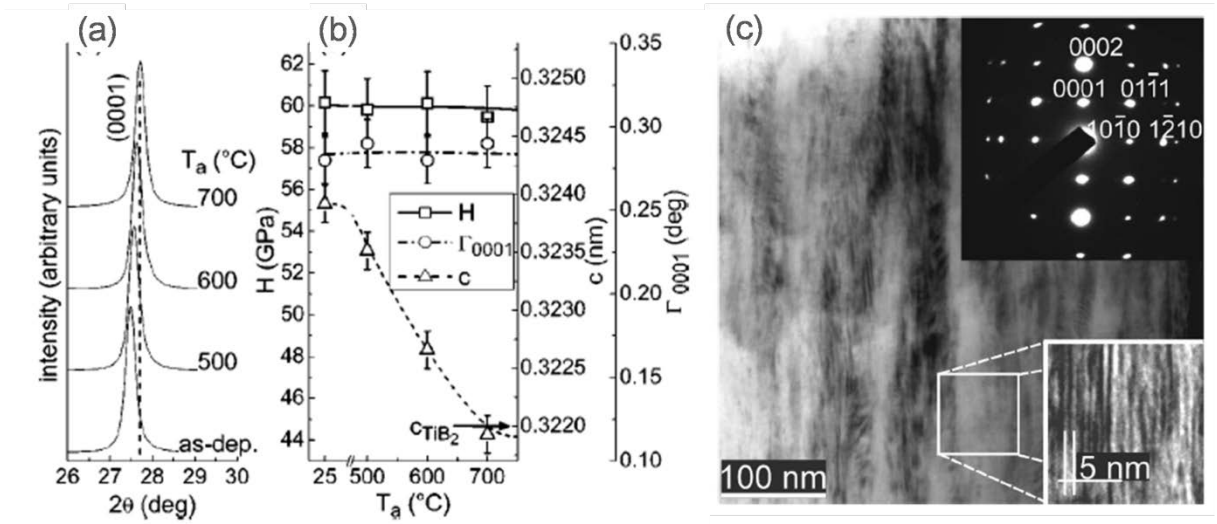

Figure 2.17 (a) XRD patterns from $TiB_{2.4}$ film before and after annealing at different temperatures, T_a; (b) *H*, lattice constant, *c*, and Γ_{0001} of the (0001) XRD reflection as a function of T_a, and *c* of bulk TiB_2 is indicated by an arrow for comparison; (c) Bright-field XTEM image of $TiB_{2.4}$ film after annealing at 700 °C. The corresponding SAED pattern obtained near the upper portion is shown at the top right, and a higher-resolution image of the 0001-oriented ~5 nm wide subcolumnar nanostructure is shown at the lower right. Adapted from [159].

2.2.3 B-containing nanocomposite films

B-containing nanocomposite hard coatings are of great interest due to the possibility of forming hard B-containing phases. For example, superhardness was achieved by Ti−B−N nanocomposite films deposited by PECVD and magnetron sputtering [165]. The Ti−B−N films deposited by PECVD have a *nc*-TiN/*a*-BN structure and *H* values of 40–50 GPa [166]. The highest *H* value is achieved with the structure of TiN nanocrystals covered by about one monolayer of *a*-BN. The structural and mechanical properties of the magnetron sputtered Ti−B−N films were studied by P. H. Mayrhofer et al. [165]. Nanocrystalline $TiB_{0.80}N_{0.83}$ films consist of ~50 at.% of a fully disordered phase encapsulating TiN and TiB_2 grains with sizes of 2−3 nm, and exhibits a *H* value of ~37 GPa. After annealing at 800 ºC, the *H* value is increased to 43 GPa since the density of the disordered boundary regions increases, while the B/Ti ratio and the mean crystallite remain constant at 0.8 and 2−3 nm, respectively. However, the hardness drops off when the annealing temperature increased to higher than 900 ºC. This is a result of composition changes caused by B loss [165].

$AlMgB_{14}$ is another interesting B-containing compound containing B_{12} icosahedra [167]. The *H* value of $AlMgB_{14}$ composites is ~35 GPa, and it can be further improved by introducing other elements or phases, such as Si or TiB_2. C. Yan et al. described the Al−Mg−B based nanocomposite hard coatings synthesized by magnetron sputtering. Such ternary composite films prepared by sputter deposition present *H* values of ~30 GPa [168], while the *H* values of quaternary Al−Mg−B−Ti nanocomposite films can be enhanced to higher than 40 GPa, due to the formation of $AlMgB_{14}$ and TiB_2 nanocrystallites imbedded in an amorphous Al−Mg−B matrix [169].

2.2.4 Boron carbon nitride films

BCN films have attracted great interest due to the structural similarity between carbon (graphite and diamond) and boron nitride (BN in hexagonal and cubic phases) [170]. Cubic BCN (*c*-BCN) is expected to combine the superhardness of diamond and the high oxidation resistance of *c*-BN [171-173]. Cubic BC_2N synthesized at HPHT presents an *H* value of 75 GPa, which is even higher than that of *c*-BN [172]. However, the theoretical work reported later argued that the predicted hardness of the optimal BC_2N structure cannot reach that of *c*-BN, and the

superhardness obtained in the experimental work is due to the formation of nanocrystals in the amorphous carbon matrix [173]. The superhard cubic phase could only be produced by the HPHT method. BCN coatings deposited by various vacuum-based techniques were widely investigated with respect to the mechanical properties of the films, but their hardness did not reach the superhard level [174-176].

Hexagonal BCN (*h*-BCN) presents tunable electrical properties that fall between those of semi-metallic graphite and insulating hexagonal BN (*h*-BN) [177]. C and BN phase segregation is commonly observed in *c*-BCN films as mentioned above [178, 179]. The synthesis of the ternary *h*-BCN phase is confirmed by X-ray absorption near-edge spectroscopy (XANES) [180]. *h*-BCN was reported as a p-type semiconductor with a band gap strongly depending on the elemental composition [181-183]. T. Yuki et al reported that polycrystalline BCN films can be synthesized by PECVD at a substrate temperature of 650 ºC [181]. As the carbon content of the BCN films is increased from 9% to 30%, the band gap decreases from 5.3 to 3.4 eV as shown in Figure 2.18 (a), and the electrical resistivity decreases from 1×10^{12} to 3.4×10^{9} Ω·cm [181]. BCN films deposited by RF magnetron sputtering at lower substrate temperature exhibit a smaller band gap. The band gap value decreases from 2.0 to 1.5 eV as the substrate temperature is reduced from 550 to 250 ºC, as shown in Figure 2.18 (b) [117].

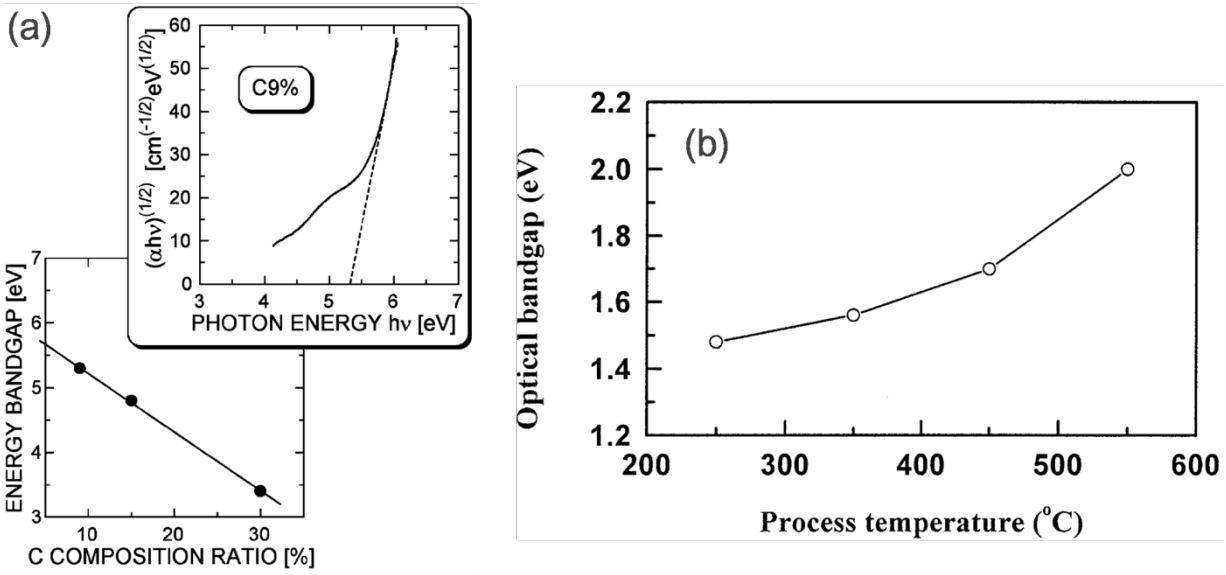

Figure 2.18 (a) Band gap values of the BCN films deposited by PECVD at a T_s of 650 ºC as a function of carbon content. The inset shows $(\alpha h\nu)^{1/2}$ plotted as a function of $h\nu$, adapted from [181]; (b) Band gap values of the BCN films deposited by RF magnetron sputtering at different T_s from 250 to 550 ºC. Adapted from [117].

CHAPTER 3 EXPERIMENTAL METHODOLOGY

In this chapter we describe the experimental methodology applied in this work including the deposition and characterization techniques. First, the working principle of magnetron sputtering and the deposition systems used in this work are briefly introduced. Then, we offer an overview of the fundamentals of the compositional and microstructural characterization techniques and their specification for different applications. The characterization methods for mechanical, tribological, and corrosion properties are addressed in the third part.

3.1 Magnetron sputtering deposition

3.1.1 Sputter deposition

Plasma is defined as a partially ionized gas that contains a collection of electrons, ions, and neutral atomic and molecular species, and it is described as the fourth state of matter. It can be induced in gases by supplying high energy (thermal energy, electric energy, or electromagnetic radiation) into the gas systems. Electrical discharges are commonly used to generate plasma in laboratories and industrial plants. The discharges can be divided into three general types including the dark discharge, the glow discharge, and the arc discharge. Sputtering deposition is commonly carried out in the abnormal glow discharge where the energy of ions can be controlled well, and Ar is commonly used as the working gas.

During the sputtering process, electrical energy can be transmitted to the charged particles in the glow discharge plasma via electric fields. The charged particles are accelerated by the electric fields to sputter the target surface. Then, the surface atoms are emitted as a result of the momentum transfer from the bombarding particles to the surface atoms. Finally, the sputtered particles, atoms, or more complex surface constituents condense on the substrate to form a thin film.

Magnetron sputtering is extensively used in sputter deposition as it can provide a high deposition rate and the feasibility of manipulating the film properties within large ranges. In general, crossed magnetic and electric fields are applied on the targets as shown in Figure 3.1. The electrons can be trapped in the vicinity of the target surface by the Lorentz force. As a consequence, the elongated electron trajectories can enhance the ionization efficiency, and thus

lead to higher ion current density and sputtering rate. Particularly, unbalanced magnetron sputtering is preferable in practice. Unbalance magnetrons are designed with two magnets (central and external magnets, e. g., in planar configuration) having unequal strength of magnetic field. When the outer magnet is stronger than the central magnet, not all the magnetic field lines are closed between the central and outer magnets, but some are directed towards the substrate. As a consequence, the resulting, more open, magnetic lines trap secondary electrons, which yields higher ionization and higher ion currents. This arrangement gives rise not only to a higher sputtering yield but also provides more economical use of the target, and enables us to form a closed magnetic field configuration assembled from multiple magnetrons confining the plasma in the region of interest.

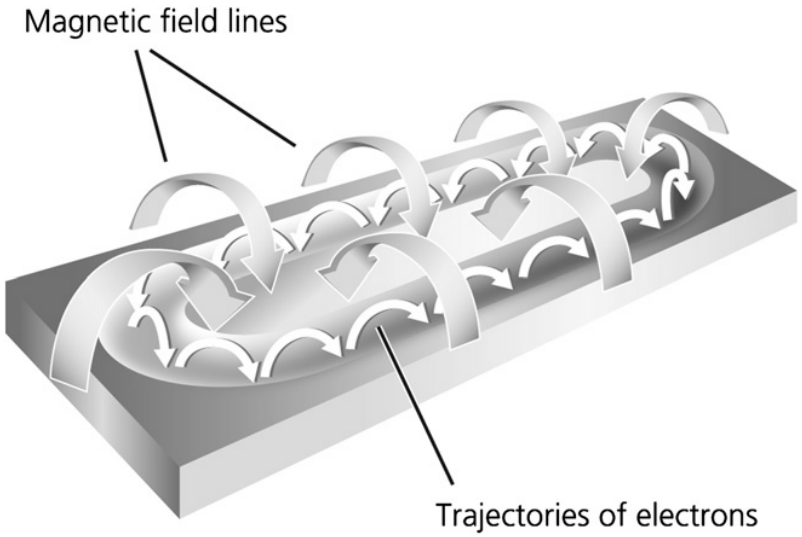

Figure 3.1 The working principle of magnetron sputtering. Electrons are restrained near the target surface by the Lorentz force in an inhomogeneous magnetic field, leading to an enhanced ionization of argon atoms. Adapted from [184].

The magnetrons can operate in different modes, including DC, AC, RF, and pulsed DC modes. The most simple and least expensive way to operate the magnetron is using a DC power mode, which is widely used for metal deposition. However, when the cathode is an insulator, DC discharge cannot be induced. This problem can be solved by the operation of magnetrons, for example, in an RF mode.

When a two-electrode diode system or a magnetron operates at high frequencies, typically at 13.56 MHz, an electrically insulating target with suitable thickness is able to develop a negative

self-bias potential on its surface, which can be explained by a leaky *I-V* characteristic of the RF plasma as presented in Figure 3.2. The electrons in the RF plasma with low-mass, respond considerably faster to the rapidly varying electric field, than heavier ions, which are inertially confined. During the positive half of the cycle, a very large current flows to the insulating positively charged electrode. During the other negative half of the cycle only a small ion current flows into the electrode. As no charge can be transferred through the capacitor, a steady state is achieved when the electrode is negatively charged, self-bias develops, and the net current is zero as shown in Figure 3.2. Consequently, the insulating electrode is under continuous bombardment by positive ions, and works as a capacitive coupling with plasma.

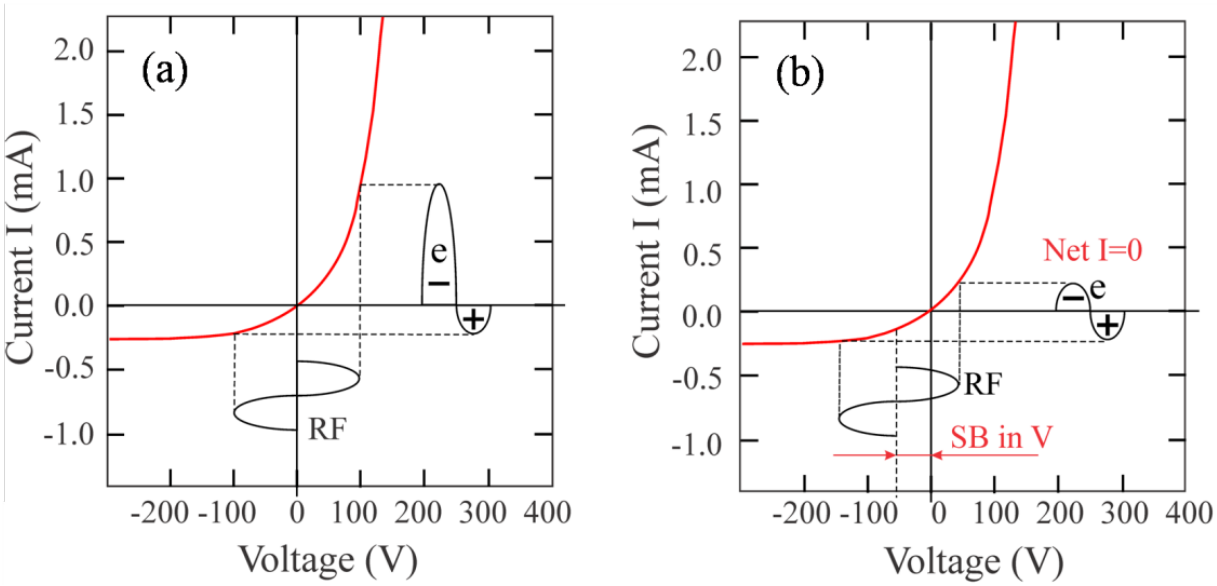

Figure 3.2 Formation of a dynamic equilibrium of zero net current and negative self-bias of cathode with capacitive coupling at operation of deposition system in an RF mode: (a) Initial state; (b) Steady state.

Application of a pulsed DC power supply is an effective way to avoid arcing during reactive magnetron sputtering. Compared to RF magnetron sputtering, the repetition frequency of pulsed DC is much lower, typically in the range from 50 to 250 kHz, in accordance with the application [185]. Generally, the discharge voltage cycles between a high negative voltage and a low positive voltage. Sputtering takes places at the negative voltage is due to ions bombarding the target, while the low positive voltage attracts electrons, neutralizing the positively charged target surface.

Due to the higher mobility of electrons, the positive voltage part is relatively short compared to the total cycle time.

3.1.2 Deposition systems

In our experiment, $B_{1-x}C_x$ and Ti−B−C coatings were deposited using a pilot-scale closed-field unbalanced magnetron sputtering deposition system (UPD 450, Teer Coatings Ltd.), which is schematically shown in Figure 3.3. The deposition chamber was equipped with four rectangular planar (with a size of 330 mm×133 mm) unbalanced magnetrons in a 4×90º configuration and a cylindrical substrate holder rack 70 mm from the targets. One graphite target, one TiB_2 target, and two boron targets were used in this work. The graphite and TiB_2 targets were powered by DC power supplies, and the other two boron targets were powered by pulsed DC power supplies (350 kHz, 1 μs). The distance between the targets and the substrate was 70 mm. The cylindrical substrate holder rack was rotating at 10 rpm during the deposition to avoid layered structure and provide a homogeneous compound.

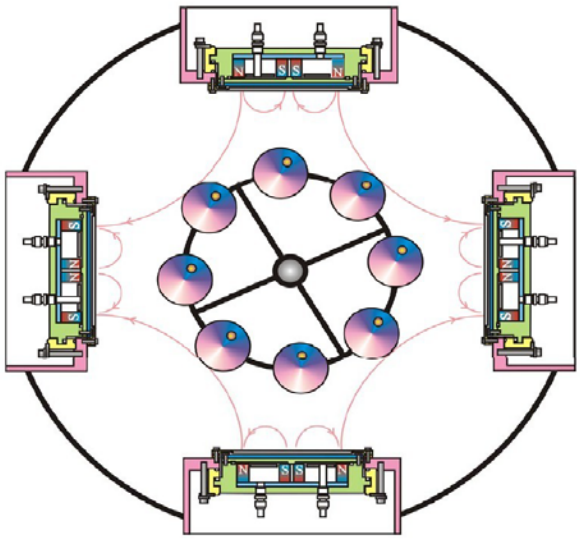

Figure 3.3 Schematic of the magnetron sputtering deposition system (UPD 450, Teer Coatings Ltd.) used to deposit the $B_{1-x}C_x$ and Ti−B−C films in this work.

Prior to deposition, all the substrates were ultrasonically cleaned in baths of a detergent (Decon 90), ethanol, and deionized water. A turbomolecular pump backed by a rotary pump was employed to evacuate the vacuum chamber down to a background pressure lower than 1.0×10^{-4} Pa. The substrate surface was sputter-cleaned for 30 minutes in Ar plasma at 250 kHz using a

bias of −450 V. Sputtering deposition was carried out in Ar plasma at a pressure of 1.86×10^{-1} Pa with an Ar flow rate of 15 sccm (2.72×10^{-2} Pam^3/s at 20 ºC). The substrate was biased at −60 V during the deposition, while the substrate temperature was maintained at ~200 ºC.

The BCN films were deposited by RF magnetron sputtering using a different deposition system, the schematic of which is presented in Figure 3.4. A single B_4C target (three inches in diameter) was powered by an RF power supply at a frequency of 13.56 MHz. Prior to deposition the system was pumped down to a background pressure of $<1.0\times10^{-4}$ Pa, and the sputtering was carried out in a gas mixture of N_2:Ar with a total flow rate of 10 sccm at a pressure of 0.4 Pa. An RF power of 200 W was applied to the B_4C target, while the substrates were electrically grounded.

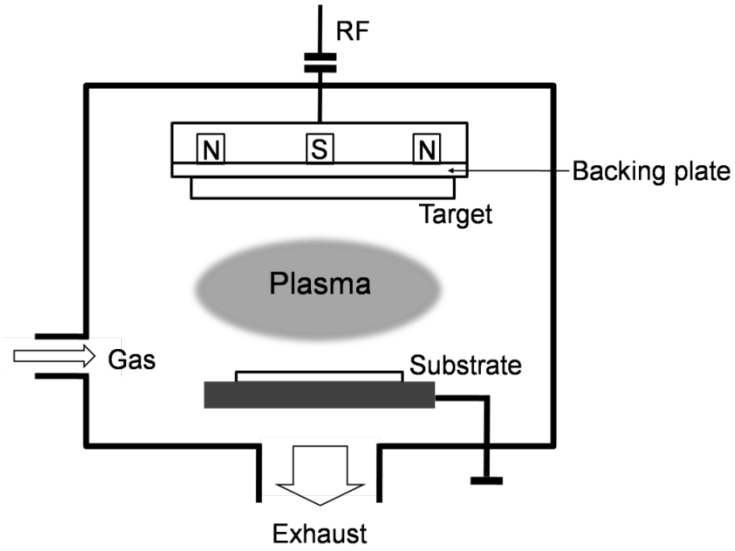

Figure 3.4 Schematic of the RF magnetron sputtering deposition system equipped with single target used for the BCN film deposition in this work.

3.2 Compositional and microstructural characterization

3.2.1 Morphology characterization

Optical microscopy is a technique widely used to evaluate the morphology and structure of thin films. Optical microscopes are also integrated into other characterization instruments, such as tribometers and nanoindenters. After a pin-on-disk test or nanoindentation test, optical

microscopy is commonly employed to examine the damage of coating surfaces. For general optical microscopy, the maximum magnification is ~1200×.

Like optical microscopy, scanning electron microscopy (SEM) is an imaging technique visualizing surfaces, but on a broader scale, from submilimeters down to ~1 nm. Instead of using photons, SEM uses a focused electron beam to obtain images by collecting secondary electrons, the intensity of which corresponds to the topographic level. The spatial resolution of SEM is much higher than that of optical microscopy due to the very short wavelength of electrons.

In this work, a Nikon optical microscope and a SEM (JEOL JSM840) equipped with an energy dispersive X-ray spectrometry (EDS) were employed to evaluate the film thickness, the topography of the wear tracks, and the composition of the films.

3.2.2 Structural and compositional characterization

Generally, thin film structure is determined by combining different techniques, such as X-ray photoelectron spectroscopy (XPS), Fourier transform infrared spectroscopy (FTIR), Raman spectroscopy, and X-ray diffraction (XRD). In this work, all of these were used in different combinations.

It is instructive to consider the interaction volume of electrons and the escape volumes of different signals, which are the fundamentals of the working principles of many surface analytical techniques including EDS and XPS. As energetic electrons impact on a specimen surface, various signals carrying different information can be generated in a pear-like interaction volume as shown in Figure 3.5. For instance, the secondary electrons are characteristic of topographic contrast as mentioned above, the scattered electrons yield the atomic contrast, and the characteristic X-rays are unique to different chemical elements. The spatial and depth resolutions of the analytical techniques based on these three typical signals are determined by their own escape volumes as illustrated in Figure 3.5. Obviously, analytical techniques based on X-ray detection have the poorest spatial resolution since the lateral size of its escape volume is the largest among all the indicated signals.

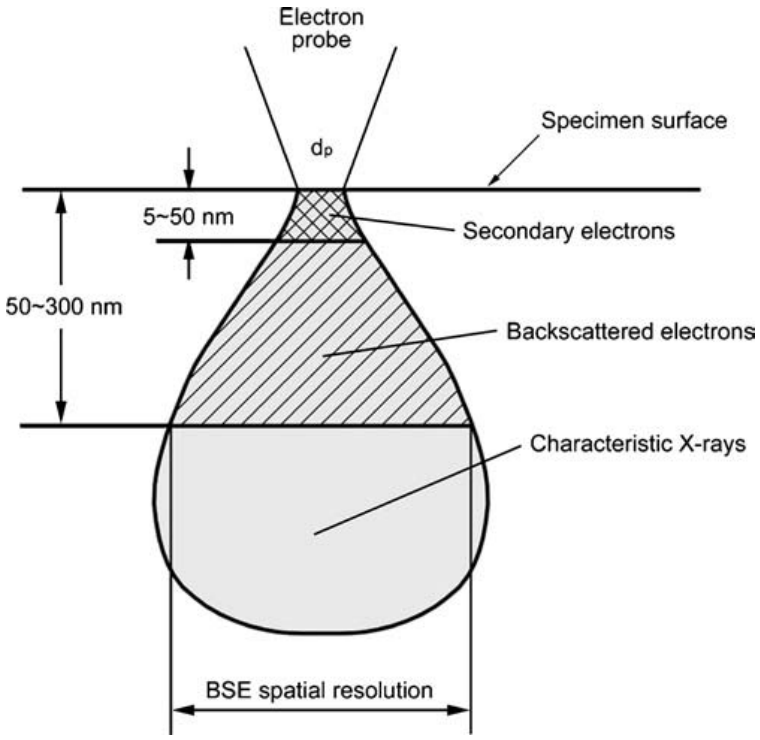

Figure 3.5 Interaction volume of electrons and specimen atoms below a specimen surface, and the escape volumes of different signals. Adapted from [186].

- **XPS**

XPS is a spectroscopic technique providing information on the chemical states and composition. Its working principle can be described as follows. When a sample surface is irradiated by X-ray photons, photoelectrons will be ejected from the surface atoms as illustrated in Figure 3.6. In general, Al Kα (1486.6 eV) and Mg Kα (1253.6 eV) X-ray photons are employed for photoelectron excitation. The emitted photoelectrons are analyzed by an energy analyzer to determine their kinetic energy (KE). Then, the binding energy (BE) of the photoelectrons can be calculated using

$$BE = h\nu - KE - \Phi_{\text{spectrometer}} \ , \tag{3.1}$$

where $h\nu$ is the energy of the incident X-ray photon (h is Planck's constant, and ν is the frequency) and $\Phi_{\text{spectrometer}}$ is the work function of the spectrometer. The binding energy values of the photoelectrons are unique to the chemical elements, so they can be used to identify the elements and to study the material composition. Due to the very shallow analysis depth of XPS (< 10 nm), the measured composition and chemical states are confined to the very top layer of the surface,

which may differ from the bulk chemical properties. Therefore, Ar sputter cleaning is commonly used to remove the adventitious hydrocarbon and oxygen based contaminants, from the sample surface before analysis.

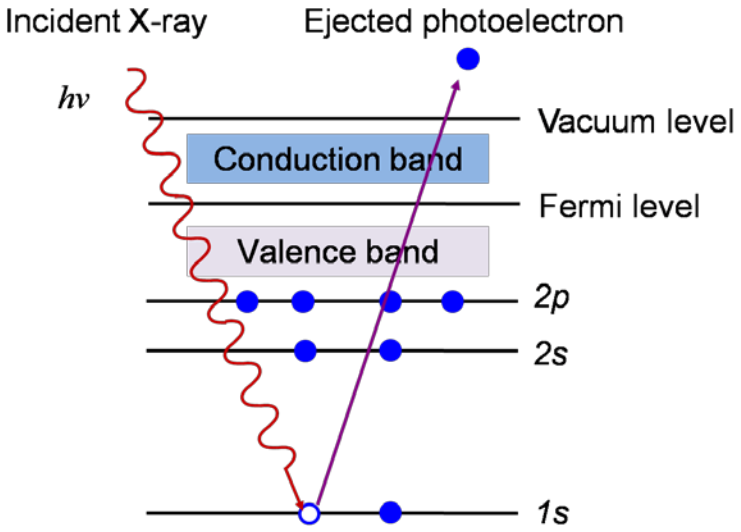

Figure 3.6 Schematic diagram of photoelectron emission process induced by X-ray irradiation.

XPS can also provide quantitative analysis, which means the concentrations of chemical elements can be calculated by examining and processing the peak intensities. The atomic concentration, X_i, can be calculated by a semiempirical equation

$$X_i = \frac{I_i / S_i}{\sum I_i / S_i}, \tag{3.2}$$

where I_i is the peak intensity and S_i is the sensitivity factor. S_i for each element is experimentally determined and varies with conditions of the instrument and sample surface.

In this work, the XPS spectra were obtained using a VG ESCALAB 220i-XL ultrahigh vacuum (UHV) surface analytical facility equipped with a monochromatic Al Kα (1486.6 eV) X-ray source. All the samples were sputter-cleaned by Ar ion beam with an energy of 3 keV at an angle of 30º before collecting the XPS spectra.

- **Raman and FTIR**

Raman spectroscopy and the FTIR are in the category of vibrational spectroscopies, which use optical methods to analyze the molecule structure by examining the interaction between

electromagnetic radiation and molecular vibrations. They are extensively used in material characterization, particularly for evaluation of molecular structure and composition.

Infrared spectroscopy is based on the infrared radiation absorption by molecules and the subsequent induced vibrations, which are characteristic of molecular structure and chemical bonding [186]. The energies of the radiation near infrared and visible light are not high enough to excite electronic levels, but their frequencies match that of molecular vibrations. Therefore, such radiation is able to change status of molecular vibrations. The vibrational energy of a molecule can be described as

$$E_{\text{vib}} = h\nu_{\text{vib}}(\upsilon + \frac{1}{2}) , \qquad \upsilon = 0,1,2,... \tag{3.3}$$

where υ is the vibrational quantum number, and ν_{vib} is the vibrational frequency of a molecule. When the frequency of photons, ν, is equal to ν_{vib}, the molecular vibration is excited as reflected by $\Delta\upsilon = 1$. In the meantime, the photon energy is transferred to excite molecular vibrations, which means the radiation with the frequency of ν is absorbed by the molecule. Therefore, the infrared absorption is dominated by the fundamental transition from $\upsilon = 0$ to $\upsilon = 1$, although other transitions may be probable as well.

Raman spectroscopy is based on the Raman effect which is a specific form of the inelastic scattering of light. When a specimen is irradiated by light, both elastic and inelastic scattering can take place. The difference between elastic and inelastic scattering relies on the relationship between the frequencies of the incident and of the scattered light. Elastic scattering means that the frequency of the scattered light is the same as that of the incident light. The inelastic scattering implies the frequencies of the scattered light and of the incident light are different.

Figure 3.7 illustrates the elastic and inelastic scattering in terms of energy transfer between photons and molecules. The molecular vibration can be excited to a higher level by photons, when $\nu = \nu_{vib}$. If the excited vibration returns to its initial level without any energy transfer, the frequency of the scattered photons is preserved, which is called Rayleigh scattering as shown in Figure 3.7 (a). In contrast, when the excited molecular vibration does not return to its initial level, Raman scattering takes place and the energy of the scattered photons can be either lower or higher than that of the incident photons. If the final energy level of molecular vibration is higher as shown in Figure 3.7 (b), the process is termed as Stokes scattering, whereas, when the final

energy is lower than the initial energy, the process is named as anti-Stokes scattering as shown in Figure 3.7 (c). Generally, a Raman spectrum records the frequency changes induced by the Stokes scattering because it has a much higher intensity compared to that of anti-Stokes scattering. Such frequency change is called Raman shift in Raman spectra.

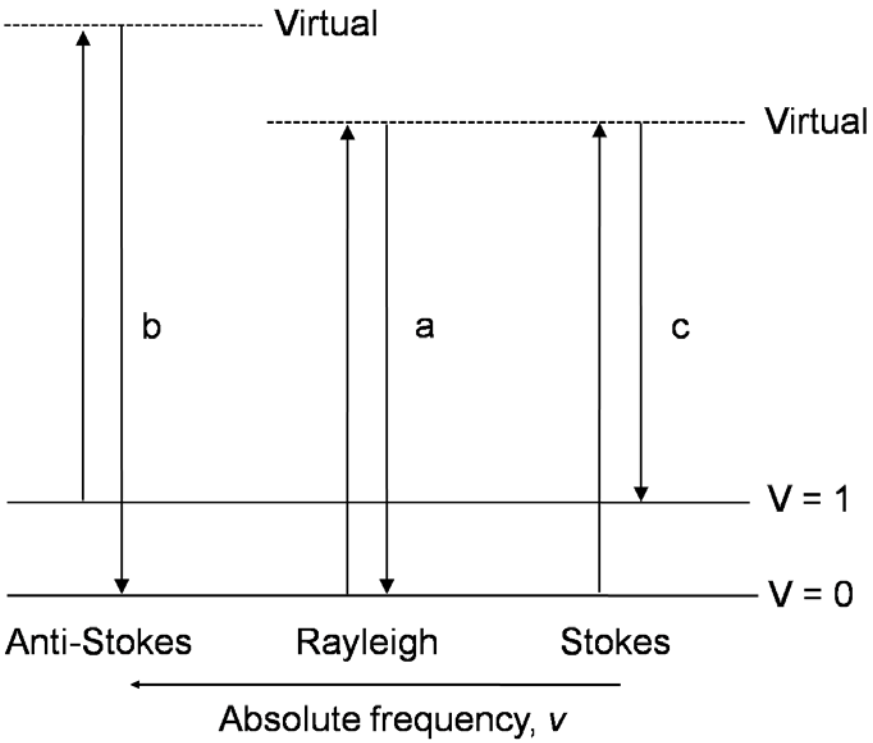

Figure 3.7 Elastic and inelastic scattering of incident light by molecules including Rayleigh, Stokes, and anti-Stokes scattering. Modified from [187].

Raman and IR spectra are complementary to each other. Generally, Raman spectroscopy is good at analyzing symmetric or in-phase vibrations and non-polar groups. On the contrary, FTIR is efficient in studying the asymmetric or out-of-phase vibrations and polar groups. Therefore, in this work the C−C bonds in the boron carbide films were studied by Raman spectroscopy using a Renishaw inVia Raman spectrometer with an excitation wavelength of 633 nm. In addition, FTIR (FT-IR 1600, Perkin-Elmer) was used to identify the boron nitride phase in the BCN films.

- **XRD**

X-ray diffraction is commonly used to determine the crystallographic characteristics of materials. In Figure 3.8, an incident X-ray with wavelength of λ is diffracted by crystallographic planes at specific diffraction angle, θ, following Bragg's law

$$2d \sin\theta = n_1 \lambda \ , \tag{3.4}$$

where d is the interplanar spacing, and n_1 is an integer. Therefore, with the wavelength of the X-ray and the incident angle, the spacing between the equivalent crystalographic planes can be calculated, and the crystalline phases can be identified by comparison with material databases.

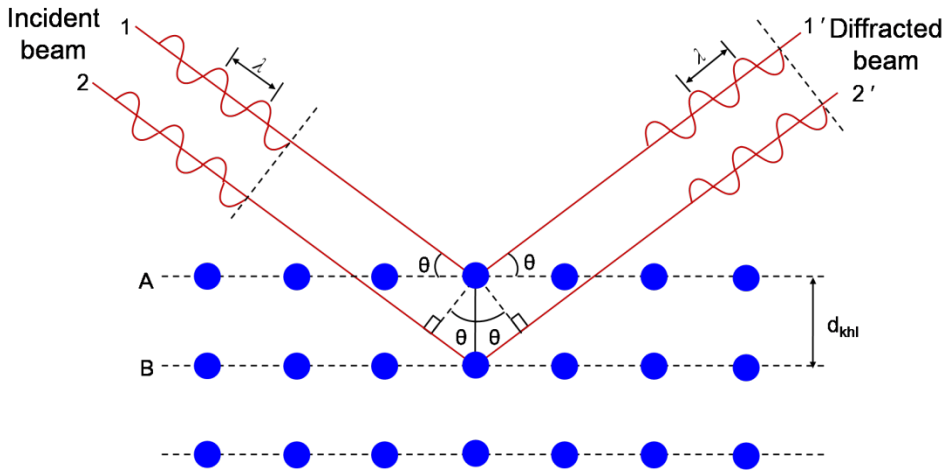

Figure 3.8 Bragg diffraction by crystallographic planes. Modified from [186].

Diffractometers with Bragg−Brentano configuration (see Figure 3.9) are widely used in practice, as the diffraction angles can be well-defined for finite slit widths and beam divergences. In such geometry, the X-ray tube and the detector are on the circumference of a circle with the sample in the center, and accordingly, the diverging incident rays from the X-ray tube can be refocused on the detector due to the specific geometry. Consequently, good intensity and instrument resolution can be achieved. In general, the characterization of thin film structure is performed at a small incident angle of the incoming X-ray to increase the interaction depth of the X-ray and avoid the diffraction signal from the substrate. The crystallite size can be estimated from the FWHM of the diffraction peaks, while the stress level can be deduced from the shift of diffraction peaks.

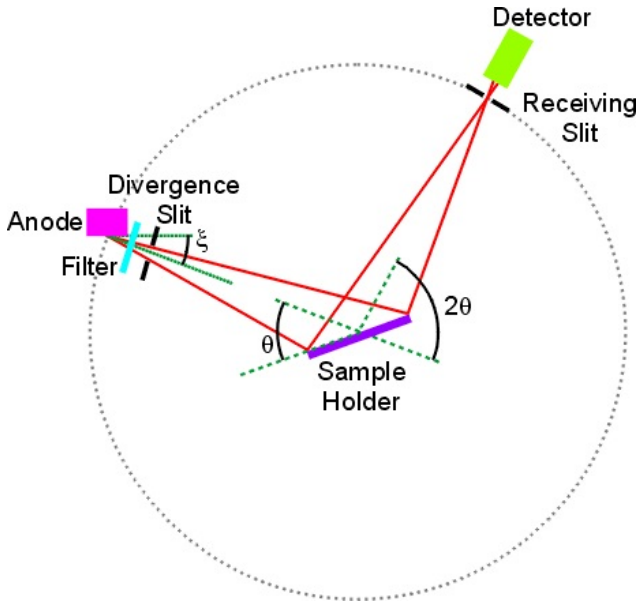

Figure 3.9 Geometry of a Bragg–Brentano diffractometer. Adapted from [188].

In this work, a Philips X'Pert X-ray diffractometer with Cu Kα radiation was employed to collect XRD patterns, and all the measurements were performed at a grazing angle of 2° in a Bragg−Brentano configuration.

- **EDS**

EDS is generally integrated in the SEM system to obtain compositional information. As mentioned above, characteristic X-rays can be induced when an electron beam probe interacts with the specimen surface. The emitted characteristic X-rays act like finger prints for each element since the energy of the characteristic X-rays is dependent upon the atomic number and is unique for each element. As their intensities are proportional to the atomic concentration, they can be used for compositional analysis as well. The spectral resolution of EDS typically ranges from 150 to 200 eV. Elements with atomic numbers smaller than 8 cannot be well identified by EDS because the X-rays with low energy are fully or partially absorbed by the solid state detectors and their windows.

- **Rutherford backscattering spectroscopy (RBS)**

RBS is significantly different from the previous characterization techniques. Instead of using electromagnetic waves to assess the composition and structure of materials, RBS uses ion beams as probes to perform material characterization including the composition and the density of bulk

materials. RBS is a quantitative analysis technique that does not require standards. In RBS, the specimen is probed by a highly energetic (on the order of MeV) and monoenergetic ion beam, and the energies of the backscattered ions are measured. According to the mechanistic theory, the backscattered energy is a function of the atomic number of the collided atoms from the specimen and the scattering angle. For RBS analysis He^{++} (alpha particles) beams are generally used as the probes, and the scattering angle typically is 170º with respect to the ion beam direction.

3.3 Mechanical, tribological, and corrosion characterization

3.3.1 Mechanical characterization

The mechanical properties, denoted by *H* and *E*, of hard coatings are generally evaluated by indentation techniques, such as microindentation and nanoindentation. Indentation hardness can be calculated by dividing the applied load, *P*, by the projected contact area, A_c, which is essentially the contact pressure when an indenter is pressed into a material's surface. For traditional microhardness testing, A_c is usually measured by optical microscopy after complete unloading; while for nanoindentation measurement, the size of the residual impression is usually too small to measure using optical techniques. Hence, depth-sensing indentation was developed and has been extensively applied for hardness measurement. In such procedure, the depth of penetration, h_{depth}, beneath the specimen surface is measured with applied load, and the size of contact area can be calculated by the depth of penetration when the geometry of the indenter is known. Three-sided Berkovich indenters are commonly used in nanoindentation due to the high accuracy of their face angles and the sharper tips compared with four-sided Vickers indenters used for microindentation. During the depth-sensing indentation testing, a load is progressively applied up to a maximum value and the tip is then retracted; meanwhile the load and the displacement are continuously monitored and recorded. For each depth, a load-displacement curve can obtained as shown in Figure 3.10 (b), from which *H* and *E* can be extracted.

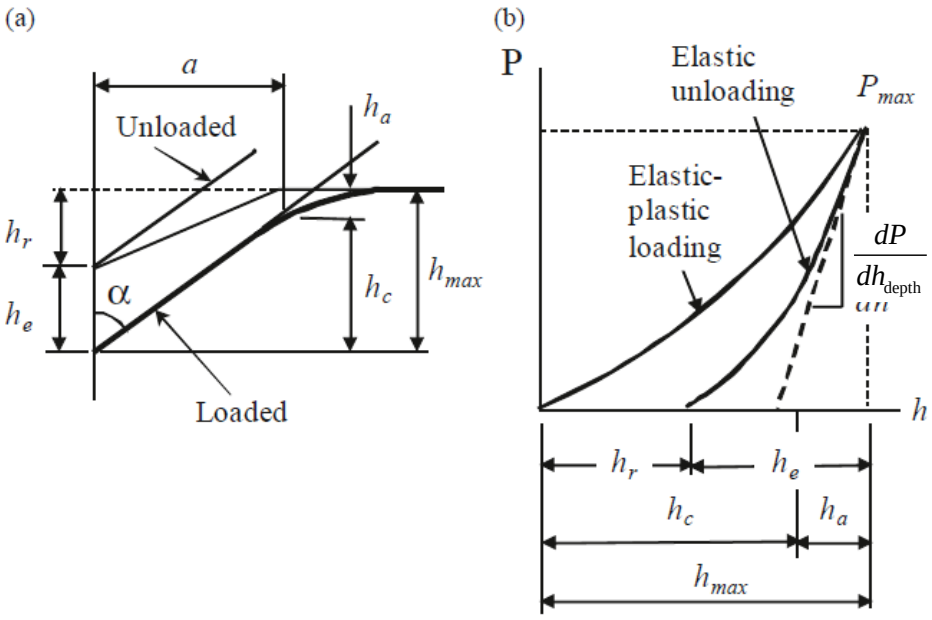

Figure 3.10 Depth-sensing indentation: (a) cross-section profile of sample surface at full load and unload; (b) typical load-displacement curve. Adapted from [189].

In general, the loading process during indentation test results in both elastic and plastic deformation of the specimen material, whereas the unloading process involves only elastic response as illustrated in Figure 3.10. The stiffness defined as

$$S = \frac{dP}{dh_{\text{depth}}}, \tag{3.5}$$

is used for the calculation of reduced modulus, E_{r}, using

$$E_{\text{r}} = \frac{S\sqrt{\pi}}{2A_{\text{c}}}. \tag{3.6}$$

E_{r} is the combined elastic modulus of the contacting indenter and specimen, and their relationship can be described by

$$\frac{1}{E_{\text{r}}} = \frac{(1-\nu_{\text{s}}^2)}{E_{\text{s}}} + \frac{(1-\nu_{\text{i}}^2)}{E_{\text{i}}}, \tag{3.7}$$

where E_{s} and E_{i} are elastic moduli of the sample and of the indenter, and ν_{s} and ν_{i} are the Poisson's ratios of the sample and the indenter, respectively [189]. E_{r} is dominated by the elastic properties of the specimen since the stiffness of the indenter, typically diamond, is very high and the effect of the Poisson ratio is very small.

The most widely used model for the stiffness calculation was proposed by Oliver and Pharr [190]. The load-displacement data, P and h_{depth}, are fitted by

$$P = B(h_{depth} - h_r)^m , \tag{3.8}$$

where h_r is the depth of the residual impression as shown in Figure 3.10, and B and m are fitting constants. The stiffness at the maximum load can be calculated by differentiating the Eq. (3.8) using h_{max}, which is the maximum depth from the original specimen surface at full load of P_{max}.

In addition to H and E, the energy dissipation can be estimated from the load-displacement curve as well. The energy dissipated in the testing material caused by plastic deformation, W_p, is represented by the area between the loading and unloading curves; in contrast, the energy due to elastic deformation, W_e, corresponds to the area under the unloading curve [191]. The elastic recovery is then calculated as

$$R = W_e / \left(W_p + W_e \right). \tag{3.9}$$

Nanoindentation is extensively used for thin film hardness measurement because the substrate effect can be avoided by small penetration depth. Here the H and E values of all films were determined by depth-sensing nanoindentation using a triboindenter (Hysitron) system equipped with a Berkovich pyramidal tip. A fused silica standard was used to calibrate the tip geometry and compliance before testing. All the measurements were performed on films prepared on Si substrates while applying a maximum load of 5 mN. The data were analyzed using the Oliver and Pharr method as mentioned above [190], and the hardness was determined at a penetration depth less than 10% of the film thickness to diminish the substrate effect.

3.3.2 Tribological characterization

Usually, the tribological properties (μ and K) are measured by tribometers, which can be constructed in different configurations and geometries, such as the pin-on-flat and the pin-on-disc used for sliding tests as shown in Figure 3.11. Both of these two types of tribometers consist of a pin or ball under an applied load in contact with a plate or disk, but the relative motions of the two counterparts are different. For pin-on-flat tribometer, the plate is stationary, while the pin moves in a reciprocating mode as shown in Figure 3.11 (a), whereas the pin-on-disk tribometer is composed of a stationary pin in contact with a rotating disk as shown in Figure 3.11 (b). The

applied load and the sliding speed can be adjusted, and the collected frictional force is used for the calculation of μ. The volume loss can be measured by a depth profilometer in order to evaluate the wear rate.

In this work, both types of tribometers were employed to analyze the tribological properties of the films. Usually, a normal force of 2 N was applied to an alumina ball, 6.35 mm in diameter, being used as a counterpart material. In addition to the measurement of μ and K, the morphology and composition of the wear tracks as well as the debris were examined by the combination of optical microscope, SEM, and EDS to study the tribological mechanisms.

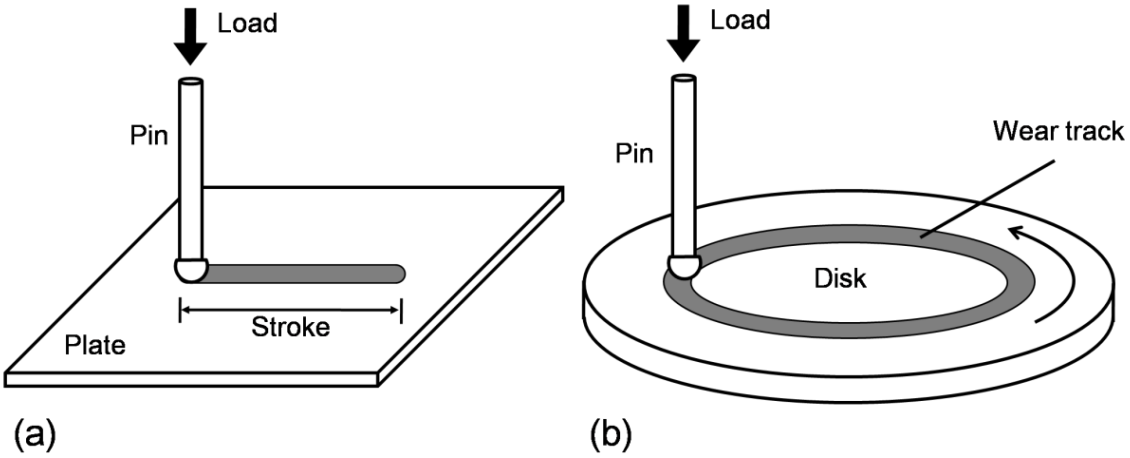

Figure 3.11 Two types of tribometers in different configurations: (a) pin-on-flat used in reciprocating sliding tests; (b) pin-on-disk used in rotating sliding tests.

3.3.3 Corrosion characterization

A potentiodynamic polarization test can be used to investigate the corrosion properties of materials. The corrosion tests are usually carried out in a three-electrode corrosion cell as shown schematically in Figure 3.12. The sample serves as a working electrode (WE), and a standard calomel electrode and a graphite rod are used as reference electrode (RE) and counter electrode (CE), respectively. The potential between the WE and RE, and the current between WE and CE can be controlled by a Potentiostat which is connected to the three electrodes.

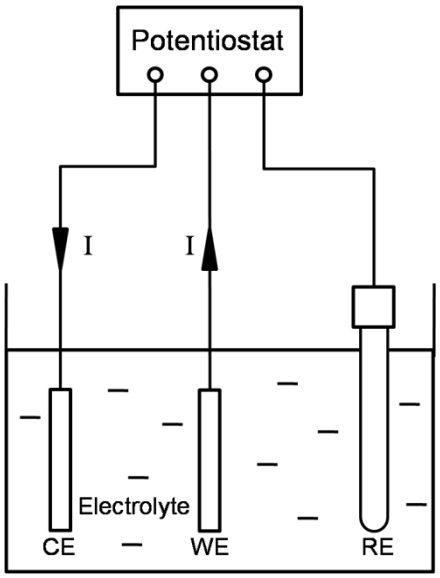

Figure 3.12 Schematic illustration of a three-electrode corrosion cell with a counter electrode (CE), a working electrode (WE), and a reference electrode (RE).

The electrolyte is a conductive solution, such as NaCl in H_2O. In the corrosion process, the current flow is generated by the anodic and cathodic reactions. The anodic reaction is an oxidation process in which the metal is oxidized and dissolved into the electrolyte. On the other hand, the released electrons are consumed by the reduction of the dissolved oxygen, an effect described as cathodic reaction. The electrochemical process in the polarization test occurs at the open circuit potential (OCP), and no external voltage is applied to the sample serving as the WE. Accordingly, no external current other than the corrosion current goes though the WE. In a potentiodynamic polarization test, the potential of the WE gradually increases from a value below the OCP, and the current is monitored and recorded as a function of the potential. In such procedure, the corrosion rate and the corrosion mechanisms can be obtained.

The polarization curve of SS301 in 1 wt.% NaCl solution is shown in Figure 3.13, where two very important parameters for corrosion property evaluation, the corrosion current density, i_{corr}, and the breakdown potential, E_{BD}, are indicated. i_{corr} is defined as the current density at which the anodic and cathodic reaction rates are equal, reflecting the corrosion resistance of the sample. E_{BD} is determined by the potential at which the current increases sharply. This represents the resistance to the initiation of localized corrosion, such as pitting.

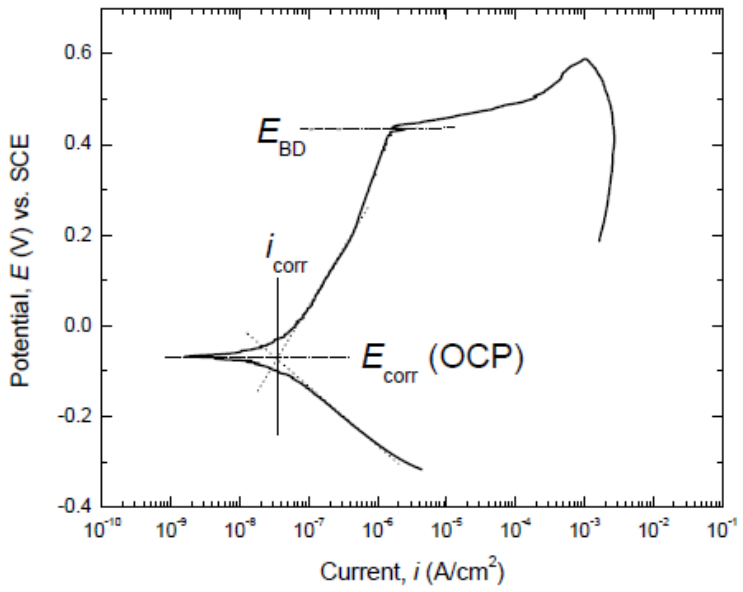

Figure 3.13 Polarization curve of SS301 in 1 wt.% NaCl solution.

In this work, the corrosion properties were measured in 1 wt.% NaCl solution at room temperature using a three-electrode cell equipped with an Autolab PGSTAT302 potentiostat. M2 steel substrates with and without films were exposed to the electrolyte with a circular area of 10 mm in diameter (0.79 cm^2). The electrodes were first stabilized in the electrolyte for 1 hour until a stable open circuit potential (OCP) was reached. Then the potentiodynamic polarization test was performed with a scan rate of 0.001 V/s, while the applied voltage varied from −0.2 V below the OCP to a potential until a current density of 1 mA/cm^2 was reached.

CHAPTER 4 ARTICLE 1: TAILORING THE MECHANICAL AND TRIBOLOGICAL PROPERTIES OF SPUTTERED BORON CARBIDE FILMS VIA THE $B_{1-X}C_X$ COMPOSITION

Article 1: Tailoring the mechanical and tribological properties of sputtered boron carbide films via the $B_{1-x}C_x$ composition

Authors: J. C. Qian, Z. F. Zhou, C. Yan, D. J. Li, K. Y. Li, S. Descartes, R. Chromik, W. J. Zhang, I. Bello, L. Martinu, and J. E. Klemberg-Sapieha*

Article published: Surface and Coatings Technology, **267** (2015) 2.

Abstract

Boron carbide films are very attractive due to their high hardness and interesting tribological properties. In the present work, the compositional effect of boron carbide $B_{1-x}C_x$ ($0 < x < 1$) films is systematically studied to tailor mechanical, tribological and corrosion properties of the films. The $B_{1-x}C_x$ layers were deposited on Si (100) and M2 high speed steel substrates using a pilot-scale closed-field unbalanced magnetron sputtering system equipped with one graphite and two boron targets. Different compositions were obtained by tuning the electrical power applied to the graphite target. The hardness of the $B_{1-x}C_x$ films decreases from 28 to 20 GPa as the carbon content [C] rises from 19 to 56 at.%, but thereafter it increases again up to ~25 GPa when [C] reaches 76 at.%. The hardness variation is explained by changes in the film microstructure, namely formation of either a nanocrystalline boron carbide in the case of boron-rich films, or boron carbide nanocrystals dispersed in an amorphous boron carbide/*a*-C matrix in the case of carbon-rich films as deduced from the combined XPS, micro-Raman and XRD measurements. The friction coefficient of the $B_{1-x}C_x$ films reduces from 0.66 to 0.13, and the wear rate against alumina ball drops from 6.4×10^{-5} to 1.3×10^{-7} mm^3/Nm with increasing the [C]. Raman analyses indicate that improvement of the tribological properties of the $B_{1-x}C_x$ films is primarily caused by the presence of the amorphous carbon phase that leads to the formation of a graphitic tribolayer acting as a solid lubricant during the wear process. Deposition of the $B_{0.81}C_{0.19}$ film with high hardness (28 GPa) improves the corrosion resistance of the M2 steel substrate by four orders of magnitude, documented by the decrease of the corrosion current from 3×10^{-6} to 8×10^{-10} A/cm^2. We demonstrate that adjustment of the x-portion in the $B_{1-x}C_x$ system allows one to tailor the

tribo-mechanical properties over a large range from high hardness/high friction to high hardness/low friction structures.

Key Words: Boron carbide films, Magnetron sputtering, Tribo-mechanical properties, Corrosion resistance.

4.1 Introduction

Boron carbide is well known for its excellent mechanical properties. With its hardness of ~40 GPa, it is the third hardest traditional bulk material at room temperature after diamond and cubic boron nitride, and it is a good candidate for mechanical applications at high temperature due to its high thermal stability [118]. The physical properties such as low mass density of 2.52 g/cm^3 (light weight material), low thermal expansion coefficient of 4.3×10^{-6} K^{-1}, high thermal and chemical stability and good wear resistance, make boron carbide suitable for many industrial applications including hard disks, cutting tools, aerospace components, military armor products and others [18, 120, 121].

The detailed atomic structure of boron carbide is still ambiguous [125] since ^{11}B and ^{12}C cannot be well distinguished by X-ray and neutron diffraction due to their similarity in electron density and nuclear cross-section [125-129]. Its lattice structure is usually idealized as a rhombohedral unit cell, where one $B_{11}C$ icosahedra is located at each node of the lattice, and one linear C−B−C chain connects the nodes along the (111) axis [125, 126]. However, the investigation of Raman spectra of boron carbide with the increasing carbon content showed that boron atoms in the icosahedra and in the chain could be substituted by carbon atoms. Even in monocrystalline boron carbide, small amount of carbon could be observed [133, 192]. As a consequence, the electrical and mechanical properties are affected by the change in carbon concentration and chemical states [193].

Inspired by the attractive properties of the bulk boron carbide material, numerous studies focused on boron carbide films prepared by a variety of deposition techniques such as chemical vapor deposition (CVD) [138-140], magnetron sputtering [141-143], ion beam assisted deposition [144] and pulsed laser deposition [120, 145, 194]. CVD deposited films were studied for their photoelectrical properties [195], while their hardness was found to vary considerably (typically from 22 to 33 GPa [196]) depending on the composition and the deposition parameters;

the high hardness is usually reached when the temperature is very high (> 1000 ºC) [197]. In previous studies, boron carbide films with modulated carbon contents were deposited by reactive magnetron sputtering accompanied by continuously tuning the hydrocarbon gas to adjust the film structure and the mechanical properties [198, 199]. However, addition of the hydrocarbon led to a decrease of hardness due to the trapped hydrogen.

The main aim of the present work is to fabricate $B_{1-x}C_x$ films with x varied over a large range in order to tailor their tribo-mechanical properties. For versatility the films were sputtered from single element targets, boron and graphite. We demonstrate a possibility to tune their hardness, friction, wear and corrosion resistance by controlling the film composition and microstructure.

4.2 Experimental methodology

4.2.1 Deposition of the $B_{1-x}C_x$ films

$B_{1-x}C_x$ films were deposited on Si (100) and high speed steel M2 substrates using a closed-field unbalanced magnetron sputtering system (UPD 450, Teer Coatings Ltd.) comprising four rectangular planar (with a size of 330 mm×133 mm) unbalanced magnetrons in a 4×90º configuration. The $B_{1-x}C_x$ films were obtained from one graphite target and two boron targets operated simultaneously, respectively powered by a DC power supply and two pulsed DC power supplies (350 kHz, 1 μs). A 200 nm TiB_2 interlayer was deposited on the M2 steel substrate prior to the $B_{1-x}C_x$ films using a TiB_2 target powered by a DC power supply. The distance between the targets and the substrate was 70 mm. A cylindrical substrate holder rack rotating at 10 rpm was used to avoid a layered structure and provide a homogeneous compound. The total film thickness was 500 nm and 1μm when deposited on Si and M2 steel substrates, respectively.

Prior to deposition, all the substrates were ultrasonically cleaned in baths of a detergent (Decon 90), ethanol and deionized water. After introduction to the deposition chamber, the substrate surface was sputter-cleaned for 30 minutes with Ar plasma at 250 kHz using a bias of −450 V. The system was pumped down to a background pressure $<1.0\times10^{-4}$ Pa before the deposition. Sputtering was carried out in Ar plasma at a pressure of 1.86×10^{-1} Pa with an Ar flow rate of 15 sccm, (2.72×10^{-2} Pa·m^3/s at 20 ºC). The boron target was sputtered at a constant power density of 2 W/cm^2, while the graphite target power density was varied from 0.4 to 4 W/cm^2. The

substrate was biased at −60 V during the deposition, and the substrate temperature was maintained at ~200 ºC.

4.2.2 Structural and compositional characterization

The $B_{1-x}C_x$ films were analyzed by several complementary techniques; this included: a) surface sensitive (10 nm) X-ray photoelectron spectroscopy (XPS) using a VG ESCALAB 220i-XL instrument equipped with a monochromatic Al Kα (1486.6 eV) X-ray source. Ar ion beam sputtering with 3 keV Ar ions at an angle of 30º was used for 5 minutes to remove adventitious hydrocarbons and other carbon- and oxygen based contaminants adsorbed on the film surface. b) In depth sensitive (about 0.5−1.0 μm) Rutherford backscattering spectrometry (RBS); c) Raman scattering spectra were measured by a Renishaw inVia Raman spectrometer with an excitation wavelength of 633 nm. The scattered light was collected in the backscattering geometry using a high sensitivity ultra-low noise CCD detector. d) The XRD patterns of the $B_{1-x}C_x$ films were collected by a Philips X'Pert X-ray diffractometer with Cu Kα X-rays at a grazing angle of 2° in a Bragg−Brentano configuration.

4.2.3 Mechanical and tribological tests

The hardness (H) and reduced Young's modulus (E_r) of the $B_{1-x}C_x$ films were determined by depth-sensing indentation using Triboindenter (Hysitron) system equipped with a Berkovich pyramidal tip. The measurements were performed on films prepared on Si substrates while applying a maximum load of 5 mN. All the data were analyzed using the Oliver and Pharr method [190], and the hardness was determined at an indentation depth less than 10% of the film thickness to reduce the error caused by substrate.

The friction coefficient, μ, of the $B_{1-x}C_x$ films on the M2 steel substrates was measured by two types of pin-on-disk tribometers, using both linear reciprocating and rotating motion modes. A normal force of 2 N was applied to an alumina ball 6.35 mm in diameter being used as a counterpart friction material. In the reciprocating test, the wear track length, the linear speed and the sliding distance were 7 mm, 2.8 mm/s and 7 m, respectively. In the rotating test, the diameter of the wear track ring was 7 mm, the linear speed was 30 mm/s, and the sliding distance was 50 m. For each sample the friction was expressed by the mean friction coefficient, $\bar{\mu}$, during the 50 m sliding, and the error of μ was estimated by the standard deviation of all the experimental data.

The wear rate K was calculated from the latter measurements as $K = V_{loss}/(F \times s)$, where V_{loss} is the worn volume measured by a profilometer, F is the normal load, and s is the sliding distance. Four measurements of V_{loss} were performed on each wear track in order to reduce the random error.

4.2.4 Corrosion measurements

The corrosion properties were measured in an electrolyte (NaCl 1 wt.% solution) at room temperature using the Autolab PGSTAT302 potentiostat with a three-electrode cell type described elsewhere [200]. $B_{1-x}C_x$ films on the M2 steel substrates were exposed to the electrolyte with a circular area of 10 mm in diameter (0.79 cm^2), while the substrate served as a working electrode. A standard calomel electrode and a graphite rod were used as reference and counter electrodes, respectively. The electrodes were first stabilized in the electrolyte for 1 hour to reach a stable open circuit potential (OCP) to reduce measurement error. Then the potentiodynamic polarization test was performed with a scan rate of 0.001 V/s, while the applied voltage varied from −0.2 V below the OCP to a potential when a current density of 1 mA/cm^2 was reached.

4.3 Results

4.3.1 Chemical composition

In the first part of this work, we evaluate the effect of deposition conditions on the film composition, specifically to control the [C] value. Figure 4.1 shows [C] in the $B_{1-x}C_x$ films as a function of power density applied to the graphite target characterized by both XPS and RBS analyses. Comparing the results collected from these two techniques, it is found that the overall trend of the variation is very comparable for both approaches, but the carbon content measured by XPS is slightly higher than that detected by RBS. Indeed, RBS data are less affected by possible surface contamination by carbon, and they better represent the films' bulk composition. Therefore, the carbon content [C] referred to below is that obtained by RBS. By tuning the graphite target power density from 0.5 to 4 W/cm^2, the $B_{1-x}C_x$ films exhibit [C] change from 19 to 76 at.%. The concentration of oxygen in the $B_{1-x}C_x$ films measured by RBS is around 2 at.%.

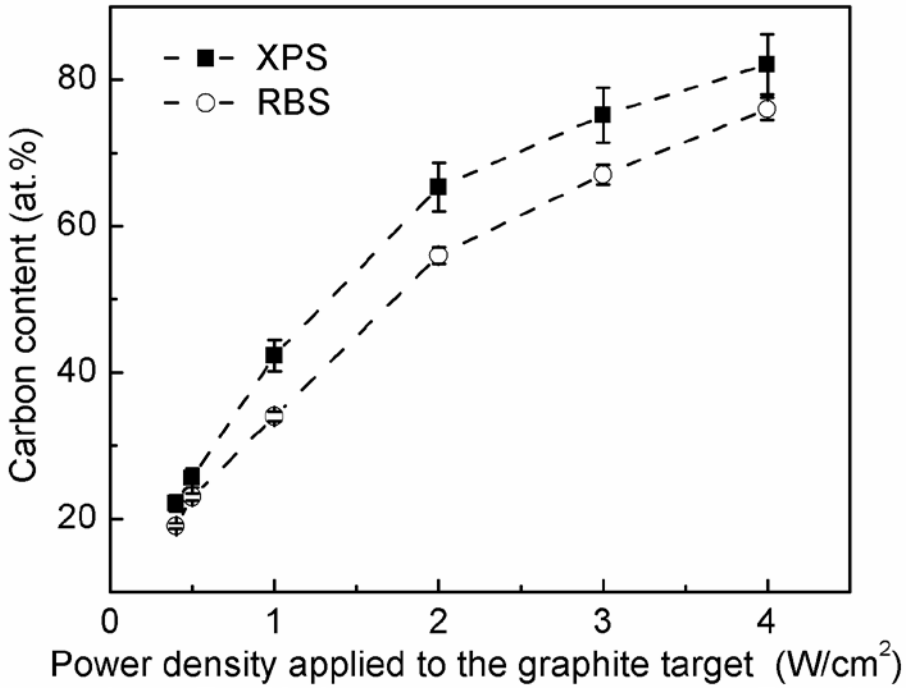

Figure 4.1 Carbon content in the $B_{1-x}C_x$ films as a function of the power density applied to the graphite target as evaluated by the XPS and RBS analytical techniques.

4.3.2 Mechanical properties

The mechanical properties of the $B_{1-x}C_x$ films are presented in Figure 4.2. Figure 4.2 (a) illustrates typical load-displacement curves for $B_{0.81}C_{0.19}$, $B_{0.44}C_{0.56}$ and $B_{0.24}C_{0.76}$ films, while the inset schematically describes the load-displacement curve and the methodology for the determination of the hardness, Young's modulus, and elastic recovery, R. The hardness is defined as the indentation load divided by the projected contact area, $H = P_{max}/A_c$, where P_{max} is the maximum load, and A_c is the projected contact area equal to $24.5h_c^2$ for Berkovich indenter. The reduced Young's modulus can be calculated as $E_r = \frac{1}{2}\frac{\sqrt{\pi}}{\sqrt{A_c}}\frac{dP}{dh_{depth}}$, while the Young's modulus of the coatings can be extracted from the equation $\frac{1}{E_r} = \frac{(1-\nu_s^2)}{E_s} + \frac{(1-\nu_i^2)}{E_i}$, where E_s and E_i are elastic moduli of the sample and of the indenter, and ν_s and ν_i are the Poisson's ratios of the sample and the indenter [190].

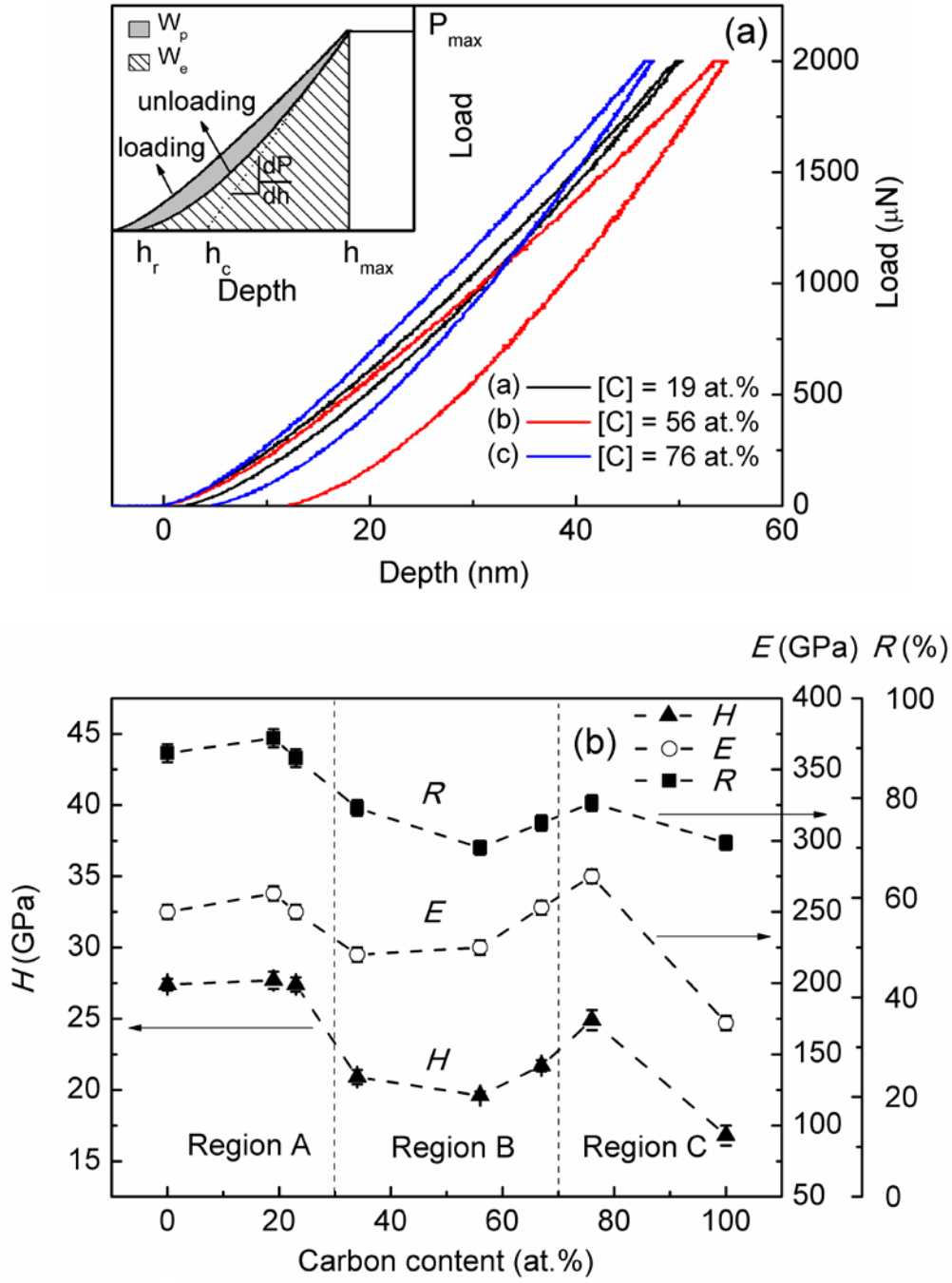

Figure 4.2 (a) Load-displacement curves for the $B_{1-x}C_x$ films with the [C] contents of 19, 56, and 76 at.%; the inset presents a schematic representation of the load-displacement curve, where h_r is the depth of the residual impression, h_c is the contact depth, h_{max} is the maximal penetration depth, P_{max} is the maximum load, W_p is the plastic energy, and W_e is the elastic energy; (b) Hardness, Young's modulus, and elastic recovery of the $B_{1-x}C_x$ films as a function of the carbon content.

The energy dissipated in the material due to plastic deformation, W_p, is represented by the area between the loading and unloading curves; in contrast, the energy due to elastic deformation, W_e, corresponds to the area under the unloading curve [191]. The elastic recovery is then calculated as $R = W_e/(W_p + W_e)$.

The $B_{0.81}C_{0.19}$ film exhibits the highest H value of 28 GPa and a high R of 92%. On the contrary, the $B_{0.24}C_{0.76}$ film with H of 25 GPa shows the smallest penetration depth at the maximum load, indicating high resistance to both plastic and elastic deformation. However, due to a lower R of 79%, the hardness, that is determined as the resistance to plastic deformation, is lower than that for the $B_{0.81}C_{0.19}$ film. The $B_{0.44}C_{0.56}$ film provides the lowest mechanical performance regarding to the combination of hardness, elastic recovery and the penetration depth.

The hardness and the Young's modulus of the $B_{1-x}C_x$ films are plotted in Figure 4.2 (b) as a function of [C]. The H and E values of pure boron and carbon films, deposited from elemental boron and graphite targets, are also shown for reference. According to the variation trend of H and E, the mechanical behavior can be divided in three regions with respect to [C]: (i) region A where [C] < 30 at.%; (ii) region B where 30 at.% < [C] < 70 at.%; and (iii) region C where [C] > 70 at.%. In the boron-rich region A the maximum H of 28 GPa occurs for [C] around 20 at.%. In region B the overall hardness is lower, and it exhibits a minimum of 20 GPa for the $B_{0.44}C_{0.56}$ film. As the carbon content further increases (region C), the hardness reaches 25 GPa ($B_{0.24}C_{0.76}$ film). The overall variation trend of the Young's modulus and the elastic recovery as a function of [C] exhibits a trend similar to that of the hardness. The mechanical behavior is interpreted in terms of the film microstructure in Section 4.4.

4.3.3 Tribological and electrochemical characteristics

In the following we evaluate the tribological properties of the $B_{1-x}C_x$ films in order to assess their performance in the context of protective coating applications. As an example, Figure 4.3 (a) shows the evolution of the friction coefficient as a function of sliding distance for the $B_{0.81}C_{0.19}$, $B_{0.44}C_{0.56}$ and $B_{0.24}C_{0.76}$ films selected from the regions A, B and C indicated in Figure 4.2 (b).

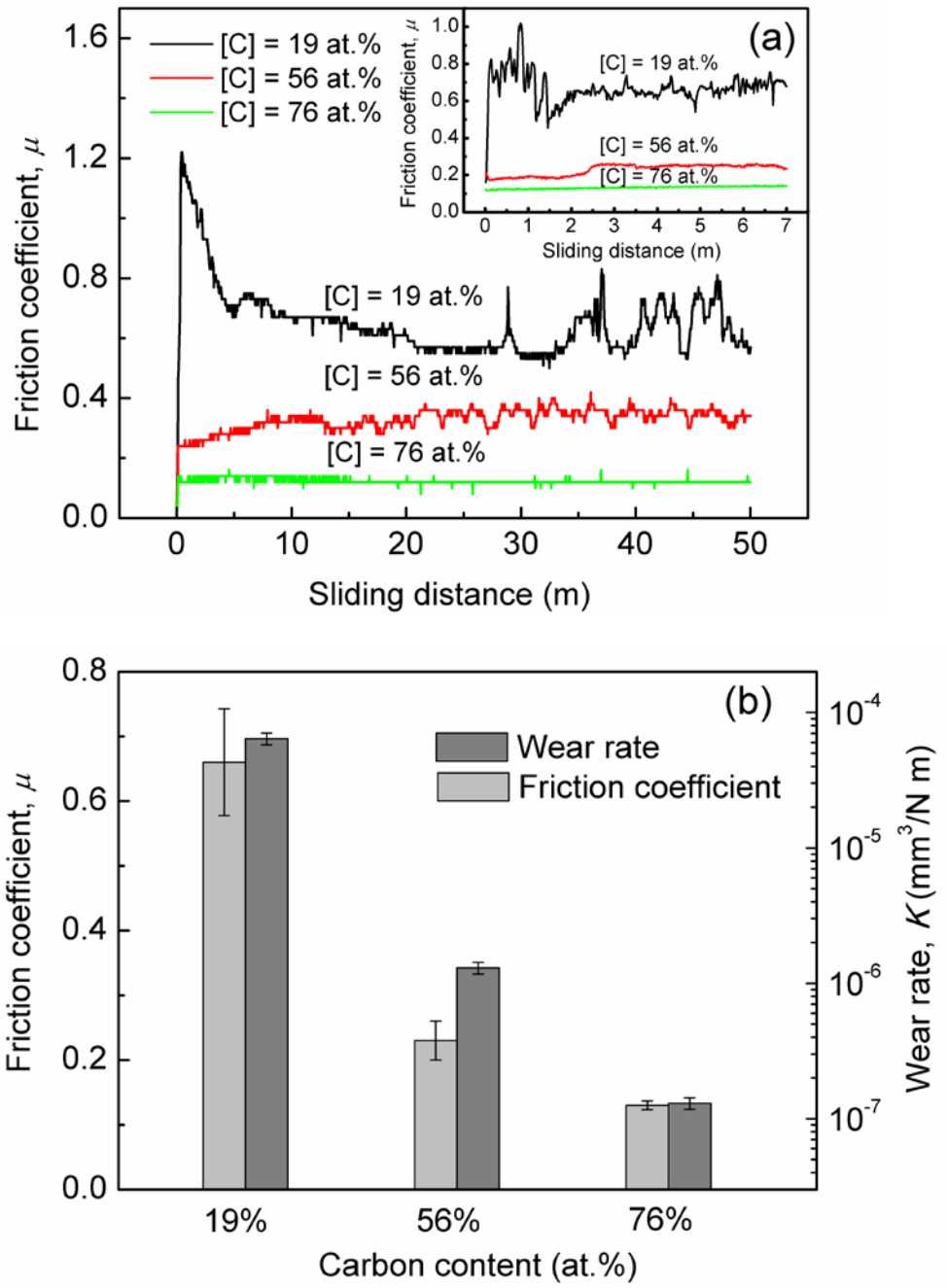

Figure 4.3 (a) Friction coefficient, μ, of the $B_{1-x}C_x$ films with different carbon contents as a function of the sliding distance measured by a rotating pin-on-disk tribometer. The inset shows the data measured by a linear reciprocating tribometers; (b) Wear rate, K, and friction coefficient, μ, of the $B_{1-x}C_x$ films with different carbon contents.

The results obtained from pin-on-disk tests in both rotating and reciprocating modes reveal a similar evolution of the friction coefficient with different carbon contents. In the inset of Figure

4.3 (a), the linear reciprocating test shows that the friction coefficient drops from 0.66 to 0.13 with increasing the carbon content from 19 to 76 at.%.

The wear rate is found to be closely related to the friction coefficient presented in Figure 4.3 (b). As indicated the wear rate decreases by two orders of magnitude from 6.4×10^{-5} to 1.3×10^{-7} mm^3/Nm when the carbon content rises from 19 to 76 at.%.

The corrosion characteristics of the M2 substrate with and without the $B_{1-x}C_x$ films were assessed by the Potentiodynamic polarization as presented in Figure 4.4. Corrosion current density (defined as the current density where the anodic and cathodic reaction rates are equal) and breakdown potential (determined by the potential where the current sharply increases) are very important parameters for the corrosion evaluation. Compared with the bare M2 steel that generally possesses low corrosion resistance, all $B_{1-x}C_x$ films studied here appear to significantly improve the corrosion resistance of the substrate. The $B_{0.44}C_{0.56}$ film (region B) with the lowest hardness decreases the corrosion current by two orders of magnitude from 3×10^{-6} to 6×10^{-8} A/cm^2. The boron-rich $B_{0.81}C_{0.19}$ film decreases the corrosion current by four orders of magnitude to 8×10^{-10} A/cm^2. In addition, the $B_{0.24}C_{0.76}$ film presents a higher breakdown potential of 0.7 V compared with the $B_{0.81}C_{0.19}$ film, which implies the higher resistance to the initiation of localized corrosion, such as pitting.

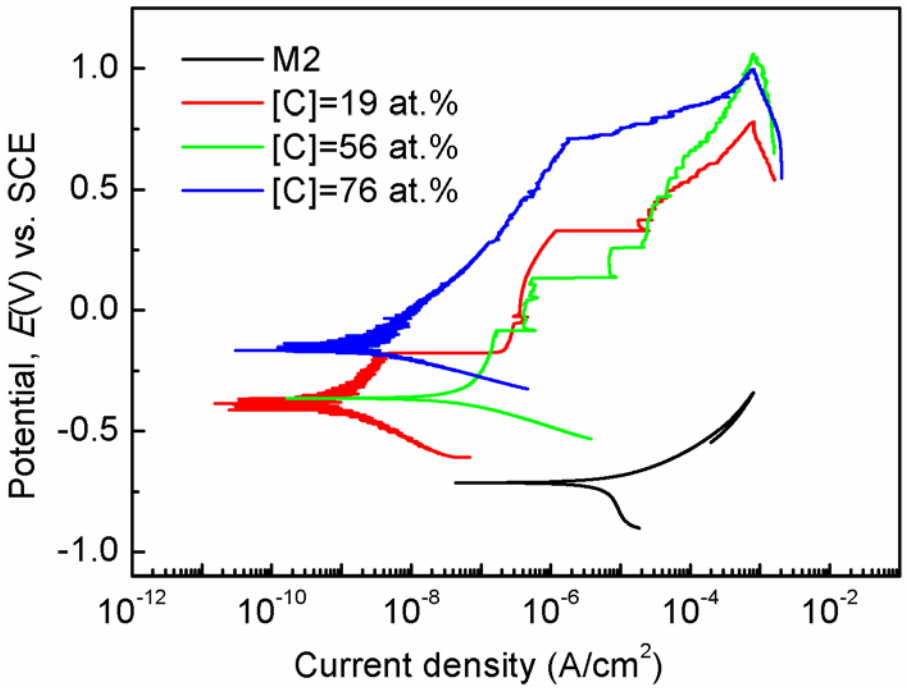

Figure 4.4 Potentiodynamic polarization curves of $B_{1-x}C_x$ films with different carbon contents.

4.3.4 Microstructure and composition

In order to explain the characteristics of the $B_{1-x}C_x$ materials from regions A, B and C (Figure 4.2 (b)), we performed a detailed microstructural and chemical analysis using XRD, Raman and XPS measurements. Figure 4.5 shows the XRD patterns for the $B_{0.81}C_{0.19}$, $B_{0.44}C_{0.56}$, and $B_{0.24}C_{0.76}$ films selected from the three regions indicated in Figure 4.2 (b). The patterns without any refined diffraction peaks imply the amorphous nature of the overall structure of the $B_{1-x}C_x$ films. The weak and broad diffraction peaks from the $B_{0.81}C_{0.19}$ and $B_{0.24}C_{0.76}$ films suggest formation of nanoparticles of boron carbide imbedded in the amorphous matrix. The diffraction peak at around 37.7° which corresponds to the diffraction from (021) crystallographic planes of boron carbide orthorhombic crystal structure [201] is observed in both the $B_{0.81}C_{0.19}$ and $B_{0.24}C_{0.76}$ films possessing the highest hardness in the A and C regions, respectively. On the other hand, no diffraction peaks are observed in the XRD spectra of $B_{0.44}C_{0.56}$ films exhibiting the lowest hardness (region B). The size of crystallites in the $B_{0.24}C_{0.76}$ film is smaller than that in the $B_{0.81}C_{0.19}$ film as indicated by the broader diffraction peaks. Such small crystallite size can be related to the relatively low boron content for the former film, while the main (021) diffraction peak shifts to higher angles by about 0.2° due to the built-in stress.

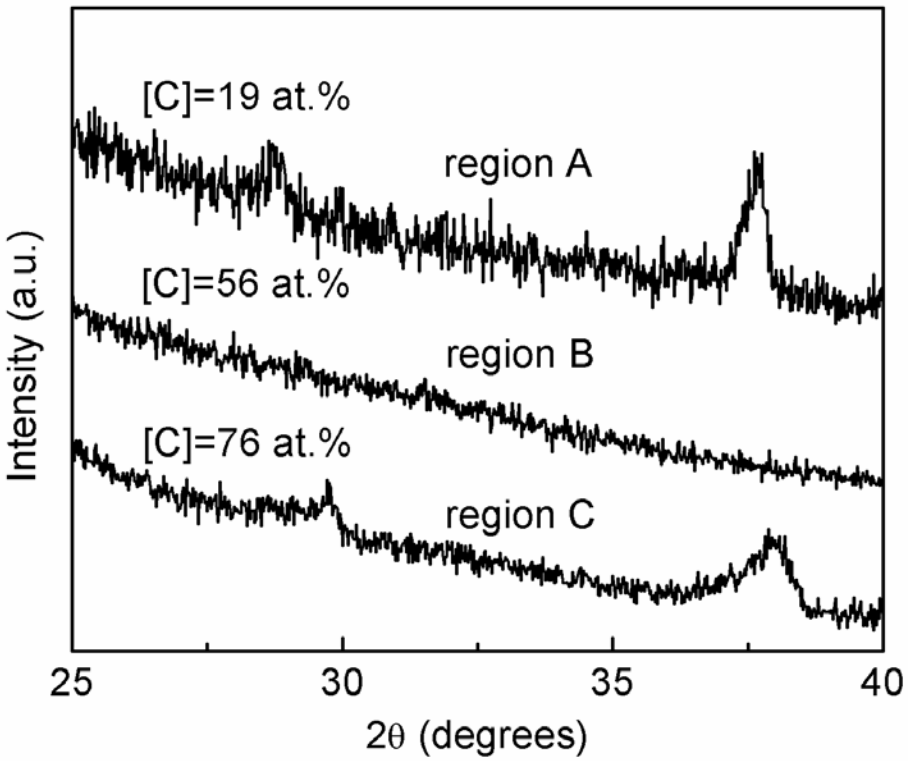

Figure 4.5 XRD spectra of the $B_{1-x}C_x$ films with different carbon contents.

Small diffraction peaks at 28.8° and 29.7° are observed in the XRD spectra of $B_{0.81}C_{0.19}$ and $B_{0.24}C_{0.76}$ films, respectively. Referring to the XRD data for bulk boron carbide, weak diffraction peaks are generally observed between 28° and 30°, and their positions vary with composition [202]. Therefore, the small diffraction peaks from $B_{0.81}C_{0.19}$ and $B_{0.24}C_{0.76}$ films may be attributed to boron carbide, but it is difficult to identify their specific phases due to a weak diffraction caused by the amorphous nature of the films and small crystallite size.

In complement to the XRD analysis sensitive to crystallinity, Raman spectroscopy provides information related to the bonding structure. This technique has been frequently applied for the analysis of carbon and carbon-based materials [203, 204]. Figure 4.6 shows Raman spectra of $B_{1-x}C_x$ films with different carbon contents. The $B_{0.81}C_{0.19}$ film (region A, high H = 28 GPa) exhibits a broad peak complex between 600 and 1200 cm^{-1} that can be assigned to the icosahedral mode of boron carbide [133]. In general, no specific peaks are observed in the Raman spectra of boron carbide single crystal at frequencies ranging from 600 to 1200 cm^{-1} because of the distribution of carbon atoms among the icosahedral sites, which introduces a form of substitutional disorder [133].

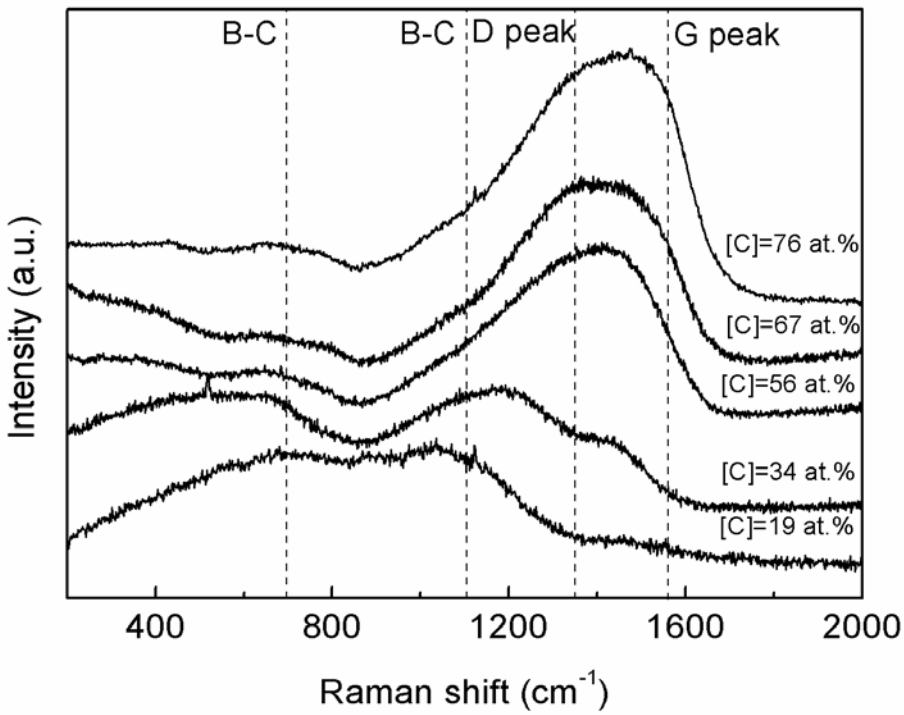

Figure 4.6 Raman spectra of the $B_{1-x}C_x$ films with different carbon contents.

As the carbon concentration in the $B_{1-x}C_x$ films increases, a broad band between 1000 and 1600 cm^{-1} arises. This intensity enhancement can be explained by the presence of amorphous carbon, for which the G peak around 1580−1600 cm^{-1} and the D peak around 1350 cm^{-1} [205] are characteristic of a mixture of graphitic and disordered sp^3-bonded carbon [204, 206]. Therefore, as the carbon content is increased, the structure can be considered as a mixture of amorphous carbon and boron carbide, as consistently indicated by the XPS analysis.

High resolution XPS core level spectra represented by the B 1s and C 1s peaks were collected to study the impact of carbon content on the chemical states of the $B_{1-x}C_x$ films. Figure 4.7 shows typical B 1s and C 1s high resolution spectra of the boron-rich $B_{0.81}C_{0.19}$ and the carbon-rich $B_{0.24}C_{0.76}$ films. The deconvoluted B 1s spectrum of the $B_{0.81}C_{0.19}$ sample in Figure 4.7 (a) features the presence of two chemical states indicated by the peaks at 188.3 eV and 189.4 eV, which are attributed to the B−C bonds in a B_4C environment (boron-rich), and to the B−C bonds with C atoms in a graphitic state (carbon-rich), respectively [142, 207]. An additional peak at 191.7 eV originating from B−O bonds [208] is observed in the B 1s spectrum of the $B_{0.24}C_{0.76}$ film as shown in Figure 4.7 (b). The area under each specific deconvoluted peak corresponding to a particular chemical bond structure determines the bond content (see Table 1.1). Thus when [C]

is low the area of the peak centered at 188.3 eV is large which indicates that 78% of carbon participate in the B−C bonds in B_4C. This indicates the presence of the B_4C phase as the major component in such boron-rich films. This observation is consistent with the Raman and XRD results described above.

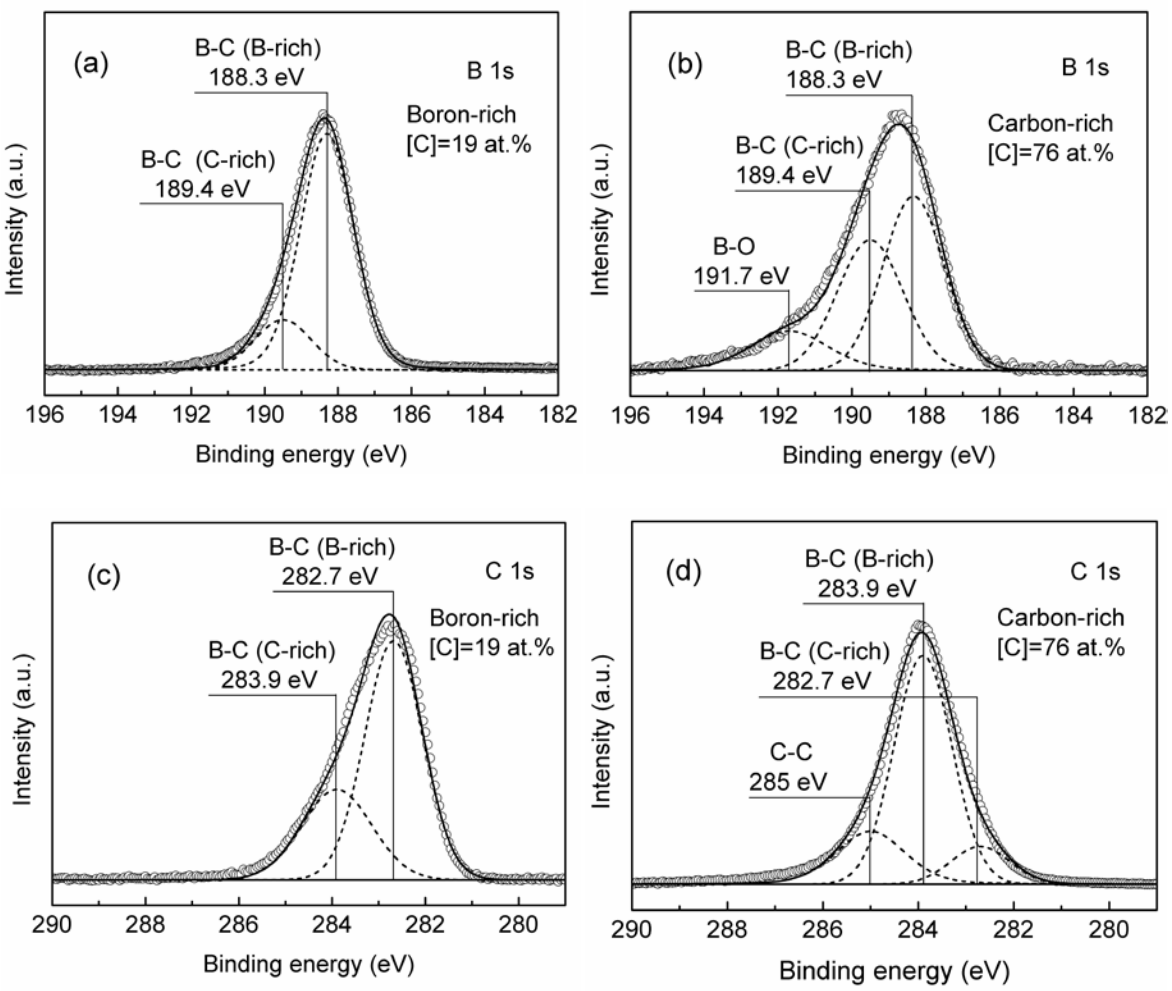

Figure 4.7 B1s and C1s core level spectra of the boron-rich $B_{0.81}C_{0.19}$ and the carbon-rich $B_{0.24}C_{0.76}$ films; experimental data (open circles), fitted results (solid lines) and their deconvoluted components (dashed lines).

Curve-fitted C 1s spectra of the selected $B_{0.81}C_{0.19}$ and $B_{0.24}C_{0.76}$ films are presented in Figure 4.7 (c) and (d). For the boron-rich $B_{0.81}C_{0.19}$ film, the peaks at 282.7 eV in the C 1s spectrum corresponds to C−B bonds within the B_4C environment, while a shoulder at 283.9 eV is assigned to B−C bonds in the carbon-rich environment [142, 209]. As the carbon content increases, the C 1s peak at 285 eV is significantly higher (as illustrated here for the $B_{0.24}C_{0.76}$ film)

indicating an abundant presence of the C−C bonds [143]. Combined with the peak area corresponding to chemical bonding given in Table 1.1, it is found that further addition of carbon results in an increase of the B−C bonds in the carbon rich-environment as well as in the formation of C−C bonds. This is consistent with the presence of amorphous carbon identified in the Raman spectra of the carbon-rich films.

Table 4.1 Peak areas corresponding to different chemical bonds in the boron-rich $B_{0.81}C_{0.19}$ and the carbon-rich $B_{0.24}C_{0.76}$ films.

		BE (eV)	Area (%)	
			$B_{0.81}C_{0.19}$ sample	$B_{0.24}C_{0.76}$ sample
B1s	B−C	188.3	82	47
		189.4	18	38
	B−O	191.7	0	15
C1s	C−B	282.7	69	11
		283.9	31	68
	C−C	285.0	0	21

4.4 General discussion

In this section, we discuss the mechanical properties of the $B_{1-x}C_x$ films in relation to the changes in the microstructure. In region A the $B_{0.81}C_{0.19}$ film possesses the highest hardness of 28 GPa. In this case the stoichiometry is very close to that of B_4C, and indeed, its X-ray diffraction patterns also indicated the formation of nanocrystalline boron carbide, leading to the high hardness of such film. In region B, no diffraction patterns are observed and the hardness of the $B_{1-x}C_x$ films is relatively low. In region C, formation of nanocrystalline boron carbide in the $B_{0.24}C_{0.76}$ film is inferred by XRD, while the presence of amorphous carbon (*a*-C) is deduced from the Raman spectra. This implies that the microstructure in region C can be described as a nanocomposite consisting of nanocrystalline boron carbide embedded in an amorphous boron carbide/*a*-C matrix. In this case, we may consider the hardening mechanism in nanocomposite films as described by Veprek [112]; films comprising nanoparticles imbedded in an amorphous matrix, (for example TiN in Si_3N_4) exhibit a high hardness which is enhanced by strengthening the nanoparticle-matrix interfaces [34, 102]. Therefore, the structure of nanocrystalline boron carbide in an amorphous boron carbide/*a*-C matrix also possibly gives rise to a high hardness for relatively low x in $B_{1-x}C_x$, specifically, for the $B_{0.24}C_{0.76}$ films (H = 25 GPa).

The tribological performance of the $B_{1-x}C_x$ films also varies with the composition and microstructure. The friction coefficient and wear rate decrease with the increasing carbon content, which can be related to a higher amount of amorphous carbon indicated by the Raman spectra for the carbon-rich $B_{1-x}C_x$ films. The amorphous carbon is the third structure which acts as a solid lubricant during the tribological test, and reduces the friction coefficient and wear rate. As shown, when the hardness is maintained over 25 GPa, the friction coefficient of the $B_{1-x}C_x$ films can be adjusted between a high value of 0.66 and a low value of 0.13 by changing the carbon content from 19 to 76 at.%. This feature makes the $B_{1-x}C_x$ films very promising to be applied in different areas, where hard coatings with either high or low friction coefficient are demanded.

4.5 Conclusions

$B_{1-x}C_x$ films with tailored carbon content were prepared by magnetron sputtering from element boron and graphite targets. Maximum hardness of 28 and 25 GPa was reached in both boron-rich and carbon-rich regions with [C] of 19 and 76 at.%, respectively. The mechanical properties are explained by the variation in the film microstructure. The structure of the $B_{1-x}C_x$ films has generally an amorphous character as deduced from XRD patterns. However, the broad and weak diffraction patterns from boron carbide observed for the films with maximum hardness imply the formation of nanocrystalline boron carbide. Based on the compositional and microstructural analysis by both XPS and Raman techniques, we demonstrate that a nearly stoichiometric B and C ratio like in the boron carbide (B_4C) and presence of a nanocrystalline structure yield the high hardness for boron-rich films. In addition, formation of a nanocomposite structure formed by boron carbide particles imbedded in the amorphous boron carbide/*a*-C matrix also enhances the high hardness of carbon-rich films.

The friction coefficient of the $B_{1-x}C_x$ films decreases from 0.66 to 0.13 by changing the carbon content from 19 to 76 at.% while the hardness over 25 GPa is maintained. The wear rate is correspondingly reduced by two orders of magnitude from 6.4×10^{-5} to 1.3×10^{-7} mm^3/Nm. The amorphous carbon component in the carbon-rich films acts as a solid lubricant layer, and it is responsible for the reduction of the friction coefficient and wear rate. The corrosion resistance of the M2 substrate is also significantly improved by applying the $B_{1-x}C_x$ films. Compared with the bare substrate, the corrosion current is reduced by four orders of magnitude to 8×10^{-10} A/cm^2 when a boron-rich film is used. In addition, $B_{0.24}C_{0.76}$ film gave a better performance with respect

to the breakdown potential of 0.7 V. In conclusion, the $B_{1-x}C_x$ films with high hardness, tunable tribological properties and high corrosion resistance are promising materials for protective coating in various industrial applications.

4.6 Acknowledgments

This work was supported by the Research Grants Council of the Hong Kong Special Administrative Region (Project No. CityU 104911), National Science Foundation of China (NSFC Grant 61176007 and 51372213), and the Natural Sciences and Engineering Research Council of Canada.

CHAPTER 5 ARTICLE 2: MICROSTRUCTURE AND TRIBO-MECHANICAL PROPERTIES OF TI−B−C NANOCOMPOSITE FILMS PREPARED BY MAGNETRON SPUTTERING

Article 2: Microstructure and tribo-mechanical properties of Ti−B−C nanocomposite films prepared by magnetron sputtering

Authors: J.C. Qian, Z.F. Zhou, W.J. Zhang, K.Y. Li, I. Bello, L. Martinu, and J.E. Klemberg-Sapieha

Article published: Surface and Coatings Technology, **270** (2015) 290.

Abstract

Ti−B−C nanocomposite films synthesized by magnetron sputtering are systematically studied with respect to the effect of composition and structure on their tribo-mechanical properties. The Ti−B−C films were deposited using a pilot-scale closed-field unbalanced magnetron sputtering system equipped with one graphite target, one TiB_2 target, and two boron targets. The microstructure of the Ti−B−C films is represented by TiB_2 nanocrystallites embedded in an amorphous boron carbide matrix. The film hardness varies in the range from 33 to 42 GPa in relation to the composition and microstructure. The change in the mechanical properties depends upon the nanostructure, particularly the concentration and size of the TiB_2 nanocrystallites in the amorphous boron carbide matrix. The tribological properties are closely related to the surface chemical states of the films. The lowest friction coefficient of 0.37 and the lowest wear rate of 3.3×10^{-6} mm^3/Nm are obtained for the Ti−B−C film with the highest titanium content, due to the formation of an oxide layer developed in the wear track. This layer acts as a solid lubricant during the tribological solicitation. The corrosion resistance of the M2 steel substrate is significantly enhanced by applying the Ti−B−C films, yielding a reduction of the corrosion current density by two orders of magnitude.

Key Words: Titanium boron carbide films, Superhardness, Nanocomposite, Magnetron sputtering, Tribo-mechanical properties, Corrosion resistance.

5.1 Introduction

Hard protective coatings have been widely used in industry to enhance the surface properties of various parts and components. Coatings with high hardness, good wear resistance, and high chemical inertness can improve the performance of aircraft and automotive engines, and of various instruments, such as mechanical movable parts of robots, prevent rapid failure of various tools, and generally avoid damage of the bulk materials [3-7]. Accordingly, development of novel hard protective coatings with improved surface tribo-mechanical properties and corrosion resistance leads to high economic impact in diverse fields, such as the automobile industry, space and aerospace, chemistry, energy conversation, electronic devices operating in harsh environments, and others.

Protective coatings based on binary, ternary, or quaternary nanocomposites are of great interest since their tribo-mechanical properties can be tailored by introducing different phases [11, 112, 210-212]. For example, the superhardness of nanostructured Ti−Si−N and Ti−B−N films can be induced by forming thermodynamically stable TiN or TiB_2 phases in an amorphous matrix [112, 212, 213]. The hardening is due to the strengthening of the interfaces between the two phases, preventing grain boundary sliding, avoiding dislocations in small grains [34], and hampering the accumulation of dislocations. Magnetron sputtering is widely used for deposition of nanocomposite coatings due to the relative ease of compositional control, low substrate temperature without harmful gases, and generally good film adhesion.

B-containing materials, such as B_4C and TiB_2, are well known for their excellent mechanical properties, high thermal stability, and chemical inertness [157, 214]. Therefore, Ti−B−C nanocomposite films appear very attractive due to the prospects of combining the properties of the two materials to form superhard protective coatings comprising hard ceramic phases (B_4C and TiB_2). Understanding of the hardening and tribological mechanisms is vital for the controlled synthesis of films with tailored properties. These mechanisms can be understood via studying the structural evolution and the effect of microstructure on the tribo-mechanical properties.

In the present work, Ti−B−C nanocomposite films were prepared by multi-target magnetron sputtering using one graphite target, one TiB_2 target, and two boron targets, as in our previous work on boron carbide ($B_{1-x}C_x$) films [215]. The power densities applied to the boron and

graphite targets were adjusted for obtaining B_4C films, while the TiB_2 phase content was controlled by the power density applied to the TiB_2 target. Very high hardness is reached due to the formation of a nanocrystalline TiB_2 phase in an amorphous B_4C matrix. Accordingly, the structural evolution and the variation of the tribo-mechanical properties of the Ti−B−C films were systematically investigated to explain the hardening and tribological mechanisms as well as the anti-corrosion performance.

5.2 Experimental methodology

5.2.1 Deposition of the Ti−B−C films

Ternary Ti−B−C films were deposited on Si (100) wafers and M2 high speed steel substrates using a pilot-scale closed-field unbalanced magnetron sputtering system (UPD 450, Teer Coatings Ltd.). The deposition chamber was composed of four vertical rectangular planar magnetrons with sizes of 330 mm by 133 mm, and a cylindrical substrate holder rack, 70 mm apart from the targets. The films were obtained by simultaneously sputtering one TiB_2 target, one graphite target, and two boron targets. The TiB_2 and graphite targets were powered from DC power supplies, and the two boron targets were powered from pulsed DC power supplies (350 kHz, 1 μs). The substrate holder rotated at 10 rpm to avoid formation of a layered structure and to provide a homogeneous compound. The total film thickness was 0.5 μm and 1 μm when deposited on Si and M2 steel substrates, respectively.

The substrates were ultrasonically cleaned in baths of detergent (Decon 90), ethanol, and deionized water before loading into the deposition chamber. A turbomolecular pump backed by a rotary pump was employed to evacuate the chamber, down to a background pressure lower than 1.0×10^{-4} Pa. Prior to deposition, the surface was sputter-cleaned for 30 min in Ar plasma at 250 kHz using a bias of −450 V. Subsequently, sputtering was carried out in Ar plasma at a pressure of $\sim2\times10^{-1}$ Pa with an Ar flow rate of 15 sccm. The power densities applied to the boron targets and to the graphite target were maintained at 2 and at 0.4 W/cm^2, respectively, while the TiB_2 target power density varied from 0.4 to 4.8 W/cm^2 to adjust the Ti content. The substrates were biased at −60 V during the deposition, and the substrate temperature was maintained at about 200 ^{o}C.

5.2.2 Structural characterization

Chemical and compositional analyses were performed by X-ray photoelectron spectroscopy (XPS) using a VG Escalab 220i-XL system equipped with a monochromatic Al Kα (1486.6 eV) X-ray source. Prior to collecting the high resolution XPS spectra, all samples were sputter-cleaned by an Ar ion beam with an energy of 3 keV at an angle of 30º to the sample normal to remove adventitious hydrocarbon, and carbon and oxygen based contaminants adsorbed on the film surface. Complementary Rutherford backscattering spectrometry (RBS) was employed to determine the elemental composition of the films. He^{++} ion beam with an energy of 2.7 MeV was applied, while backscattered ions were collected at the 170º detector geometry. The film crystallinity was assessed by analyzing the XRD patterns obtained using a Philips X'Pert X-ray diffractometer with Cu Kα X-rays at a grazing angle of 2º in a Bragg−Brentano configuration. A field emission scanning electron microscope (FESEM) (JEOL JSM7600F) was used to obtain the morphology of the film cross-sections.

5.2.3 Mechanical and tribological tests

The mechanical properties (hardness, H, and reduced Young's modulus, E_r) of the deposited Ti−B−C films on Si substrates were determined by depth-sensing indentation using a Triboindenter (Hysitron) system equipped with a Berkovich pyramidal tip. A maximum load of 5 mN was applied to the films, and the data were analyzed using the Oliver and Pharr method [190]. To diminish the substrate effect, the hardness was determined at an indentation depth less than 10% of the film thickness.

The tribological properties, namely, the friction coefficient, μ, and the wear rate, K, of the Ti−B−C films on M2 steel substrates were assessed by a conventional pin-on-disk wear test apparatus. A normal force of F = 2 N was applied to an alumina ball 6.35 mm in diameter being used as a counterpart material. The diameter of the wear track ring was 7 mm, while the linear speed was 30 mm/s. The worn volume, V, was measured by a profilometer after a sliding distance of s = 50 m. The resulting wear rate was calculated using the $K = V/(F \times s)$ formula. The wear tracks of the Ti−B−C films and the worn balls were first analyzed using a Nikon optical microscope. In addition, the surface morphology and elemental information of the wear track and

of the debris were assessed by a scanning electron microscope (SEM) (JEOL JSM840) equipped with an energy dispersive X-ray spectrometer (EDS).

5.2.4 Corrosion measurements

Corrosion properties of the Ti−B−C films prepared on M2 steel substrates were evaluated by a potentiodynamic polarization test using an Autolab PGSTAT302 potentiostat with a three-electrode cell described in more detail elsewhere [200]. The samples were exposed to the electrolyte (NaCl 1 wt.% solution) with a circular area of 10 mm in diameter (0.79 cm^2) at room temperature. The tested sample served as a working electrode, while a standard calomel electrode (SCE) and a graphite rod were used as reference and counter electrodes, respectively. The electrodes were first stabilized in the electrolyte for 1 h to reach a stable open circuit potential (OCP). Then the potentiodynamic polarization test was performed with a scan rate of 0.001 V/s. The potential was increasing from −0.2 V below the OCP, until the current density reached 1 mA/cm^2.

5.3 Results and discussion

5.3.1 Composition and microstructure

The composition of the Ti−B−C films was controlled by the power density applied to the TiB_2 target. Table 5.1 lists the composition of Ti−B−C films determined by both XPS and RBS, and the atomic concentrations as a function of the TiB_2 target power density are presented in Figure 5.1. The compositions obtained by these two techniques exhibit certain systematic differences, but the trends of individual elemental concentrations upon the sputtering power are consistent when the probing depth taken into account. The titanium content [Ti] rises when the TiB_2 target power density is increased as a result of the higher sputtering rate of TiB_2. The oxygen content [O] in the Ti−B−C films measured by RBS is lower than 2 at.%, and that measured by XPS increases from 4.5 to 10.4 at.% as [Ti] rises. In what follows, we refer to the Ti concentration obtained by RBS since this standardless analytical technique measures the atomic concentration across the depth of the film, whereas XPS has a shallow analysis depth, typically below 10 nm. Given the very similar trends between the RBS and XPS measurements, the Ti

contents of the samples which were not directly evaluated by RBS were estimated by linear interpolation with respect to the measured RBS results.

Table 5.1 XPS and RBS compositional analyses of Ti−B−C films deposited at different power densities applied to the TiB_2 target.

Sample no.	Power density applied to targets (W/cm^2)			Ti content (at.%)		B content (at.%)		C content (at.%)	
	TiB_2	B×2	C	XPS	RBS	XPS	RBS	XPS	RBS
B_4C	0	2.0×2	0.4	0	0	78.0	81.0	22.0	19.0
1	0.4	2.0×2	0.4	12.7	10.0	74.9	81.5	12.4	8.5
2	0.9	2.0×2	0.4	13.3	–	76.9	–	9.8	–
3	1.5	2.0×2	0.4	24.1	–	66.8	–	9.1	–
4	2.0	2.0×2	0.4	27.2	17.0	64.1	78.0	8.7	5.0
5	2.7	2.0×2	0.4	30.1	–	62.8	–	7.1	–
6	3.4	2.0×2	0.4	33.1	–	58.8	–	8.1	–
7	4.2	2.0×2	0.4	34.4	21.6	58.0	72.0	7.6	6.4
8	4.8	2.0×2	0.4	35.2	22.6	58.0	72.0	6.8	5.4
TiB_2	2.0	0	0	43.2	30.0	56.8	70.0	0	0

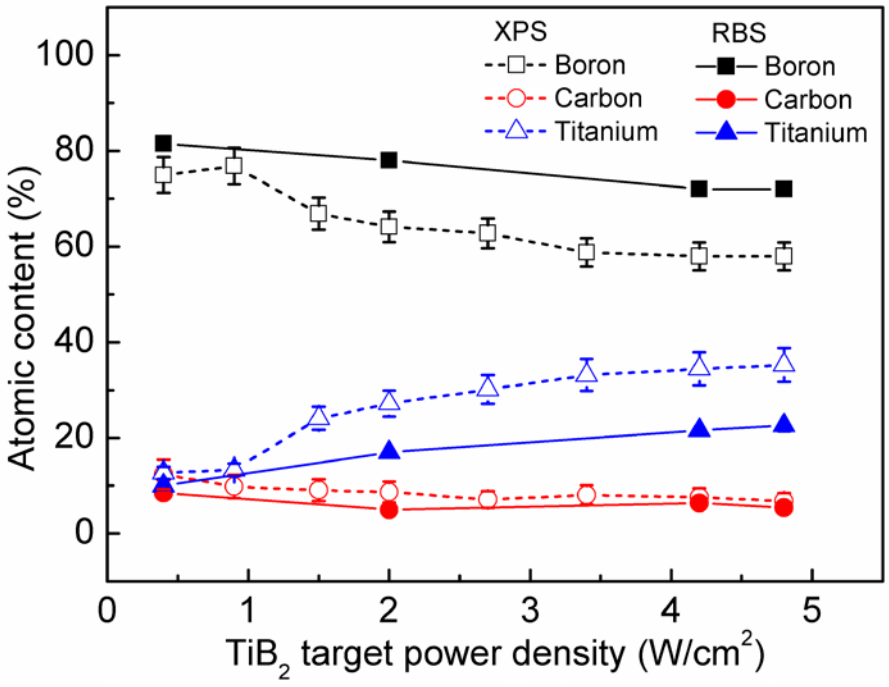

Figure 5.1 Variation of the film composition as a function of the power density applied to the TiB_2 target: open symbols−XPS results; full symbols−RBS results.

The microstructure of the Ti−B−C films was evaluated by XRD, and the patterns for films with varying [Ti] are presented in Figure 5.2 (a). The diffraction peaks are in agreement with a hexagonal TiB_2 phase [216] as indicated by the vertical dashed lines in the graph. The diffraction peaks from the Ti−B−C films slightly shift toward lower 2θ angles in comparison to the standard pattern, which may be related to a non-stoichiometry of the TiB_2 phase in the films. The small diffraction peaks at ~25º and ~53º are due to the boron carbide phase and the Si substrate, respectively. In summary, we can distinguish three regions of microstructure of the Ti−B−C films according to [Ti]: region A with [Ti] ≤ 15.0 at.% (Samples 1, 2, and 3); region B with 15.0 at.% < [Ti] < 20.0 at.% (Samples 4 and 5); and region C with [Ti] ≥ 20.0 at.% (Samples 6, 7, and 8).

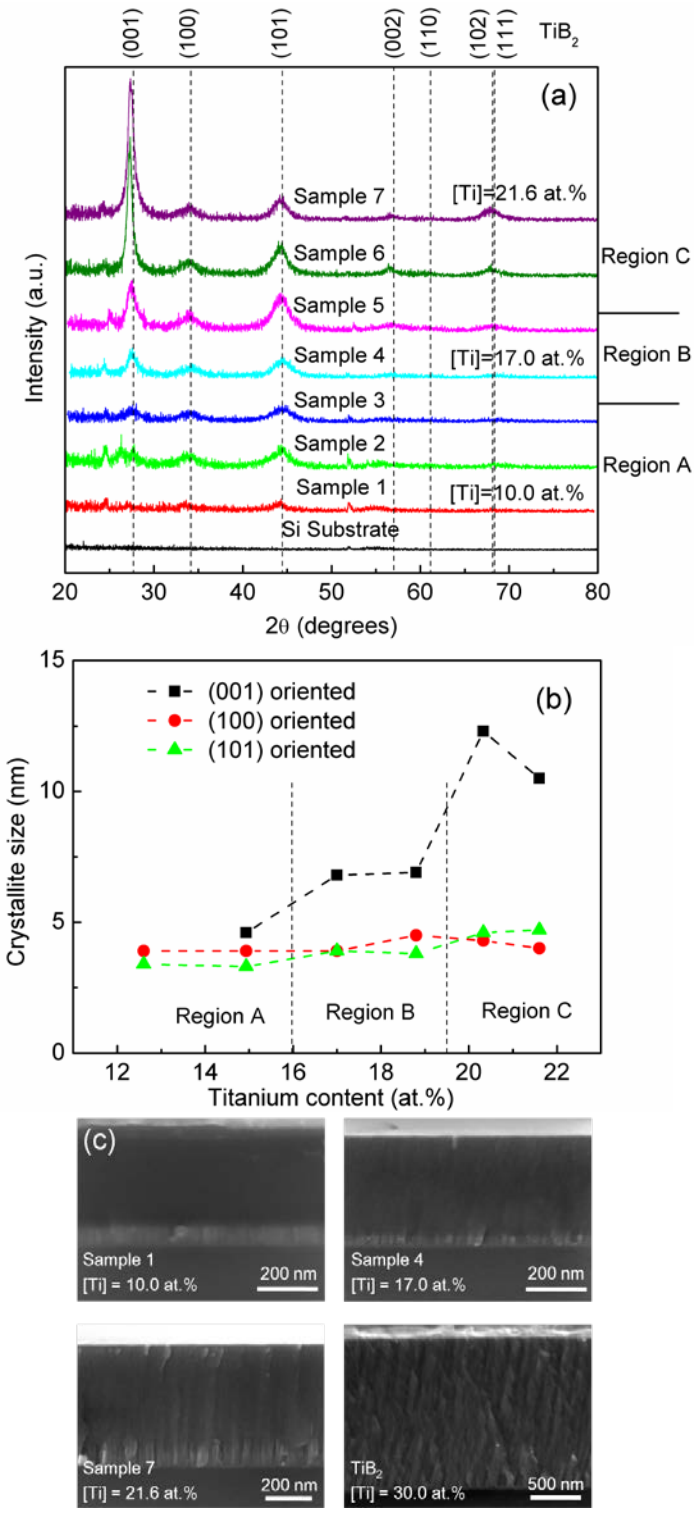

Figure 5.2 Microstructural characteristics of the Ti−B−C films: (a) XRD spectra of films with different titanium contents; (b) effect of Ti content on the crystallite size determined from XRD measurements; and (c) SEM cross-section images of representative Ti−B−C films (Samples 1, 4, and 7) and of the TiB_2 film.

In region A with low [Ti], the weak diffraction peaks imply an amorphous nature of the films and a reduced occurrence of the TiB_2 nanocrystals. The intensity of the TiB_2 diffraction patterns increases with higher [Ti] in region B, indicating a more abundant presence of the TiB_2 nanocrystallites. Further increase in [Ti] to region C leads to a slight increase of the (100) and (101) diffractions and a rapid increase of the preferred growth along the (001) orientation.

The crystallite sizes were estimated using the Scherrer equation (see Figure 5.2 (b)). Analysis of the (100) and (101) diffractions shows a minor increase in the crystallite size with the increase in [Ti]. The (101)-oriented crystallites grow from 3.4 to 4.7 nm as the [Ti] increases from 16.0 to 21.6 at.%, and the size of the (100)-oriented crystals is maintained at ~4 nm. In contrast, the crystallite size estimated from the (001) diffraction increases from 4.6 to 12.0 nm with rising [Ti]. This is consistent with a study on TiB_2 films which formed a nanocolumnar structure and a (001) preferred orientation [159].

The film microstructure as a function of [Ti] was also assessed using the SEM cross-section images of selected Ti−B−C films and of the TiB_2 film (Figure 5.2 (c)). Sample 1 with a low [Ti] of 10.0 at.% exhibits a textureless morphology, which is consistent with its amorphous nature as revealed by the XRD patterns. As [Ti] increases to 17.0 at.%, a weak texture is observed for Sample 4. A further increase of [Ti] to 21.6 at.% (Sample 7) leads to the occurrence of a nanocolumnar structure; this structural feature is more pronounced for the TiB_2 film with a highest [Ti] of 30.0 at.%. We therefore conclude that the structural evolution exhibiting a cross-sectional morphology as shown in the Figure 5.2 (c) is in agreement with the XRD analysis above.

In complement to the XRD and SEM analyses, the chemical bonding of the Ti−B−C films was evaluated by XPS. The high resolution XPS core level spectra of Sample 1 ([Ti] = 10.0 at.%), Sample 4 ([Ti] = 17.0 at.%), and Sample 8 ([Ti] = 22.6 at.%), selected from regions A, B, and C, respectively, are illustrated in Figure 5.3. Two chemical bonding states, namely Ti−B and Ti−O located at 454.6 and 455.7 eV, respectively [217, 218], are identified for the $Ti2p_{3/2}$ peaks as shown in Figure 5.3 (a). The $Ti2p_{3/2}$ peak positions for Samples 4 and 8 with higher [Ti] slightly shift to lower binding energy owing to the lower electron affinity of titanium, and the Ti−O bonds are caused by the surface oxidation.

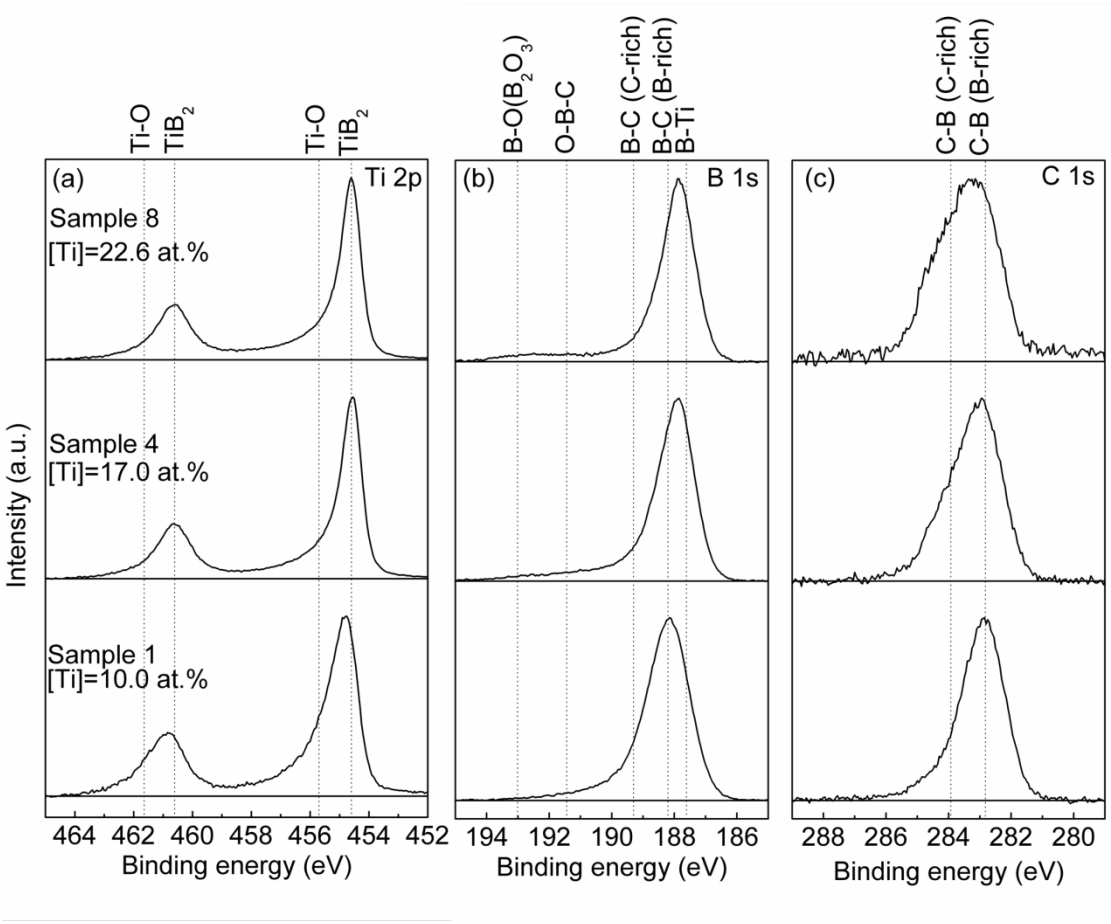

Figure 5.3 Ti2p, B1s, and C1s core level XPS spectra of representative Ti−B−C films (Samples 1, 4, and 8).

The primary peaks of the B1s XPS spectra as shown in Figure 5.3 (b) contain three chemical bonding states located at 187.6, 188.2, and 189.3 eV. The chemical state at 187.6 eV is assigned to the B−Ti bonds, and the other two chemical states at 188.2 and 189.3 eV are attributed to the B−C bonds in the B_4C state (boron-rich environment) and to the B−C bonds in the graphitic state (carbon-rich environment), respectively [142, 207]. The peak position shifts to lower binding energy at higher [Ti] indicating the increase of the TiB_2 phase. An additional complex peak at a higher binding energy (~193 eV) is observed in the B1s spectra of Sample 8 due to surface oxidation.

The C1s XPS spectra of Samples 1, 4, and 8 demonstrate the presence of two chemical states at 282.8 and 283.9 eV. Similar to the different binding energies of B−C bonds in different chemical environments in the B1s spectra, the observed three peaks are attributed to the C−B

bonds in a B_4C state (boron-rich environment) and the B−C bonds in a graphitic state (carbon-rich environment), respectively [142, 207].

5.3.2 Mechanical properties

The mechanical properties of the Ti−B−C films are presented in Figure 5.4 and interpreted with respect to the concentration regions A, B, and C introduced in Figure 5.2 and Figure 5.3. Typical load-displacement curves for Samples 1, 4, and 8, selected from regions A, B, and C, respectively, are compared in Figure 5.4 (a), from which the values of *H* and of the elastic recovery, *R*, are calculated. Sample 1, with the lowest [Ti] = 10.0 at.%, exhibits the lowest *H* and *R* values of 33 GPa and 78%, respectively. For Sample 4, with higher [Ti] = 17.0 at.%, the *H* value is increased to 38 GPa (by 15% higher than that of Sample 1), while the *R* value of 80% does not rise significantly. A further increase in [Ti] to 22.6 at.%, for Sample 8, gives rise to the highest *H* and *R* values of 42 GPa and 88%, respectively. Indeed, the Ti−B−C films with higher [Ti] exhibit better resistance to both plastic and elastic deformations, as indicated by the increase of the *H* and *R* values and the reduction of the maximum depth penetration.

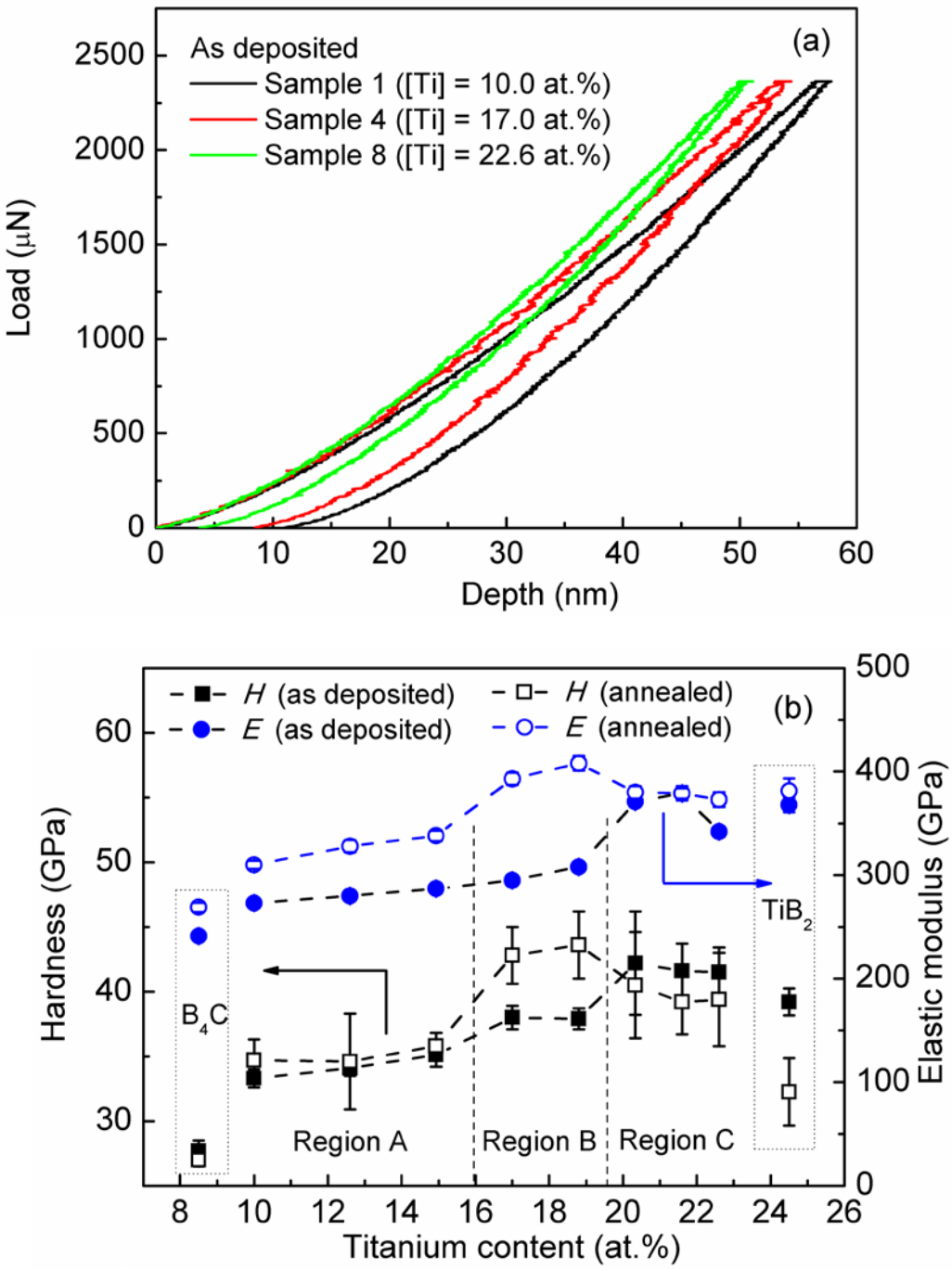

Figure 5.4 (a) Load-displacement curves for Samples 1, 4, and 8 selected from the concentration regions A, B, and C, respectively; (b) hardness and elastic modulus of the Ti−B−C films before and after annealing at 600 ºC as a function of titanium content.

The H and E_r values of the Ti−B−C films as a function of [Ti] are shown in Figure 5.4 (b). Specifically in comparison with H and E_r for the B_4C film (28 GPa, 241 GPa), the H and E_r

values of the as deposited Ti−B−C films gradually increase from 33 to 42 GPa and from 273 to 379 GPa, respectively, as the [Ti] increases from region A to region C. One can see that the *H* values in region C exceed that of both the B_4C and TiB_2 films.

In general, the hardening of thin films can be interpreted in terms of microstructure, which in turn, is closely related to the process conditions, such as ion bombardment. Defects can be induced by ion bombardment, and they are usually associated with the stress level in the films. The defects can hinder multiplication and movement of dislocations, and consequently, enhance the film hardness. In addition, the nanocomposite structure with an appropriate design can lead to hardness enhancement. The presence of strong interfaces between the nanocrystals and the amorphous matrix can increase the interface cohesive energy, and thus, prevent grain boundary sliding and formation of dislocations in small grains [34]. Their mechanical properties are closely related to the size and concentration of the nanocrystals.

For the Ti−B−C films in region A, the higher hardness compared to that of B_4C film can be attributed to the presence of small amounts of TiB_2 nanocrystals in the dense amorphous boron carbide matrix. The increase of *H* with higher [Ti] in region B is likely caused by the occurrence of a higher density and a larger size of TiB_2 nanocrystallites. In region C, *H* is further increased, and reaches a superhardness level ($H > 40$ GPa), a trend possibly related to the formation of TiB_2 nanocolumns within the amorphous matrix. We also note that *H* of the TiB_2 film is higher than that of the bulk TiB_2 (~25 GPa) [157]; the origin of this effect has been reported to be the presence of high compressive stress induced by ion-bombardment in the TiB_2 films [164] and formation of nanocolumnar structure for overstoichiometric TiB_x ($x > 2$) [159].

In order to better understand the hardening mechanisms of the B_4C, TiB_2, and Ti−B−C materials, all films were annealed in an Ar atmosphere at 600 ºC for 2 h with a ramping temperature rate of 10 ºC/min. Usually, post annealing at high temperature can relax the bombardment-induced compressive stress and lead to an increase of the grain size.

The *H* value of the B_4C film remains at ~28 GPa after annealing; in contrast, that of the TiB_2 film decreases from 39 to 32 GPa (see Figure 5.4 (b)); The hardness reduction can be attributed to the relaxation of the ion-induced stress during annealing [102]. The relaxation process and the differences in the expansion coefficients of the interfacing materials can even lead to film cracking, as observed in the case of the TiB_2 film after annealing. However, the *H* value of 32

GPa for the TiB_2 film is still higher than that of the bulk TiB_2. The overstoichiometry of the TiB_2 film (B/Ti = 2.3) (see Table 5.1) may be responsible for the relatively high hardness after annealing; in fact, *H* of overstoichiometric TiB_x with a nanocolumnar structure was reported to be fairly stable after post annealing [159].

For the Ti−B−C films in region A, the annealing process increases the *H* and E_r values by about 1 and 45 GPa, respectively. In comparison with the B_4C film with stable hardness after annealing, the films with low [Ti] exhibit a similar performance due to the high portion of boron carbide in the matrix. In contrast, the *H* and E_r values in region B are by about 5 and 100 GPa higher than those of the as deposited films, respectively. Obtaining superhardness (~43 GPa) after annealing can be related to TiB_2 grain growth, also reported for other nanocomposite films [25]. In region C, the *H* values decrease by about 2 GPa after annealing, while the E_r values do not vary significantly; this is similar to the effect of annealing of the TiB_2 film alone. This similarity is attributed to the high TiB_2 phase contents in the Ti−B−C films. In general, an increase of E_r upon annealing for films from all A, B, and C regions (even at different extends) may be attributed to the reduction of defects and of the grain boundary fraction [25, 219].

After annealing, the Ti−B−C films, the hardness dependence on [Ti] follows a typical relationship between the mechanical properties and the microstructure of nanocomposite films. The hardness increases with the TiB_2 nanocrystallite size at low [Ti] (region A), and the highest hardness is achieved when the nanocrystallite size reaches a critical value in region B. Further increase of the grain size in region C leads to a hardness reduction in agreement with the Hall-Petch relationship.

5.3.3 Tribological properties

The tribological properties of protective coatings are generally well represented by μ and *K*. Specifically, representative behavior of the films selected from regions A, B, and C is shown in Figure 5.5. The variation of μ as a function of sliding distance for Samples 1, 4, and 8 is illustrated in Figure 5.5 (a), while the average μ and *K* values are compared in Figure 5.5 (b). Samples 1 and 4 exhibit relatively high μ (0.56 and 0.73) and *K* values (4.7×10^{-5} and 5.7×10^{-5} mm^3/Nm), which are compatible with what has been observed for the “pure” B_4C [199] and TiB_2 [220]. Lower μ and *K* (0.37 and 3.3×10^{-6} mm^3/Nm) for Sample 8 may be explained by the presence of a different wear mechanism discussed below.

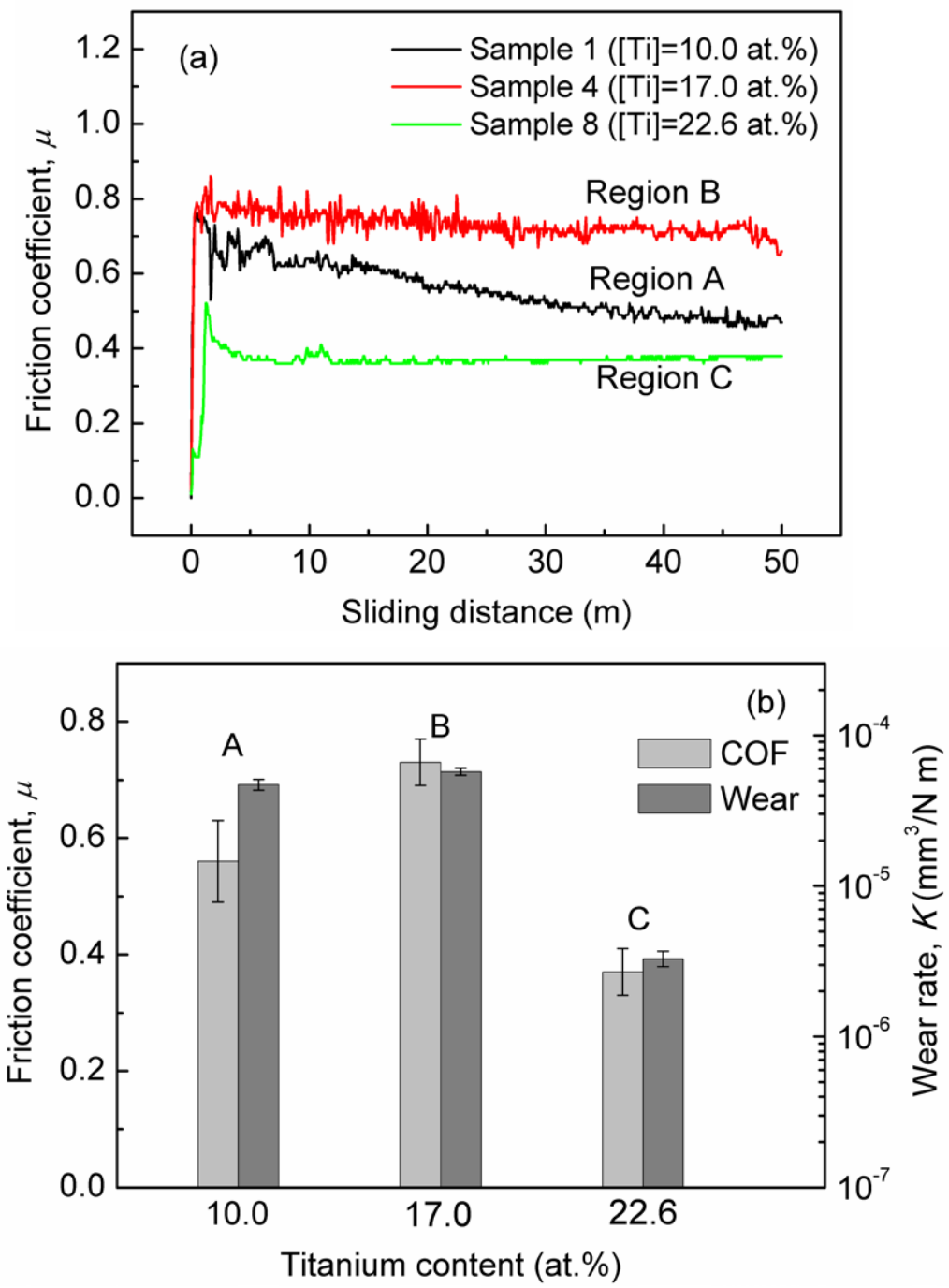

Figure 5.5 (a) Variation of the friction coefficient of the Ti−B−C films with different titanium contents as a function of sliding distance. (b) Friction coefficients and wear rates of the Ti−B−C films with different titanium contents. Counter body: alumina ball; load: 2N.

Wear mechanisms of the Ti−B−C films were studied by examining the wear tracks using optical microscopy, SEM, and EDS analyses; examples of the results are shown in Figure 5.6.

Optical images of the wear track for Sample 1 (region A) and of the corresponding counter body (see Figure 5.6 (a) and (b)) reveal that the originally spherical surface of the alumina ball is flattened. The corresponding SEM image of the wear track (Figure 5.6 (c)) clearly shows the wear debris. Analysis of the EDS spectra collected from the wear track (Figure 5.6 (d)) allows one to conclude that the composition of the bare wear track is consistent with that of the film, while the debris originates from the alumina ball as identified by the presence of O and Al. The wear behavior of Sample 4 (region B) as well as the measured results is very similar to that of Sample 1.

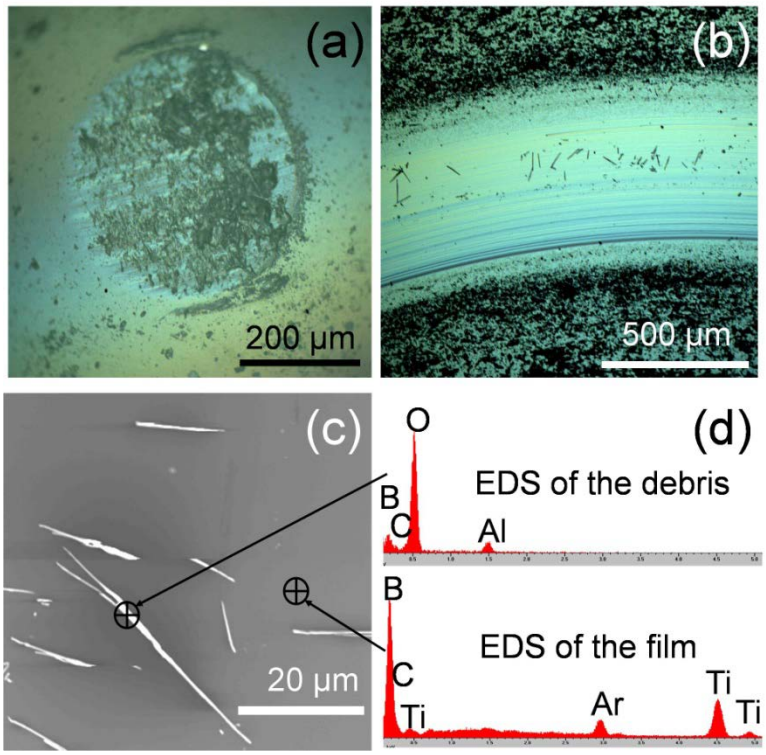

Figure 5.6 Optical microscope images of the worn ball (a) and of the wear track (b) for Sample 1 after the pin-on-disk test; (c) SEM images of the wear track on Sample 1; (d) EDS spectra of the wear track and of the debris on Sample 1.

The wear mechanism of Sample 8 (region C) appears to be different from that of Samples 1 and 4 as indicated by the results in Figure 5.7. The lower wear of the ball as well as of the sample surface is confirmed by the optical images in Figure 5.7 (a) and (b). In this case, one can observe layered debris attached to the wear track (SEM image in Figure 5.7 (c)). The EDS spectra (Figure 5.7 (d)) indicate that the debris is formed by an oxide, but the absence of aluminum excludes their

origin from the alumina ball. The oxide in the debris may be caused by both the original surface oxidation, as detected in the B1s and Ti2p XPS spectra, and oxidation induced during the wear process itself.

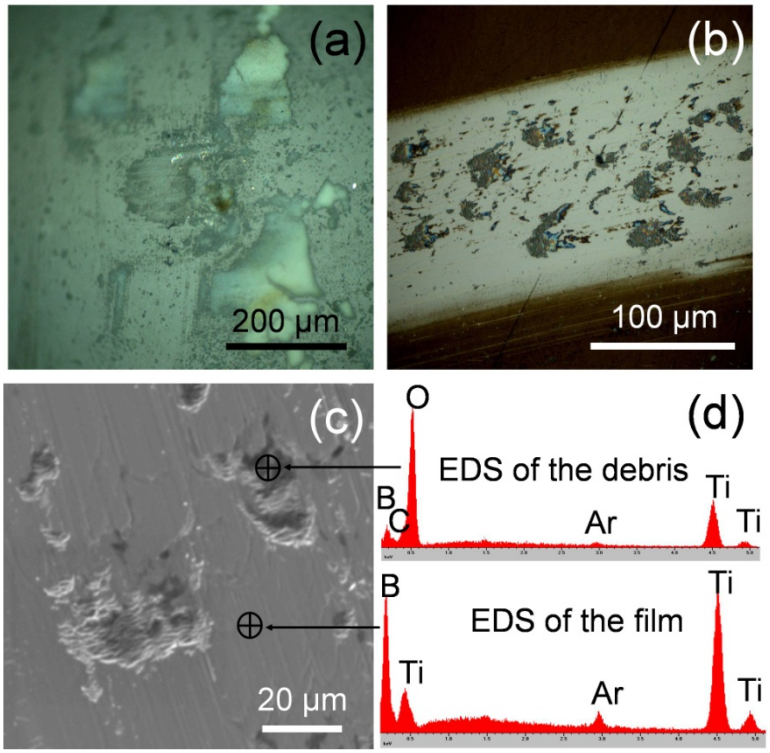

Figure 5.7 Optical microscope images of the worn ball (a) and of the wear track (b) for Sample 8 after the pin-on-disk test; (c) SEM images of the wear track on Sample 8; (d) EDS spectra of the wear track and the debris on Sample 8.

TiO_2 was demonstrated to possess μ of ~0.4 [221], and B_2O_3 can react with the moisture in humid air to form boron acid which exhibits μ lower than 0.1 [137]. Therefore, such oxides within the wear track of Sample 8 can function as a solid lubricant and decrease the friction and wear rate accordingly. In addition, the disparity of the wear behavior between Samples 1 and 8 can also be interpreted by their distinct mechanical properties as shown in Figure 5.4. Sample 8 possesses a higher resistance to plastic deformation compared to Sample 1, as indicated by the higher H and R values, as well as a lower penetration depth at the same load, which is a prerequisite to its lower wear rate.

5.3.4 Corrosion properties

Potentiodynamic polarization tests were performed to evaluate the corrosion behavior of the Ti−B−C films. The polarization curves of the coated and uncoated M2 steel substrates are shown in Figure 5.8. The corrosion resistance of all samples is assessed in terms of the corrosion current density, i_o. The corrosion resistance of the M2 steel is significantly enhanced by the presence of the Ti−B−C films as demonstrated by the reduction of i_o by two orders of magnitude from 3×10^{-6} to 1.1×10^{-8} A/cm^2. Moreover, the breakdown potential of all Ti−B−C films presented in Figure 5.8 is significantly higher than that of the bare M2 steel substrate; this also implies that the resistance to the initiation of localized corrosion, such as pitting, is improved by the Ti−B−C layer.

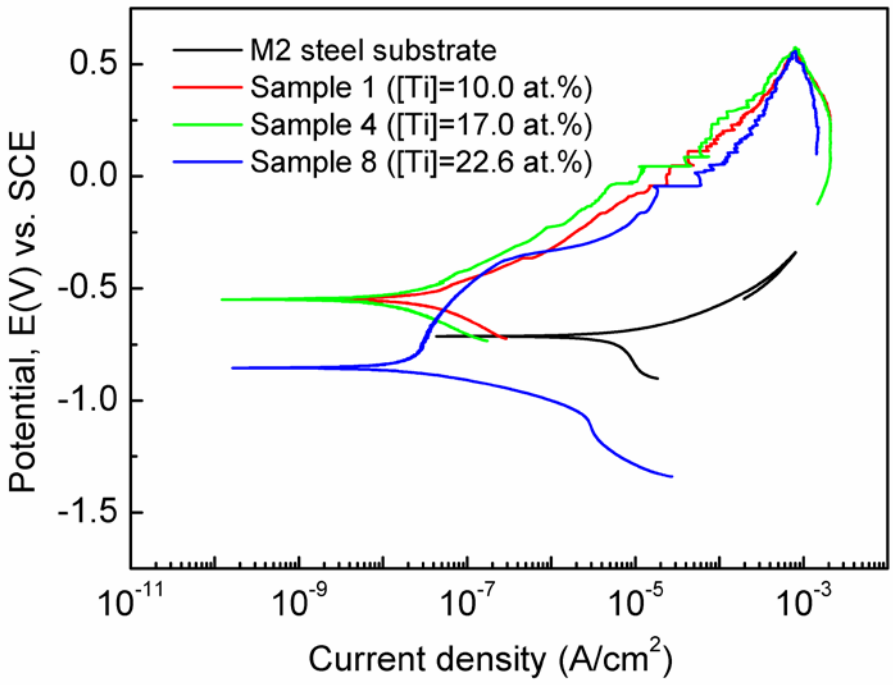

Figure 5.8 Potentiodynamic polarization curves of the Ti−B−C films with different titanium contents.

5.4 General discussion

Here we compare the tribo-mechanical properties of the present Ti−B−C nanocomposite coatings with those of other hard coatings, including the B-containing films studied in our previous work [168, 169]. Ranges of the H and μ values are summarized in Figure 5.9. H of the

B-containing coatings is generally higher than 20 GPa (Figure 5.9 (a)), clearly confirming their classification as hard coatings. Particularly, *c*-BN films exhibit superhardness due to their high atomic density and strong chemical bonds [48]. *H* of the $B_{1-x}C_x$, Al−Mg−B, and TiB_2 films is generally in the range of 20−30 GPa; however, nanocomposite B-containing coatings with appropriate microstructure can reach superhardness levels (> 40 GPa). This is indeed the case for the Ti−B−C films formed by TiB_2 nanocrystallites in the amorphous $B_{1-x}C_x$ studied here, or for the nanocomposite Al−Mg−B−Ti coatings with TiB_2 particles embedded in the Al−Mg−B matrix reported earlier [169].

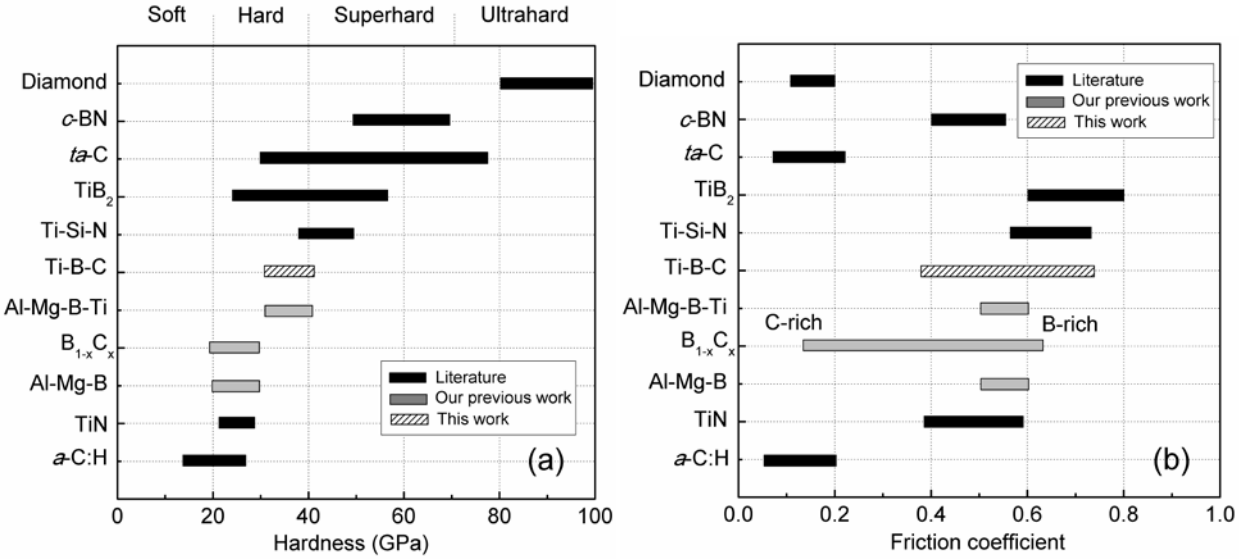

Figure 5.9 Mechanical and tribological properties for the most frequently studied hard protective coatings including our work on B-containing films: (a) hardness and (b) friction coefficient.

Figure 5.9 (b) compares the tribological properties of hard coatings in terms of the friction coefficient. The μ values of the B-containing coatings vary over a large range depending on their composition. For instance, μ of the $B_{1-x}C_x$ layers can be tuned from 0.13 to 0.76 by controlling the B/C ratio [215]. In such a case, the low friction is closely related to the formation of amorphous carbon, which acts as a solid lubricant during the tribological process. Surface chemical characteristics can strongly affect the tribological performance as well. For instance, the superhard Ti−B−C coating with high titanium content (such as Sample 8 from region C in this work) exhibits low friction due to the formation of a low-μ surface oxide layer acting as solid lubricant.

In addition to the tribo-mechanical properties, corrosion resistance also frequently represents a very important criterion for the selection of protective coatings. Both the $B_{1-x}C_x$ and Ti−B−C coatings can significantly improve corrosion resistance of the M2 steel substrate. The lowest i_o has been achieved for the $B_{1-x}C_x$ films ($i_o = 8\times10^{-10}$ A/cm^2) which is four orders of magnitude lower compared to the bare M2 steel. For comparison, the Ti−B−C nanocomposite coatings present a lower corrosion resistance indicated by a higher i_o of 1.1×10^{-8} A/cm^2. Such differences are related to the microstructures; specifically, the mainly amorphous nature of the $B_{1-x}C_x$ films gives rise to a high corrosion resistance.

5.5 Conclusions

In the present work, we studied the microstructural, tribo-mechanical, as well as corrosion properties of the Ti−B−C nanocomposite films synthesized by magnetron sputtering. The titanium content in the films, ranging from 10.0 to 22.6 at.%, was controlled by the power density applied to the TiB_2 target.

We interpreted and discussed the film behavior and performance with respect to three regions (A, B, and C) according to the titanium concentration: (i) in region A with [Ti] ≤ 15.0 at.%, the films exhibit *H* values of 33−35 GPa due to the formation of small amounts of TiB_2 nanocrystallites embedded in an amorphous boron carbide matrix. A typical friction coefficient of 0.56, which is comparable with that of boron carbide, is the consequence of the large portion of boron carbide in the matrix. (ii) In region B with 15.0 at.% < [Ti] < 20.0 at.%, the increase of both the quantity and size of TiB_2 nanocrystallites leads to higher *H* values of ~38 GPa and a friction coefficient of ~0.73 close to that of TiB_2. (iii) In region C with [Ti] ≥ 20.0 at.%, the highest hardness of ~42 GPa is achieved as a result of a larger amount and a larger size of TiB_2 nanocrystallites with a (001) preferred orientation and the ion-induced stress. The friction coefficient is reduced to 0.37 owing to the oxide layer formed within the wear track acting as a solid lubricant. Coating M2 steel substrates with Ti−B−C films was found to lead to a higher corrosion resistance documented by a decrease of the corrosion current density from 3×10^{-6} to 1.1×10^{-8} A/cm^2.

In summary, the tribo-mechanical properties of Ti−B−C films can be adjusted by controlling the composition and the microstructure. In comparison with other boron-containing films and

different complementary hard protective coatings, we present “tribo-mechanical” maps in terms of the hardness and friction coefficient. This allows one to perform an appropriate selection of materials with respect to the specific tribological application and the corresponding performance requirements.

5.6 Acknowledgments

This work was supported by the Natural Sciences and Engineering Research Council of Canada through its Industrial Research Chair Program, the Research Grants Council of the Hong Kong Special Administrative Region (Project No. CityU 104911), and the National Science Foundation of China (NSFC Grant 61176007 and 51372213).

CHAPTER 6 ARTICLE 3: HIGH QUALITY BORON CARBON NITRIDE/ZNO-NANORODS P-N HETEROJUNCTIONS BASED ON MAGNETRON SPUTTERED BORON CARBON NITRIDE FILMS

Article 3: High quality boron carbon nitride/ZnO-nanorods p-n heterojunctions based on magnetron sputtered boron carbon nitride films

Authors: J. C. Qian, S.K. Jha, B. Q. Wang, E. V. Jelenković, I. Bello, J. E. Klemberg-Sapieha, L. Martinu and W. J. Zhang*

Article published: Applied Physics Letters, **105** (2014) 192104.

Abstract

Boron carbon nitride (BCN) films were synthesized on Si (100) and fused silica substrates by radio-frequency magnetron sputtering from a B_4C target in an Ar/N_2 gas mixture. The BCN films were amorphous, and they exhibited an optical band gap of ~1.0 eV and p-type conductivity. The BCN films were overcoated with ZnO nanorod arrays using hydrothermal synthesis to form BCN/ZnO-nanorods p-n heterojunctions, exhibiting a rectification ratio of 1500 at bias voltages of ±5 V.

6.1 Introduction

Boron carbon nitride (BCN) is an attractive material due to its structural similarity to carbon (graphite and diamond) and boron nitride (BN in hexagonal and cubic phases). The hexagonal BCN (*h*-BCN) has tunable electrical characteristics that fall between semi-metallic graphite and insulating hexagonal BN (*h*-BN) [177], while the cubic BCN (*c*-BCN) shows properties comparable to diamond and cubic BN (*c*-BN) [172]. BCN films have been synthesized by a variety of techniques including chemical vapor deposition (CVD) [222-224] and physical vapor deposition (PVD) [225, 226]. In contrast to the C and BN phase segregation commonly observed in *c*-BCN films [178, 179]. the synthesis of the ternary *h*-BCN phase is available as confirmed by X-ray absorption near-edge spectroscopy (XANES) [180]. Preliminary studies suggest that *h*-BCN is a p-type semiconductor with a band gap strongly dependent on the elemental composition [181-183]. Interestingly, amorphous BCN films were synthesized at lower substrate temperatures while their tunable electrical properties could still be maintained [117]. The low deposition

temperature reduces the manufacturing cost, and makes it possible to carry out the deposition on substrates with low melting points, such as flexible plastics [227]. Thus far, there have been only very few studies on the electronic devices based on BCN to a large extent due to the complex phase structure varying with the deposition parameters and the film composition.

Very interesting device applications of BCN have been predicted, and several related patents have been granted [228]. In particular, boron-containing materials are well known as good candidates for applications in solid state neutron detection because of the high neutron capture cross section of boron [153]. Various p-n junction neutron detectors based on semiconducting boron carbide (BC) have been fabricated, such as homojunctions made by doping [156]. heterojunctions formed with other materials [154, 155], and "heteroisomeric" junctions composed of undoped p- and n-type BC [229]. Combining the high neutron capture ability and unique semiconducting properties, BCN can potentially be the material of choice for fabricating neutron detection devices. Therefore, p-n junctions based on BCN are very important to investigate for practical applications.

ZnO, as an inherent n-type semiconductor [230], is a very attractive material to form p-n heterojunctions with p-type BCN. As inspiration, ZnO nanorods (NRs) have been used as building blocks in active electronic and optoelectronic devices, such as transistors, light emitting diodes [231, 232], and solar cells [233, 234]. In response, in this work we present a heterojunction diode made of BCN/ZnO-NRs using simple growth of ZnO NRs on BCN films. We show a representative *I-V* characteristic of the BCN/ZnO-NRs heterojunctions, and demonstrate a rectification ratio of 1500.

6.2 Experimental methodology

BCN films were prepared by RF (13.56 MHz) magnetron sputtering from a single B_4C target (75 mm in diameter). The films, with a thickness of ~1 μm, were deposited on Si (100) and fused silica substrates. Prior to deposition the system was pumped down to a base pressure of $< 1.0\times10^{-4}$ Pa, and the sputtering process was carried out using a gas mixture of N_2:Ar with a flow rate ratio of 2:8 and a total flow rate of 10 sccm at a pressure of 0.4 Pa. RF power of 200 W was applied to the B_4C target, and the substrate holder was electrically grounded. The substrates were not intentionally heated, and the substrate temperature reached about 90 °C due to plasma heating.

In the subsequent step, arrays of vertical ZnO NRs were grown over the BCN film using a low-temperature (95ºC) hydrothermal growth process [235, 236]. Thus, both the BCN and ZnO materials were processed at temperatures below 100ºC and hence required little thermal budget.

The structure of the BCN films was studied by Fourier transform infrared spectroscopy (FTIR) (FT-IR 1600, Perkin-Elmer). The elemental composition and the chemical structure of the films deposited on silicon were analyzed by X-ray photoelectron spectroscopy (XPS) using a VG ESCALAB 220i-XL ultrahigh vacuum (UHV) surface analytical facility with a base pressure of 10^{-7} Pa. A monochromatic Al Kα (1486.6 eV) X-ray source was used, and the XPS spectra were taken after Ar ion sputter cleaning of the sample surface. A Lambda-750 UV/Vis spectrophotometer was used to record absorption spectra and analyze optical properties of the BCN films on fused silica. The Hall measurements were carried out at 5,000 G and room temperature using a Lakeshore 7704A system. The morphology of the ZnO NRs was studied by scanning electron microscopy (SEM, Philips FEG SEM XL30). The electrical characterization of the BCN/ZnO-NRs heterojunction diodes was performed using a Keithley-4200 semiconductor parameter analyzer.

6.3 Results and discussion

A representative FTIR spectrum of the as-deposited BCN films is presented in Figure 6.1. Two distinct absorption bands can be observed. The narrow band located at 780 cm^{-1} is assigned to the out-of-plane B−N−B bending vibration, whereas the broad band centered around 1400 cm^{-1} can be attributed to the in-plane B−N stretching vibration [48]. However, this broad band extended over a wide wavenumber range from 1000 to 1800 cm^{-1}; no well-defined peaks could be observed mainly due to the highly disordered structure of the BCN films and the multiple bonding arrangements as revealed by XPS analysis below. In fact, several bond types involving boron, carbon, and nitrogen can appear in this wavenumber range, e.g., cubic BN phase at 1070 cm^{-1}, B−C stretching vibration from 1090 to 1250 cm^{-1} depending on the chemical environment [237], and C−N (sp) and C=N (sp^2) bonds at 1272 and 1540 cm^{-1}, respectively. Overlapping of these individual bands and short range order of structural crystallinity prevent resolving these chemical states in the FTIR spectra.

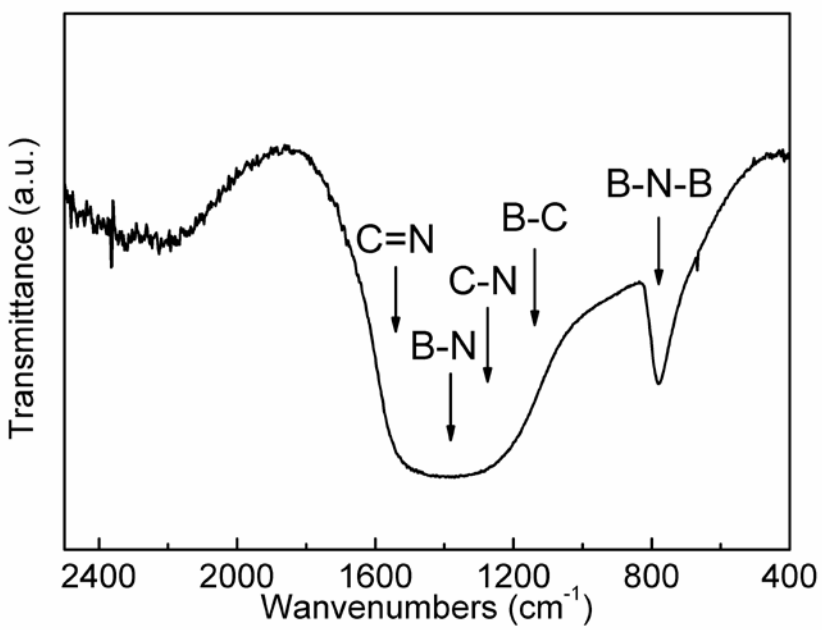

Figure 6.1 Representative FTIR spectrum collected from a pristine BCN film.

In complement to the FTIR measurements, XPS analysis was carried out to study the atomic composition and chemical states. Figure 6.2 presents high resolution XPS B1s, N1s, and C1s core level spectra of the BCN films after Ar ion sputter cleaning. By calculating the integrated areas of the corresponding peaks corrected for sensitivity, the atomic concentrations of boron, carbon, nitrogen, and oxygen (denoted [B], [C], [N], and [O], respectively) before sputter cleaning were 30.0, 24.3, 30.6, and 15.1 at.%, respectively. After Ar ion sputter cleaning, [C] and [O] decreased to 11.1 and 5.7 at.%, whereas the portions of [B] and [N] increased to 44.5 and 38.7 at.%, respectively. This indicates that the adventitious hydrocarbon and oxygen-based contaminants adsorbed on the surface were removed.

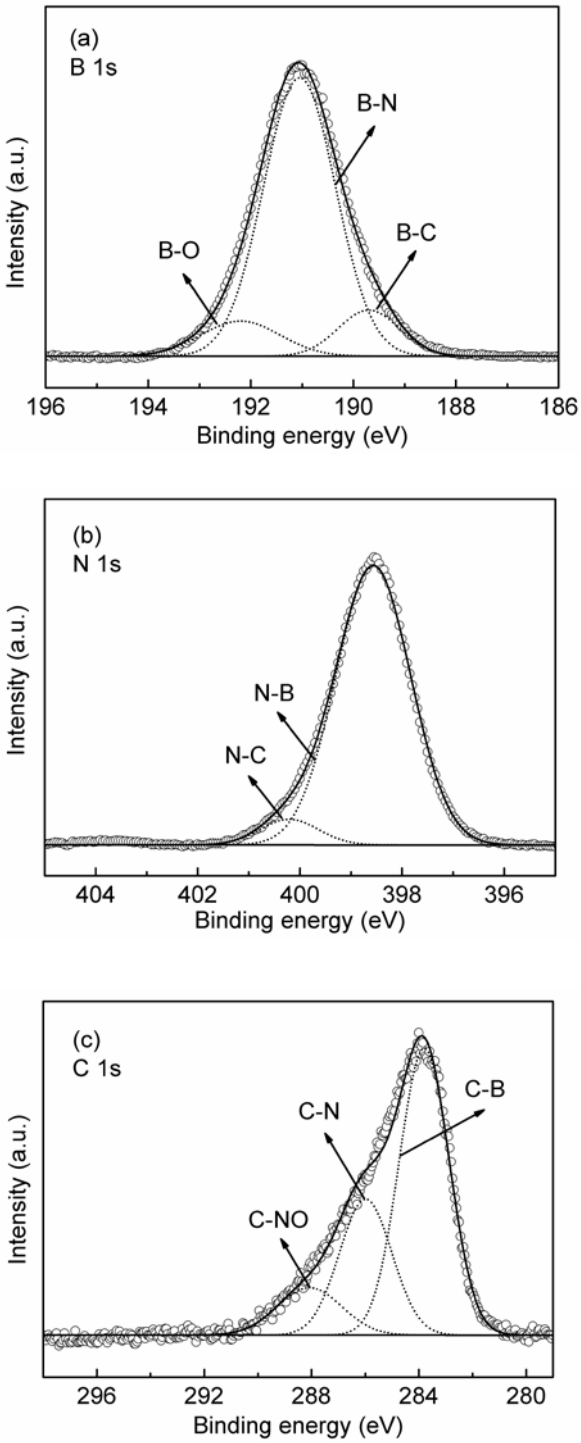

Figure 6.2 High resolution XPS spectra obtained from a pristine BCN film: (a) B1s, (b) N1s, and (c) C1s core level spectra. The open circles are the raw data; the solid lines are backgrounds and fitted curves, while the dash lines are deconvoluted peaks corresponding to different chemical states.

The broad and asymmetric peaks of B1s, N1s, and C1s imply the existence of multiple chemical environments in the BCN matrix. The B1s spectrum in Figure 6.2 (a) could be deconvoluted into three peaks located at 189.6, 191.0, and 192.2 eV. The dominant component centered at 191.0 eV is assigned to B−N bonds. The smaller shoulders peaking at 189.6 and 192.2 eV are attributed to B−C and B−O bonds, respectively [238]. In the N1s spectrum (Figure 6.2 (b)) the major component at 398.5 eV originates from N−B bonding, consistent with the corresponding chemical state in the B1s spectrum. The component located at 400.2 eV suggests formation of sp^2 N−C bonds [239, 240].

Since the percentage of each chemical state is proportional to the integral area of the resulting deconvoluted peak, it is found that the abundance of B−N bonds is much higher than that of B−C bonds. Deconvolution of the C1s peak in Figure 6.2 (c) reveals the C−B bonding at 283.6 eV, the sp^2 C−N bonding at 286 eV, and the C−NO bonding at 288.1 eV. The presence of B−O and C−NO bonds is due to residual surface oxides which are more resistant to the sputter cleaning process than the physically adsorbed surface contaminants. Both the FTIR and XPS analyses imply that the ternary BCN films are amorphous and composed of B−N, C−N, and B−C bonds.

Hall measurements showed that the BCN films exhibit p-type conductivity and a carrier mobility of 1−5 cm^2/Vs at room temperature. In comparison, the carrier mobility of polycrystalline BCN films deposited by CVD at a substrate temperature of ~850 ºC was reported to be in the range of 0.37–30 cm^2/Vs depending on the film microstructure [183, 241]. The low carrier mobility of the BCN films in this work is due to their amorphous nature and it needs to be further improved for their electronic applications.

The optical properties of the BCN films were studied by UV/Vis spectroscopy. A representative UV-Vis absorption spectrum of the BCN films deposited on fused silica substrates is shown in Figure 6.3. The films exhibit a fairly broad absorption band ranging from the visible to the near-infrared region. The interference fringes observed at the absorption edge are due to the multiple reflections in films. In the inset of Figure 6.3, $(\alpha h\nu)^{1/2}$ is plotted as a function of photon energy ($h\nu$), where α is the absorption coefficient. From this function, known as the Tauc's plot, the optical band gap of the BCNs films is determined by an extrapolation method. The tangent intersect with the abscissa points to an optical band gap of 1.0 eV.

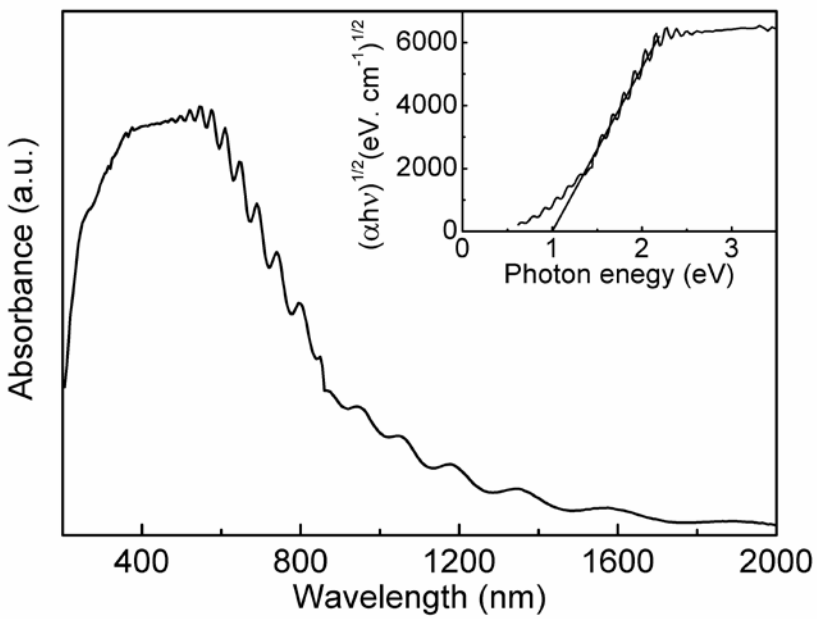

Figure 6.3 UV-Vis absorption spectrum of a typical BCN film. The inset shows $(\alpha hv)^{1/2}$ plotted as a function of photon energy.

Thus, the Hall measurements and UV-Vis absorption analysis indicate that the BCN films are p-type semiconductor with a band gap of 1.0 eV. BCN is a complex ternary composite with electronic and electrical properties strongly influenced by the composition and phase structure which are strongly related to the deposition method and the deposition conditions. Early studies on BCN films reported a band gap of ~3.0 eV when the films were synthesized by CVD at temperatures higher than 300 ºC [181]. Elsewhere [117] it was shown that the optical band gap of the BCN deposited by sputtering decreased from 2.0 to 1.5 eV as the deposition temperature decreased from 550 to 250 ºC. In the presented work, the substrate temperature is below 100ºC that appears to result in a relatively narrow band gap of 1.0 eV.

To facilitate p-n heterojunctions, ZnO NR arrays were grown on the BCN films by a low-temperature hydrothermal growth method. The cross-sectional SEM images in Figure 6.4 (a) show that the ZnO NRs are tightly bonded with the BCN films through a ZnO seeding layer, and no delamination between ZnO and BCN films was observed. ZnO NRs are grown uniformly over the BCN film with a typical length of 3 μm and a diameter of ~200 nm in average; the density of the NRs is approximately 4.58×10^{8} cm^{-2}, and the NRs preferentially grow along the direction orthogonal to the substrate (i.e. along the *c*-axis of the ZnO lattice). Because of the inherent n-

type conductivity of the ZnO NRs, p-n heterojunctions are formed between the BCN film and the ZnO NRs on the silicon substrate.

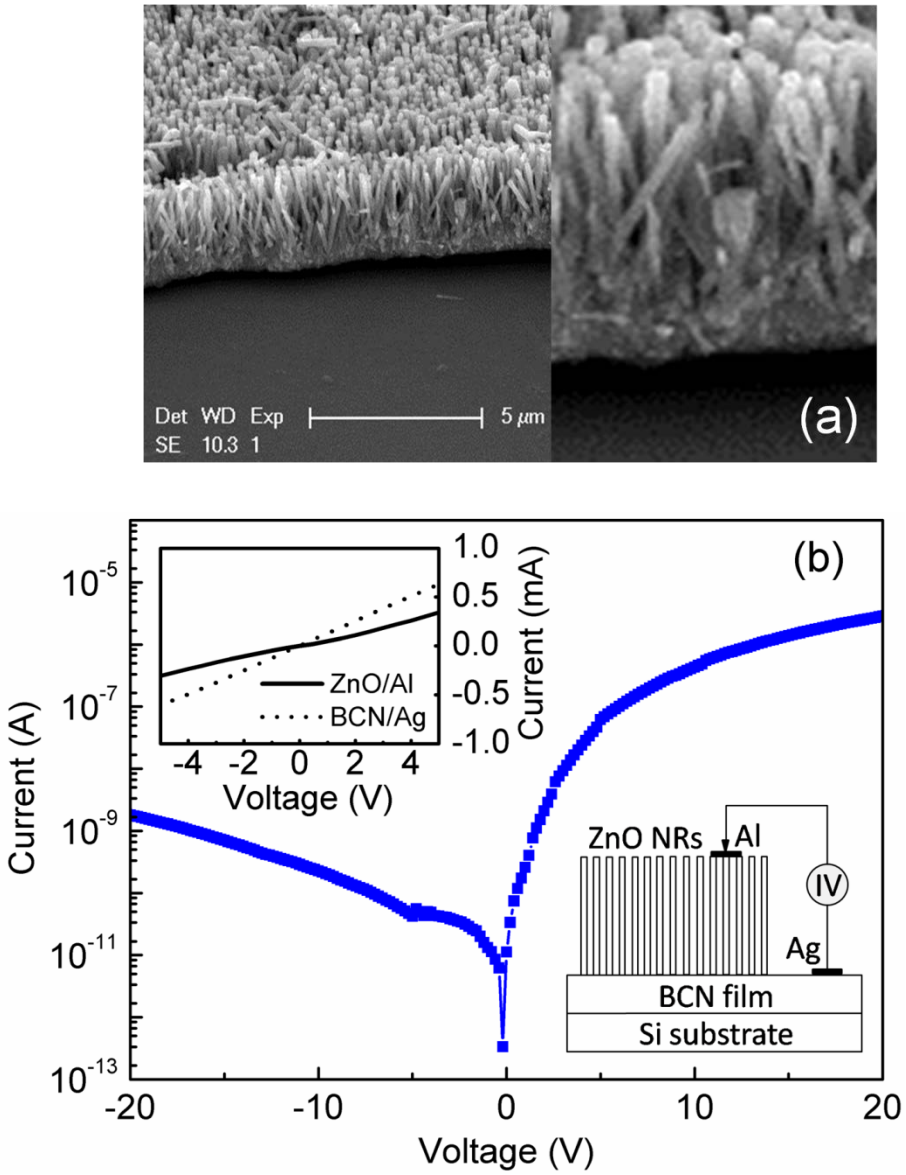

Figure 6.4 (a) SEM image of ZnO NRs in a cross sectional view; (b) *I-V* characteristics of a BCN/ZnO NRs heterojunction. Inset shows the *I-V* characteristics of ZnO/Al and BCN/Ag ohmic contacts and the schematic configuration of the heterojunction.

Al and Ag electrodes were employed to form ohmic contacts, as shown schematically in the insets of Figure 6.4 (b). The *I-V* characteristics of Ag/BCN and Al/ZnO ohmic junctions and BCN/ZnO-NRs heterojunctions are shown in Figure 6.4 (b). As the metal contacts to the films are ohmic in nature, a clear rectifying behavior of the junctions is revealed. The rectification ratio

(the forward-to-reverse current ratio) as high as 1500 at relatively low bias voltages of ±5 V has been demonstrated. This rectification performance appears significantly higher compared to our previous work on p-GaN/n-ZnO-NRs heterojunction LEDs with their rectification ratio of 320 at ±20 V [242]. In the case of ZnO/GaN heterostructures, one would expect a good lattice match as both the materials have hexagonal lattices, and their lattice parameters and band gap values are also very close. In contrast, in the case of BCN/ZnO heterostructures, such similarities are not expected. In fact, there are rather notable dissimilarities: ZnO is a wide gap semiconductor with a bandgap of 3.4 eV, while BCN is a narrow band gap semiconductor with a bandgap of ~1.0 eV. Thus a large band bending would occur at the heterointerface in the valence band region.

The *I*-*V* curve of a p-n heterojunction could be simulated by Shockley equation 6.1 for an ideal diode:

$$I = I_0\left[\exp\left(\frac{V}{nV_t}-1\right)\right], \tag{6.1}$$

where I_0 is the saturation current, $V_t = kT/q$ is the thermal voltage, q is the electronic charge, n is the ideality factor, k is the Boltzmann constant, and T is the absolute temperature. The ideality factor could thus be calculated from the slope of the linear region in the ln (I)−V plot and expressed as:

$$n = \frac{q}{kT}\frac{dV}{d(\ln I)}. \tag{6.2}$$

For $V < 0.5$ V, n was found to be around 2; for $V > 0.5$ V, it is much higher than 2. For an ideal p-n homojunction n is ~1, while in p-n homojunctions where the tunneling current mechanism is dominant, n is between 1 and 2. Considering the ideal diode model valid in the case of studied heterojunction diodes, dominance of tunneling current at low voltages appears to be valid in the first instance to explain the n of ~2. However, considering the band structure of the studied heterojunction the inter-band direct tunneling appears unlikely at small forward bias voltages. In such case, impurity assisted tunneling or band to impurity cascade processes may contribute to the tunneling current.

There are a number of defects anticipated in the studied structure: i) a large amount of defects in the as-deposited amorphous BCN films; ii) electronic defects in the ZnO synthesized by low-temperature solution based process [243]; iii) interface defects induced by the significant

mismatch of the ZnO and BCN lattices [244]. Some of these defects can be optically as well as electrically active, and influence the electrical transport [245]. Thus a cascade of tunneling is possible in the studied heterostructures. At high bias voltages a large deviation of n (> 2) is noted. Very large values of n ($2 < n < 8$) have been reported for diodes based on AlGaN/GaN p-n heterojunctions and GaN LEDs [246, 247] operating at high bias voltages.

Additional rectifying effects due to metal/semiconductor interfaces at high biases have been shown to contribute to the resulting rectification and the high value of n. Similar mechanism in the studied heterojunction is not unlikely. The demonstration of BCN based heterojunctions presented here shows their feasibility of application in electronic devices. However, further studies are necessary to better understand the electronic properties of BCN films and the transport mechanism behind the observed ideality factors.

6.4 Conclusions

In summary, BCN films were deposited by RF magnetron sputtering from a B_4C target using a N_2/Ar gas mixture. The atomic contents of boron, carbon, nitride, and oxygen were evaluated to be 44.5, 11.1, 38.7, and 5.7 at.%, respectively. The BCN films are composed of B−N, C−N, and B−C bonds in sp^2 and sp^3 configurations. The as-deposited BCN films show p-type conductivity with an optical band gap of 1.0 eV. ZnO NR arrays with n-type conductivity were grown on the BCN films to form p-n heterojunctions. The *I-V* characterization of the BCN/ZnO-NRs junctions shows a rectification behavior with a rectification ratio of 1500 at the bias voltages of ±5 V. The unique combination of optical and electronic properties of the BCN films with tunable optical band gap and the interesting device characteristics of the BCN/ZnO heterojunction diodes imply that the emerging ternary BCN materials are viable semiconductors for the fabrication of future electronic devices.

6.5 Acknowledgments

This work was supported by the Research Grants Council of the Hong Kong Special Administrative Region (Project No. CityU 104911), the National Science Foundation of China (NSFC Grant 61176007 and 51372213), and the Natural Sciences and Engineering Research Council (NSERC) of Canada.

CHAPTER 7 GENERAL DISCUSSION AND CONCLUSIONS

This chapter offers a summary of the principal results and discussion of the main achievements of this thesis and of the contributions to the field of research and technology in response to the objectives proposed in Chapter 1. First, we summarize the main conclusions resulting from the study on the $B_{1-x}C_x$, Ti−B−C, and BCN films, respectively, and compare their tribo-mechanical properties with those of other hard coatings. Then, the perspectives of the B-containing films for multi-functional protective coating applications are presented.

7.1 General discussion

B-containing hard protective coatings in this work are compared with other hard coatings with respect to the tribo-mechanical properties in terms of the *H*, *E*, and μ values (see Figure 7.1). This allows one to appreciate our contribution to the hard coating properties maps described in Chapter 2 (Figure 2.4 and 2.4) that can help to make judicious decisions with respect to specific applications.

B-containing coatings with their *H* values generally higher than 20 GPa (Figure 7.1 (a)) can be classified as hard coatings. *H* values of the $B_{1-x}C_x$ and Al−Mg−B films are generally in the range of 20−30 GPa, and the *H* variation with composition can be explained by the changes in film microstructure. Nanocomposite B-containing coatings with appropriate microstructure can reach superhardness levels (> 40 GPa). This is indeed the case for the Ti−B−C films formed by TiB_2 nanocrystallites in the amorphous $B_{1-x}C_x$ matrix studied here, or for the nanocomposite Al−Mg−B−Ti coatings with TiB_2 nanocrystals embedded in the Al−Mg−B matrix reported earlier [169].

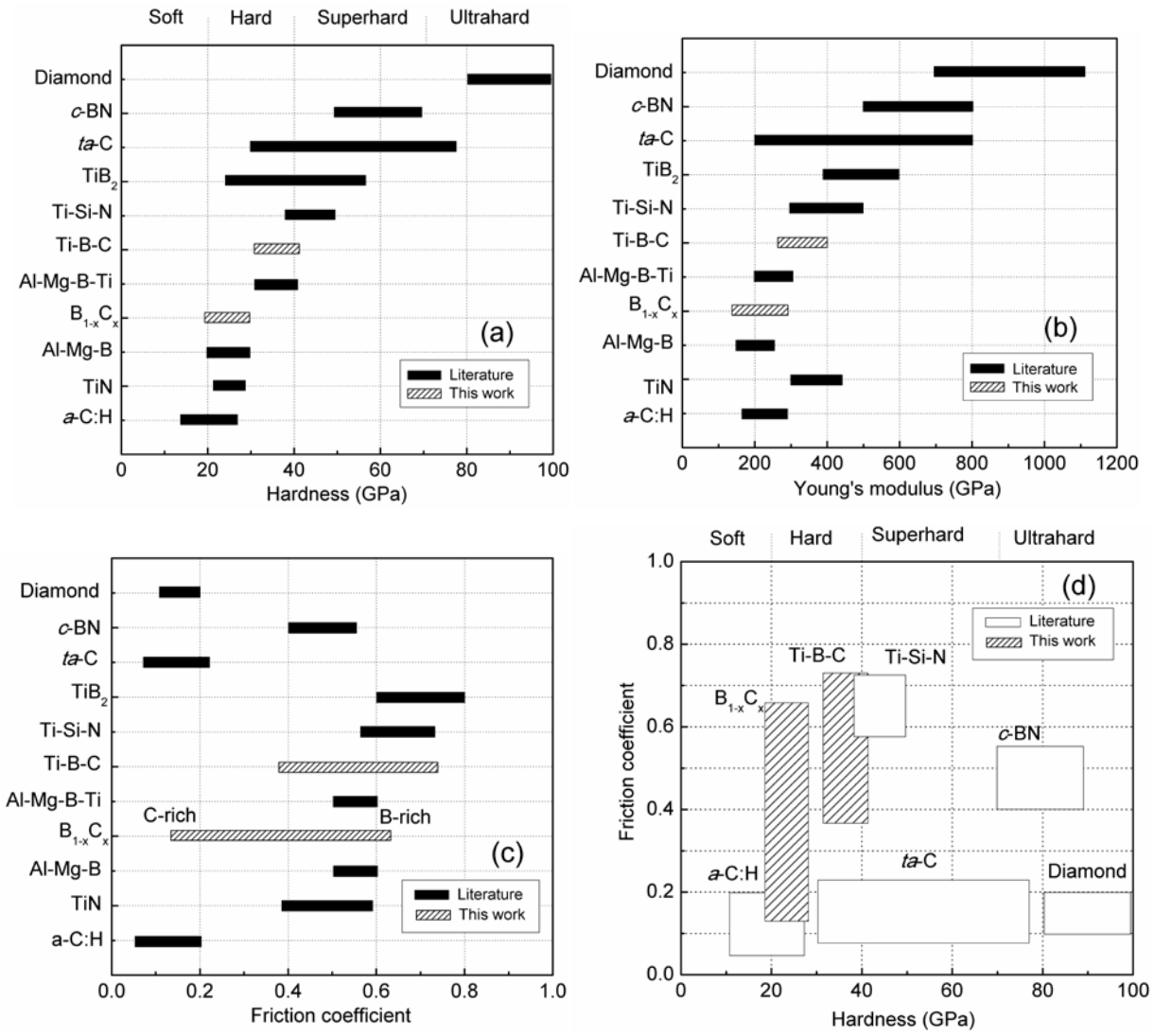

Figure 7.1 Tribo-mechanical properties for the most frequently studied hard protective coatings including our work on B-containing films: (a) hardness; (b) Young's modulus; (c) friction coefficient; (d) "Tribo-mechanical" map in terms of the hardness and friction coefficient.

Figure 7.1 (c) compares the tribological properties in terms of the friction coefficient. The μ and K values of the B-containing coatings vary over a large range depending on their composition and surface chemical characteristics. In the case of $B_{1-x}C_x$ films, the friction and wear can be reduced by increasing the carbon content due to the fact that the presence of an amorphous carbon component results in a graphite tribolayer acting as a solid lubricant during the wear process. For Ti−B−C films, lower μ and K values were achieved for the films with higher [Ti] due to the formation of a low-μ surface oxide layer within the wear track.

The B-containing coatings in this work are compared with different complementary hard protective coatings in the “tribo-mechanical” map in terms of hardness and friction coefficient as presented in Figure 7.1 (d). Clearly, the tribo-mechanical and corrosion properties of the B-containing films can be adjusted by controlling the composition and microstructure. This allows one to perform an appropriate selection of materials with respect to the specific tribological application and the corresponding performance requirements. The B-containing films with high hardness, adjustable tribological properties, and high corrosion resistance are promising materials for surface protection in various industrial applications. In addition, the unique optical and electronic properties of the BCN films and the interesting device characteristics of the BCN/ZnO heterojunction diodes open the door to apply B-containing films as multi-functional protective coatings.

7.2 Conclusions

B-containing films, including $B_{1-x}C_x$, Ti−B−C, and BCN films, were deposited using magnetron sputtering, and their tribo-mechanical and electrical properties were studied. The tribo-mechanical properties of the $B_{1-x}C_x$ films can be controlled by their composition and microstructure. Ti−B−C nanocomposite films were obtained by adding Ti into the $B_{1-x}C_x$ system with the intention of further improving the tribo-mechanical properties. In addition, BCN films were synthesized by adding N into the $B_{1-x}C_x$ system in order to explore their optical and electrical properties with respect to potential optoelectronic applications.

The mechanical properties of the $B_{1-x}C_x$ and Ti−B−C films can be tailored by adjusting their composition and microstructure. For example, $B_{1-x}C_x$ films ($0 < x < 1$) present a structure containing different proportions of amorphous and nanocrystalline phases. The $B_{0.81}C_{0.19}$ film with a nearly stoichiometric B/C ratio corresponding to B_4C exhibits the highest *H* value of 28 GPa due to the formation of nanocrystalline boron carbide, while the comparable *H* of the $B_{0.24}C_{0.76}$ film (25 GPa) is related to the formation of boron carbide nanocrystals imbedded in an amorphous boron carbide/*a*-C matrix with strong interfaces.

The Ti−B−C films exhibits a structure of TiB_2 nanocrystallites in the amorphous $B_{1-x}C_x$ matrix. Their hardness variation is closely related to the concentration and size of the TiB_2 nanocrystals which can be controlled by the Ti content. The films with [Ti] lower than 15.0 at.% exhibit a structure of small amounts of TiB_2 nanocrystallites embedded in an amorphous boron carbide matrix, which gives rise to *H* values in the range of 33−35 GPa. Rising [Ti] to 15.0 at.% leads to the increase of both the quantity and size of TiB_2 nanocrystallites, which results in the *H* values reaching ~38 GPa. As the [Ti] further increases to 20.0 at.%, the film structure features a larger amount and a larger size of TiB_2 nanocrystallites with a (001) preferred orientation. Consequently, the film's *H* value (~42 GPa) reaches super hard level.

The tribological properties of $B_{1-x}C_x$ and Ti−B−C films are affected by their composition and surface chemical characteristics. The μ and *K* values of $B_{1-x}C_x$ films can be reduced from 0.76 to 0.13 and from 6.4×10^{-5} to 1.3×10^{-7} mm^3/Nm, respectively, by increasing the [C] from 19 to 76 at.%. The decrease of friction and wear for the carbon-rich films is caused by the amorphous carbon component, which results in a graphite tribolayer acting as a solid lubricant.

Moreover, surface chemical characteristics can greatly affect the tribological performance as well. For instance, The Ti−B−C coatings with [Ti] of 10.0 at.% and of 17.0 at.% present μ values of 0.56 and 0.73, respectively. However, an increase of [Ti] to 22.6 at.% leads to a lower μ value of 0.37 due to the formation of a low-μ surface oxide layer acting as a solid lubricant, and its wear rate is decreased by about one order of magnitude accordingly.

Corrosion resistance is also very important for the selection of protective coatings, particularly for the coatings working in a corrosive environment such as sea water and biological fluids. Application of both the $B_{1-x}C_x$ and Ti−B−C coatings can significantly improve corrosion resistance of the M2 steel substrates as indicated by the decrease of i_o. The highest corrosion resistance is achieved for the $B_{0.81}C_{0.19}$ films as indicated by the $i_o = 8\times10^{-10}$ A/cm^2, which is four orders of magnitude lower than that of the bare M2 steel. For comparison, the Ti−B−C coatings present a lower corrosion resistance indicated by a higher i_o of 1.1×10^{-8} A/cm^2. Such differences are related to the film microstructure; specifically, the mainly amorphous nature of the predominately amorphous $B_{1-x}C_x$ films gives rise to a high corrosion resistance.

In addition to the evaluation of tribo-mechanical and corrosion performance of B-containing films, other properties such as optical and electrical characteristics are investigated as well. BCN films with B, C, N, and O concentrations of 44.5, 11.1, 38.7, and 5.7 at.%, respectively, were prepared by RF magnetron sputtering from a B_4C target using a N_2/Ar gas mixture. The BCN films exhibit an amorphous structure and are composed of B−N, C−N, and B−C bonds as identified by XPS and FTIR analyses. The BCN films exhibit an optical band gap of 1.0 eV and p-type conductivity. ZnO NR arrays with n-type conductivity were grown on the BCN films using hydrothermal synthesis to form p-n heterojunctions. The *I-V* characterization of the BCN/ZnO-NRs junctions shows a rectification behavior with a rectification ratio of 1500 at the bias voltages of ±5 V.

7.3 Perspectives

This thesis is primarily focused on the development of B-containing functional hard protective coatings with respect to improving the tribo-mechanical, corrosion, and electrical properties by structural control. It provides guidelines of controlling the microstructure of B-containing films, and accordingly the coating properties, which may be applicable to other

coating systems as well. It also established the background for other research directions and provided their potential of being applied in many other fields, namely the following ones:

(i) **Improving coating performance.** Binary and ternary B-containing films were systematically studied in this work. However, the coating performance may be further improved by developing quaternary B-containing coatings. Adding a fourth element such as Si or N can help to control the structural evolution in a multiphase coating system, and new properties or functions may be achieved when another phase is introduced. In addition, the electrical and mechanical properties of BCN films need to be further improved. BCN films were applied in the BCN/ZnO-NRs p-n junctions in this work. However, the mobility of the BCN films needs to be enhanced for real-life applications. The mechanical properties of the BCN films are not studied in this work. It would be interesting to develop BCN films with optimized electrical and mechanical properties for multifunctional applications.

(ii) **Nanocomposite design.** Hardness enhancement can be achieved by nanocomposite design, namely by forming nanocrystals in an amorphous or a nanocrystalline phase. In general, these phases are immiscible with each other to form well-defined spinodal structure at interfaces. In this work, the structural evolution of the Ti−B−C nanocomposite films with varied [Ti] gives us some clues for the future nanocomposite design. A self-organized structure of *nc*-TiB_2/*a*-boron carbide is formed when nanocrystalline TiB_2 phase is introduced in the amorphous boron carbide matrix by adding Ti. This is caused by the immiscibility of these two phases as well as the narrow single-phase region of TiB_2 ([B] = 65.6−66.7 at.%). The concentration and size of the TiB_2 nanocrystallites increase with the [Ti], and nanocolumnar structure forms when the [Ti] reaches certain value due to the preferred growth of TiB_2 along the (001) orientation. Therefore, one can expect that materials with structure and properties similar to TiB_2 such as zirconium diboride and hafnium diboride can be introduced as hard nanocrystalline phase to form nanocomposite, and hence their tribo-mechanical properties can be adjusted.

(iii) **Developing duplex thin-on-thick coating system.** Duplex thin-on-thick coatings can give a better performance in terms of tribo-mechanical and corrosion properties compared to single layer coatings. For example, high velocity oxy-fuel (HVOF) is a coating technique used to produce thick metallic and hard facing coatings. It is very attractive due to the high-velocity and low-temperature spraying process, as well as the possibility of using various kinds of materials

such as metals, alloys, ceramics, plastics, and composites. However, the porosity and high friction of HVOF coatings lead to a poor performance with respect to the corrosion and tribological resistance. Therefore, application of dense protective films, such as the sputtered B-containing coatings in this work, on the top of the HVOF coatings is expected to improve the corrosion resistance as well as the tribo-mechanical properties. The high load-carrying capacity of HVOF coatings and the gradual changes in H and E across the duplex coating system can reduce the interfacial stress and consequently improve the adhesion and the tribo-mechanical properties as well.

REFERENCES

[1] "Corrosion costs and preventive strategies in the United States," Available: http://www.nace.org/Publications/Cost-of-Corrosion-Study/

[2] K. Holmberg, P. Andersson, A. Erdemir, "Global energy consumption due to friction in passenger cars," Tribol Int, **47** (2012) 221.

[3] D.J. Li, S. Guruvenket, J.E. Klemberg-Sapieha, "Corrosion and tribo-corrosion enhancement of SS301 and Ti-6Al-4V substrates by amorphous hydrogenated SiN/SiC/*a*-C multilayer coating architecture," Surf Coat Tech, **206** (2011) 1893.

[4] D.J. Li, S. Guruvenket, M. Azzi, J.A. Szpunar, J.E. Klemberg-Sapieha, L. Martinu, "Corrosion and tribo-corrosion behavior of *a*-SiC_x:H, *a*-SiN_x:H and *a*-SiC_xN_y:H coatings on SS301 substrate," Surf Coat Tech, **204** (2010) 1616.

[5] M. Azzi, M. Benkahoul, J.E. Klemberg-Sapieha, L. Martinu, "Corrosion and mechanical properties of duplex-treated 301 stainless steel," Surf Coat Tech, **205** (2010) 1557.

[6] M. Benkahoul, P. Robin, L. Martinu, J.E. Klemberg-Sapieha, "Tribological properties of duplex Cr-Si-N coatings on SS410 steel," Surf Coat Tech, **203** (2009) 934.

[7] M. Azzi, M. Paquette, J.A. Szpunar, J.E. Klemberg-Sapieha, L. Martinu, "Tribocorrosion behaviour of DLC-coated 316L stainless steel," Wear, **267** (2009) 860.

[8] S. Hassani, J.E. Klemberg-Sapieha, L. Martinu, "Mechanical, tribological and erosion behaviour of super-elastic hard Ti-Si-C coatings prepared by PECVD," Surf Coat Tech, **205** (2010) 1426.

[9] S. Guruvenket, M. Azzi, D. Li, J.A. Szpunar, L. Martinu, J.E. Klemberg-Sapieha, "Structural, mechanical, tribological, and corrosion properties of *a*-SiC:H coatings prepared by PECVD," Surf Coat Tech, **204** (2010) 3358.

[10] S. Guruvenket, D. Li, J.E. Klemberg-Sapieha, L. Martinu, J. Szpunar, "Mechanical and tribological properties of duplex treated TiN, *nc*-TiN/*a*-SiN_x and *nc*-TiCN/*a*-SiCN coatings deposited on 410 low alloy stainless steel," Surf Coat Tech, **203** (2009) 2905.

[11] P. Jedrzejowski, J. Cizek, A. Amassian, J.E. Klemberg-Sapieha, J. Vlcek, L. Martinu, "Mechanical and optical properties of hard SiCN coatings prepared by PECVD," Thin Solid Films, **447** (2004) 201.

[12] A.C. Reardon, Metallurgy for the Non-Metallurgist, Second Edition, ASM International., 2011.

[13] K. Holmberg, A. Matthews, Coatings Tribology: Properties, Mechanisms, Techniques and Applications in Surface Engineering, Elsevier Science, 2009.

[14] J.H. Arps, R.A. Page, G. Dearnaley, "Reduction of wear in critical engine components using ion-beam-assisted deposition and ion implantation," Surf Coat Tech, **84** (1996) 579.

[15] C.P.O. Treutler, "Industrial use of plasma-deposited coatings for components of automotive fuel injection systems," Surf Coat Tech, **200** (2005) 1969.

[16] Y. Pauleau, P.B. Barna, Protective Coatings and Thin Films: Synthesis, Characterization, and Applications, Springer Netherlands, 1996.

[17] C.A. Love, R.B. Cook, T.J. Harvey, P.A. Dearnley, R.J.K. Wood, "Diamond like carbon coatings for potential application in biological implants − a review," Tribol Int, **63** (2013) 141.

[18] Y. Chen, Y.-W. Chung, S.-Y. Li, "Boron carbide and boron carbonitride thin films as protective coatings in ultra-high density hard disk drives," Surf Coat Tech, **200** (2006) 4072.

[19] D.J. Li, M.U. Guruz, C.S. Bhatia, Y.-W. Chung, "Ultrathin CN_x overcoats for 1 Tb/in.^{2} hard disk drive systems," Appl Phys Lett, **81** (2002) 1113.

[20] T.W. Scharf, R.D. Ott, D. Yang, J.A. Barnard, "Structural and tribological characterization of protective amorphous diamond-like carbon and amorphous CN_x overcoats for next generation hard disks," J Appl Phys, **85** (1999) 3142.

[21] M.K. Fung, K.H. Lai, H.L. Lai, C.Y. Chan, N.B. Wong, I. Bello, C.S. Lee, S.T. Lee, "Diamond-like carbon coatings applied to hard disks," Diam Relat Mater, **9** (2000) 815.

[22] M. Schlatter, "DLC-based wear protection on magnetic storage media," Diam Relat Mater, **11** (2002) 1781.

[23] P.M. Martin, Handbook of Deposition Technologies for Films and Coatings - Science, Applications and Technology (3rd Edition), William Andrew Publishing, 2010.

[24] A.A. Voevodin, M.A. Capano, S.J.P. Laube, M.S. Donley, J.S. Zabinski, "Design of a Ti/TiC/DLC functionally gradient coating based on studies of structural transitions in Ti–C thin films," Thin Solid Films, **298** (1997) 107.

[25] P.H. Mayrhofer, C. Mitterer, L. Hultman, H. Clemens, "Microstructural design of hard coatings," Prog Mater Sci, **51** (2006) 1032.

[26] P. Jedrzejowski, Mechanical and optical properties of plasma deposited superhard nanocomposite coatings, Engineering physics, École Polytechnique de Montréal, Montreal, 2003.

[27] A. Leyland, A. Matthews, "On the significance of the H/E ratio in wear control: a nanocomposite coating approach to optimised tribological behaviour," Wear, **246** (2000) 1.

[28] J. Musil, "Hard and superhard nanocomposite coatings," Surf Coat Tech, **125** (2000) 322.

[29] R.F. Bunshah, Handbook of Hard Coatings: Deposition Technologies, Properties and

Applications, Noyes Publications, 2001.

[30] E.A. Almond, "Aspects of various processes for coating and surface hardening," Vacuum, **34** (1984) 835.

[31] M.L. Cohen, "Calculation of bulk moduli of diamond and zinc-blende solids," Phys Rev B, **32** (1985) 7988.

[32] A.Y. Liu, M.L. Cohen, "Prediction of new low compressibility solids," Science, **245** (1989) 841.

[33] J. Musil, "Hard nanocomposite coatings: Thermal stability, oxidation resistance and toughness," Surf Coat Tech, **207** (2012) 50.

[34] S. Vepřek, "The search for novel, superhard materials," J Vac Sci Technol A, **17** (1999) 2401.

[35] A. Anders, "A structure zone diagram including plasma-based deposition and ion etching," Thin Solid Films, **518** (2010) 4087.

[36] I. Petrov, P.B. Barna, L. Hultman, J.E. Greene, "Microstructural evolution during film growth," J Vac Sci Technol A, **21** (2003) S117.

[37] S.M. Rossnagel, "Energetic particle bombardment of films during magnetron sputtering," J Vac Sci Technol A, **7** (1989) 1025.

[38] H. Windischmann, "An intrinsic stress scaling law for polycrystalline thin films prepared by ion beam sputtering," J Appl Phys, **62** (1987) 1800.

[39] K. Holmberg, H. Ronkainen, A. Matthews, "Tribology of thin coatings," Ceram Int, **26** (2000) 787.

[40] N. Savvides, T.J. Bell, "Microhardness and Young's modulus of diamond and diamondlike carbon films," J Appl Phys, **72** (1992) 2791.

[41] A.T. Collins, "Synthetic diamond: Emerging CVD science and technology," Chem Vapor Depos, **1** (1995) 33.

[42] W. Matthias, B. Kai, F. Hans-Jörg, Synthesis of Nanodiamond, in: Carbon-based Nanomaterials and Hybrids, Pan Stanford Publishing, 2014, 5.

[43] M. Schwander, K. Partes, "A review of diamond synthesis by CVD processes," Diam Relat Mater, **20** (2011) 1287.

[44] J. Hu, Y.K. Chou, R.G. Thompson, J. Burgess, S. Street, "Characterizations of nano-crystalline diamond coating cutting tools," Surf Coat Tech, **202** (2007) 1113.

[45] J.E. Butler, H. Windischmann, "Developments in CVD-diamond synthesis during the past decade," Mrs Bull, **23** (1998) 22.

[46] W. Zhang, I. Bello, Y. Lifshitz, K.M. Chan, X. Meng, Y. Wu, C.Y. Chan, S.T. Lee, "Epitaxy on diamond by chemical vapor deposition: A route to high-quality cubic boron nitride for electronic applications," Adv Mater, **16** (2004) 1405.

[47] Y. Liou, A. Inspektor, R. Weimer, R. Messier, "Low‐temperature diamond deposition by microwave plasma‐enhanced chemical vapor deposition," Appl Phys Lett, **55** (1989) 631.

[48] W.J. Zhang, Y.M. Chong, I. Bello, S.T. Lee, "Nucleation, growth and characterization of cubic boron nitride (*c*BN) films," J Phys D: Appl Phys, **40** (2007) 6159.

[49] S. Ulrich, J. Schwan, W. Donner, H. Ehrhardt, "Knock-on subplantation-induced formation of nanocrystalline *c*-BN with r.f. magnetron sputtering and r.f. argon ion plating," Diam Relat Mater, **5** (1996) 548.

[50] V.L. Solozhenko, V.Z. Turkevich, W.B. Holzapfel, "Refined phase diagram of boron nitride," J Phys Chem B, **103** (1999) 2903.

[51] Y.M. Chong, W.J. Zhang, Y. Yang, Q. Ye, I. Bello, S.T. Lee, "Deposition of cubic boron nitride films on diamond-coated WC:Co inserts," Diam Relat Mater, **18** (2009) 1387.

[52] I. Bello, C.Y. Chan, W.J. Zhang, Y.M. Chong, K.M. Leung, S.T. Lee, Y. Lifshitz, "Deposition of thick cubic boron nitride films: The route to practical applications," Diam Relat Mater, **14** (2005) 1154.

[53] W.J. Zhang, S. Matsumoto, Q. Li, I. Bello, S.T. Lee, "Growth behavior of cubic boron nitride films in a two-step process: changing bias voltage, gas composition, and substrate temperature," Adv Funct Mater, **12** (2002) 250.

[54] D. Litvinov, R. Clarke, "In situ texture monitoring for growth of oriented cubic boron nitride films," Appl Phys Lett, **74** (1999) 955.

[55] S. Amagi, D. Takahashi, T. Yoshida, "Threshold sheath potential for the nucleation and growth of cubic boron nitride by inductively coupled plasma enhanced chemical-vapor deposition," Appl Phys Lett, **70** (1997) 946.

[56] P.B. Mirkarimi, D.L. Medlin, K.F. McCarty, D.C. Dibble, W.M. Clift, J.A. Knapp, J.C. Barbour, "The synthesis, characterization, and mechanical properties of thick, ultrahard cubic boron nitride films deposited by ion-assisted sputtering," J Appl Phys, **82** (1997) 1617.

[57] C. Fitz, A. Kolitsch, W. Fukarek, "Stress relaxation during annealing of boron nitride films," Thin Solid Films, **389** (2001) 173.

[58] K. Bewilogua, M. Keunecke, K. Weigel, E. Wiemann, "Growth and characterization of thick *c*BN coatings on silicon and tool substrates," Thin Solid Films, **469** (2004) 86.

[59] M. Keunecke, K. Yamamoto, K. Bewilogua, "Mechanical and tribological properties of *c*BN films on silicon and tungsten carbide substrates," Thin Solid Films, **398** (2001) 142.

[60] E. Tomasella, L. Thomas, M. Dubois, C. Meunier, "Structural and mechanical properties of *a*-C:H thin films grown by RF-PECVD," Diam Relat Mater, **13** (2004) 1618.

[61] G. Capote, R. Prioli, P.M. Jardim, A.R. Zanatta, L.G. Jacobsohn, F.L. Freire Jr, "Amorphous hydrogenated carbon films deposited by PECVD: influence of the substrate temperature on film growth and microstructure," J Non-Cryst Solids, **338–340** (2004) 503.

[62] H. Ronkainen, S. Varjus, J. Koskinen, K. Holmberg, "Differentiating the tribological performance of hydrogenated and hydrogen-free DLC coatings," Wear, **249** (2001) 260.

[63] A. Grill, "Diamond-like carbon: state of the art," Diam Relat Mater, **8** (1999) 428.

[64] A. Erdemir, C. Donnet, Tribology of Diamond, Diamond-like Carbon and Related Films, in: Modern Tribology Handbook, Two Volume Set, CRC Press, 2000.

[65] J. Robertson, E.P. O'Reilly, "Electronic and atomic structure of amorphous carbon," Phys Rev B, **35** (1987) 2946.

[66] A. Erdemir, C. Donnet, "Tribology of diamond-like carbon films: recent progress and future prospects," J Phys D: Appl Phys, **39** (2006) R311.

[67] W.G. Cui, Q.B. Lai, L. Zhang, F.M. Wang, "Quantitative measurements of sp3 content in DLC films with Raman spectroscopy," Surf Coat Tech, **205** (2010) 1995.

[68] S. Zhang, X. Lam Bui, Y. Fu, "Magnetron sputtered hard *a*-C coatings of very high toughness," Surf Coat Tech, **167** (2003) 137.

[69] J. Robertson, "Properties of diamond-like carbon," Surf Coat Tech, **50** (1992) 185.

[70] C. Donnet, "Recent progress on the tribology of doped diamond-like and carbon alloy coatings: a review," Surf Coat Tech, **100–101** (1998) 180.

[71] M. Ikeyama, S. Nakao, Y. Miyagawa, S. Miyagawa, "Effects of Si content in DLC films on their friction and wear properties," Surf Coat Tech, **191** (2005) 38.

[72] S. Xu, D. Flynn, B.K. Tay, S. Prawer, K.W. Nugent, S.R.P. Silva, Y. Lifshitz, W.I. Milne, "Mechanical properties and Raman spectra of tetrahedral amorphous carbon films with high sp3 fraction deposited using a filtered cathodic arc," Philosophical Magazine Part B, **76** (1997) 351.

[73] A. Grill, "Tribology of diamondlike carbon and related materials: an updated review," Surf Coat Tech, **94–95** (1997) 507.

[74] A. Grill, "Review of the tribology of diamond-like carbon," Wear, **168** (1993) 143.

[75] J. Andersson, R.A. Erck, A. Erdemir, "Friction of diamond-like carbon films in different atmospheres," Wear, **254** (2003) 1070.

[76] C. Donnet, A. Grill, "Friction control of diamond-like carbon coatings," Surf Coat Tech, **94–**

95 (1997) 456.

[77] B. Tomcik, T. Osipowicz, J.Y. Lee, "Diamond-like film as a corrosion protective layer on the hard disk," Thin Solid Films, **360** (2000) 173.

[78] A.C. Ferrari, "Diamond-like carbon for magnetic storage disks," Surf Coat Tech, **180–181** (2004) 190.

[79] G. Dearnaley, J.H. Arps, "Biomedical applications of diamond-like carbon (DLC) coatings: A review," Surf Coat Tech, **200** (2005) 2518.

[80] A.A. Gharam, M.J. Lukitsch, Y. Qi, A.T. Alpas, "Role of oxygen and humidity on the tribo-chemical behaviour of non-hydrogenated diamond-like carbon coatings," Wear, **271** (2011) 2157.

[81] H. Abdullah Tasdemir, M. Wakayama, T. Tokoroyama, H. Kousaka, N. Umehara, Y. Mabuchi, T. Higuchi, "Wear behaviour of tetrahedral amorphous diamond-like carbon (*ta*-C DLC) in additive containing lubricants," Wear, **307** (2013) 1.

[82] Y. Mabuchi, T. Higuchi, Y. Inagaki, H. Kousaka, N. Umehara, "Wear analysis of hydrogen-free diamond-like carbon coatings under a lubricated condition," Wear, **298–299** (2013) 48.

[83] M.L. Cohen, "Predicting useful materials," Science, **261** (1993) 307.

[84] J. He, L. Guo, X. Guo, R. Liu, Y. Tian, H. Wang, C. Gao, "Predicting hardness of dense C_3N_4 polymorphs," Appl Phys Lett, **88** (2006)

[85] R.C. DeVries, "Inventory on innovative research: the case of C_3N_4," Mat Res Innovat, **1** (1997) 161.

[86] J. Jiang, W. Cheng, Y. Zhang, M. Lan, H. Zhu, D. Shen, "Deposition of crystalline C_3N_4 films via microwave plasma chemical vapour deposition," Mater Lett, **61** (2007) 2243.

[87] J.P. Rivière, D. Texier, J. Delafond, M. Jaouen, E.L. Mathé, J. Chaumont, "Formation of the crystalline β-C_3N_4 phase by dual ion beam sputtering deposition," Mater Lett, **61** (2007) 2855.

[88] K. Kato, N. Umehara, K. Adachi, "Friction, wear and N_2-lubrication of carbon nitride coatings: a review," Wear, **254** (2003) 1062.

[89] J. Vlček, K. Rusňák, V. Hájek, L. Martinu, "New approach to understanding the reactive magnetron sputtering of hard carbon nitride films," Diam Relat Mater, **9** (2000) 582.

[90] V. Hajek, K. Rusnak, J. Vlcek, L. Martinu, H.M. Hawthorne, "Tribological study of CN_x films prepared by reactive d.c. magnetron sputtering," Wear, **213** (1997) 80.

[91] E. Broitman, N. Hellgren, O. Wänstrand, M.P. Johansson, T. Berlind, H. Sjöström, J.E. Sundgren, M. Larsson, L. Hultman, "Mechanical and tribological properties of CN_x films deposited by reactive magnetron sputtering," Wear, **248** (2001) 55.

[92] J. Koskinen, J.P. Hirvonen, J. Levoska, P. Torri, "Tribological characterization of carbon-nitrogen coatings deposited by using vacuum arc discharge," Diam Relat Mater, **5** (1996) 669.

[93] D. Li, E. Cutiongco, Y.-W. Chung, M.-S. Wong, W.D. Sproul, "Composition, structure and tribological properties of amorphous carbon nitride coatings," Surf Coat Tech, **68–69** (1994) 611.

[94] J. Kalaš, R. Vernhes, S. Hřeben, J. Vlček, J.E. Klemberg-Sapieha, L. Martinu, "High-temperature stability of the mechanical and optical properties of Si–B–C–N films prepared by magnetron sputtering," Thin Solid Films, **518** (2009) 174.

[95] Y. Zhang, J. Li, L. Zhou, S. Xiang, "A theoretical study on the chemical bonding of 3d-transition-metal carbides," Solid State Commun, **121** (2002) 411.

[96] P.H. Mayrhofer, Materials science aspects of nanocrystalline PVD hard coatings, Department of Physical Metallurgy and Materials Testing, The university of Leoben, Leoben, USA, 2001.

[97] G. Abadias, "Stress and preferred orientation in nitride-based PVD coatings," Surf Coat Tech, **202** (2008) 2223.

[98] S. PalDey, S.C. Deevi, "Single layer and multilayer wear resistant coatings of (Ti,Al)N: a review," Mater Sci Eng A, **342** (2003) 58.

[99] P.H. Mayrhofer, G. Tischler, C. Mitterer, "Microstructure and mechanical/thermal properties of Cr–N coatings deposited by reactive unbalanced magnetron sputtering," Surf Coat Tech, **142–144** (2001) 78.

[100] P.H. Mayrhofer, F. Kunc, J. Musil, C. Mitterer, "A comparative study on reactive and non-reactive unbalanced magnetron sputter deposition of TiN coatings," Thin Solid Films, **415** (2002) 151.

[101] P.H. Mayrhofer, C. Mitterer, J. Musil, "Structure–property relationships in single- and dual-phase nanocrystalline hard coatings," Surf Coat Tech, **174–175** (2003) 725.

[102] S. Vepřek, M.G.J. Vepřek-Heijman, P. Karvankova, J. Prochazka, "Different approaches to superhard coatings and nanocomposites," Thin Solid Films, **476** (2005) 1.

[103] P.H. Mayrhofer, H. Clemens, C. Mitterer, "Interfaces in nanostructured thin films and their influence on hardness," Z Metallkd, **96** (2005) 468.

[104] M. Philip, "Nanostructured materials," Rep Prog Phys, **64** (2001) 297.

[105] U. Helmersson, S. Todorova, S.A. Barnett, J.E. Sundgren, L.C. Markert, J.E. Greene, "Growth of single - crystal TiN/VN strained - layer superlattices with extremely high mechanical hardness," J Appl Phys, **62** (1987) 481.

[106] M. Shinn, L. Hultman, S.A. Barnett, "Growth, structure, and microhardness of epitaxial TiN/NbN superlattices," J Mater Res, **7** (1992) 901.

[107] K.K. Shih, D.B. Dove, "Ti/Ti‐N Hf/Hf‐N and W/W‐N multilayer films with high mechanical hardness," Appl Phys Lett, **61** (1992) 654.

[108] J.L. Lin, J.J. Moore, B. Mishra, M. Pinkas, W.D. Sproul, "The structure and mechanical and tribological properties of TiBCN nanocomposite coatings," Acta Mater, **58** (2010) 1554.

[109] S. Zhang, D. Sun, Y. Fu, H. Du, "Recent advances of superhard nanocomposite coatings: a review," Surf Coat Tech, **167** (2003) 113.

[110] L. Shizhi, S. Yulong, P. Hongrui, "Ti-Si-N films prepared by plasma-enhanced chemical vapor deposition," Plasma Chem Plasma P, **12** (1992) 287.

[111] S. Veprek, S. Reiprich, "A concept for the design of novel superhard coatings," Thin Solid Films, **268** (1995) 64.

[112] S. Vepřek, S. Reiprich, S.H. Li, "Superhard Nanocrystalline Composite-Materials - the TiN/Si_3N_4 System," Appl Phys Lett, **66** (1995) 2640.

[113] M. Bouchacourt, F. Thevenot, "Analytical investigations in the B-C system," Journal of the Less Common Metals, **82** (1981) 219.

[114] P. Jedrzejowski, J.E. Klemberg-Sapieha, L. Martinu, "Relationship between the mechanical properties and the microstructure of nanocomposite TiN/SiN1.3 coatings prepared by low temperature plasma enhanced chemical vapor deposition," Thin Solid Films, **426** (2003) 150.

[115] J. Patscheider, "Nanocomposite Hard Coatings for Wear Protection," Mrs Bull, **28** (2003) 180.

[116] N.N. Greenwood, A. Earnshaw, Chemistry of the elements, Pergamon Press, 1984.

[117] M.K. Lei, Q. Li, Z.F. Zhou, I. Bello, C.S. Lee, S.T. Lee, "Characterization and optical investigation of BCN film deposited by RF magnetron sputtering," Thin Solid Films, **389** (2001) 194.

[118] S. Ulrich, H. Ehrhardt, J. Schwan, R. Samlenski, R. Brenn, "Subplantation effect in magnetron sputtered superhard boron carbide thin films," Diam Relat Mater, **7** (1998) 835.

[119] I. Jiménez, D.G.J. Sutherland, T. van Buuren, J.A. Carlisle, L.J. Terminello, F.J. Himpsel, "Photoemission and x-ray-absorption study of boron carbide and its surface thermal stability," Phys Rev B, **57** (1998) 13167.

[120] K. Jagannadham, T.R. Watkins, M.J. Lance, L. Riester, R.L. Lemaster, "Laser physical vapor deposition of boron carbide films to enhance cutting tool performance," Surf Coat Tech, **203** (2009) 3151.

[121] K. Miyazaki, T. Hagio, K. Kobayashi, "Graphite and boron carbide composites made by hot-pressing," J Mater Sci, **16** (1981) 752.

[122] A.K. Suri, C. Subramanian, J.K. Sonber, T.S.R.C. Murthy, "Synthesis and consolidation of boron carbide: a review," Int Mater Rev, **55** (2010) 4.

[123] D. Emin, "Structure and single-phase regime of boron carbides," Phys Rev B, **38** (1988) 6041.

[124] C. Wood, D. Emin, "Conduction mechanism in boron carbide," Phys Rev B, **29** (1984) 4582.

[125] M.M. Balakrishnarajan, P.D. Pancharatna, R. Hoffmann, "Structure and bonding in boron carbide: The invincibility of imperfections," New J Chem, **31** (2007) 473.

[126] R. Lazzari, N. Vast, J.M. Besson, S. Baroni, A. Dal Corso, "Atomic Structure and Vibrational Properties of Icosahedral B_4C Boron Carbide," Phys Rev Lett, **83** (1999) 3230.

[127] H. Werheit, U. Kuhlmann, T. Lundström, "On the insertion of carbon atoms in B12 icosahedra and the structural anisotropy of β-rhombohedral boron and boron carbide," J Alloy Compd, **204** (1994) 197.

[128] B. Morosin, G.H. Kwei, A.C. Lawson, T.L. Aselage, D. Emin, "Neutron powder diffraction refinement of boron carbides - Nature of intericosahedral chains," J Alloy Compd, **226** (1995) 121.

[129] G.H. Kwei, B. Morosin, "Structures of the boron-rich boron carbides from neutron powder diffraction: Implications for the nature of the inter-icosahedral chains," J Phys Chem, **100** (1996) 8031.

[130] H.K. Clark, J.L. Hoard, "The crystal structure of boron carbide," J Am Chem Soc, **65** (1943) 2115.

[131] K. Shirai, S. Emura, S.i. Gonda, Y. Kumashiro, "Infrared study of amorphous $B_{1-x}C_x$ films," J Appl Phys, **78** (1995) 3392.

[132] M.J. Zhou, S.F. Wong, C.W. Ong, Q. Li, "Microstructure and mechanical properties of B_4C films deposited by ion beam sputtering," Thin Solid Films, **516** (2007) 336.

[133] D.R. Tallant, T.L. Aselage, A.N. Campbell, D. Emin, "Boron carbide structure by Raman spectroscopy," Phys Rev B, **40** (1989) 5649.

[134] "Handbook of ceramic hard materials," Available: http://www.hardmaterials.de/index.html

[135] K. Umeda, Y. Enomoto, A. Mitsui, K. Mannami, "Friction and wear of boride ceramics in air and water," Wear, **169** (1993) 63.

[136] P. Larsson, N. Axén, S. Hogmark, "Tribofilm formation on boron carbide in sliding wear," Wear, **236** (1999) 73.

[137] H.S. Ahn, P.D. Cuong, E.S. Yoon, K.H. Shin, "Effects of relative humidity on tribological properties of boron carbide coating against steel," Surf Coat Tech, **201** (2006) 4230.

[138] K.W. Lee, S.J. Harris, "Boron carbide films grown from microwave plasma chemical vapor deposition," Diam Relat Mater, **7** (1998) 1539.

[139] M.J. Santos, A.J. Silvestre, O. Conde, "Laser-assisted deposition of r-B_4C coatings using ethylene as carbon precursor," Surf Coat Tech, **151** (2002) 160.

[140] S. Adenwalla, N. Hong, M.A. Langell, J. Liu, O. Kizilkaya, "Ni doping of semiconducting boron carbide," J Appl Phys, **107** (2010)

[141] L.G. Jacobsohn, M. Nastasi, "Sputter-deposited boron carbide films: Structural and mechanical characterization," Surf Coat Tech, **200** (2005) 1472.

[142] L.G. Jacobsohn, R.K. Schulze, M.E.H.M. da Costa, M. Nastasi, "X-ray photoelectron spectroscopy investigation of boron carbide films deposited by sputtering," Surf Sci, **572** (2004) 418.

[143] D.B. Chrisey, R.Q. Bao, "Chemical states of carbon in amorphous boron carbide thin films deposited by radio frequency magnetron sputtering," Thin Solid Films, **519** (2010) 164.

[144] I. Jimenez, I. Caretti, J.M. Albella, "Tribological study of amorphous BC4N coatings," Diam Relat Mater, **16** (2007) 63.

[145] E. Restrepo-Parra, H.A. Castillo, J.M. Velez, W. de la Cruz, "Substrate temperature influence on boron carbide coatings grown by the PLD technique," Surf Coat Tech, **205** (2011) 3607.

[146] R. Ctvrtlik, V. Kulikovsky, V. Vorlicek, R. Bohac, M. Stranyanek, A. Dejneka, L. Jastrabik, "Mechanical properties and structure of amorphous and crystalline B_4C films," Diam Relat Mater, **18** (2009) 27.

[147] V. Kulikovsky, V. Vorlicek, R. Ctvrtlik, P. Bohac, L. Jastrabik, H. Lapsanska, "Effect of air annealing on mechanical properties and structure of amorphous B_4C films," Surf Coat Tech, **205** (2011) 4052.

[148] D.M. Bylander, L. Kleinman, "Structure of $B_{13}C_2$," Phys Rev B, **43** (1991) 1487.

[149] D.M. Bylander, L. Kleinman, S. Lee, "Self-consistent calculations of the energy bands and bonding properties of $B_{12}C_3$," Phys Rev B, **42** (1990) 1394.

[150] H. Werheit, M. Laux, U. Kuhlmann, R. Telle, "Optical interband transitions of boron carbide," Phys Status Solidi B, **172** (1992) K81.

[151] R. Schmechel, H. Werheit, "Correlation between structural defects and electronic properties of icosahedral boron-rich solids," J Phys: Condens Matter, **11** (1999) 6803.

[152] S. Lee, J. Mazurowski, G. Ramseyer, P.A. Dowben, "Characterization of boron carbide thin

films fabricated by plasma enhanced chemical vapor deposition from boranes," J Appl Phys, **72** (1992) 4925.

[153] B.W. Robertson, S. Adenwalla, A. Harken, P. Welsch, J.I. Brand, P.A. Dowben, J.P. Claassen, "A class of boron-rich solid-state neutron detectors," Appl Phys Lett, **80** (2002) 3644.

[154] S. Adenwalla, P. Welsch, A. Harken, J.I. Brand, A. Sezer, B.W. Robertson, "Boron carbide/n-silicon carbide heterojunction diodes," Appl Phys Lett, **79** (2001) 4357.

[155] E. Day, M.J. Diaz, S. Adenwalla, "Effect of bias on neutron detection in thin semiconducting boron carbide films," J Phys D: Appl Phys, **39** (2006) 2920.

[156] S.D. Hwang, K. Yang, P.A. Dowben, A.A. Ahmad, N.J. Ianno, J.Z. Li, J.Y. Lin, H.X. Jiang, D.N. McIlroy, "Fabrication of n-type nickel doped $B_5C_{1+\delta}$ homojunction and heterojunction diodes," Appl Phys Lett, **70** (1997) 1028.

[157] R.G. Munro, "Material properties of titanium diboride," J. Res. Natl. Inst. Stand. Technol., **105** (2000) 709.

[158] M. Berger, L. Karlsson, M. Larsson, S. Hogmark, "Low stress TiB_2 coatings with improved tribological properties," Thin Solid Films, **401** (2001) 179.

[159] P.H. Mayrhofer, C. Mitterer, J.G. Wen, J.E. Greene, I. Petrov, "Self-organized nanocolumnar structure in superhard TiB_2 thin films," Appl Phys Lett, **86** (2005)

[160] S.H. Lee, K.H. Nam, S.C. Hong, J.J. Lee, "Low temperature deposition of TiB_2 by inductively coupled plasma assisted CVD," Surf Coat Tech, **201** (2007) 5211.

[161] V. Ferrando, D. Marre, P. Manfrinetti, I. Pallecchi, C. Tarantini, C. Ferdeghini, "Pulsed laser deposition of epitaxial titanium diboride thin films," Thin Solid Films, **444** (2003) 91.

[162] L. Maya, C.E. Vallet, J.N. Fiedor, "Reactive sputtering of titanium diboride and titanium disilicide," J Vac Sci Technol A, **15** (1997) 2007.

[163] C.M.T. Sanchez, B.R. Plata, M. da Costa, F.L. Freire, "Titanium diboride thin films produced by dc-magnetron sputtering: Structural and mechanical properties," Surf Coat Tech, **205** (2011) 3698.

[164] M. Mikula, B. Grancic, V. Bursikova, A. Csuba, M. Drzik, S. Kavecky, A. Plecenik, P. Kus, "Mechanical properties of superhard TiB_2 coatings prepared by DC magnetron sputtering," Vacuum, **82** (2007) 278.

[165] P.H. Mayrhofer, C. Mitterer, J.G. Wen, I. Petrov, J.E. Greene, "Thermally induced self-hardening of nanocrystalline Ti–B–N thin films," J Appl Phys, **100** (2006)

[166] P. Karvankova, M.G.J. Veprek-Heijman, O. Zindulka, A. Bergmaier, S. Veprek, "Superhard *nc*-TiN/*a*-BN and *nc*-TiN/*a*-TiB_x/*a*-BN coatings prepared by plasma CVD and PVD: a

comparative study of their properties," Surf Coat Tech, **163–164** (2003) 149.

[167] B.A. Cook, J.L. Harringa, T.L. Lewis, A.M. Russell, "A new class of ultra-hard materials based on $AlMgB_{14}$," Scripta Mater, **42** (2000) 597.

[168] C. Yan, Z.F. Zhou, Y.M. Chong, C.P. Liu, Z.T. Liu, I. Bello, O. Kutsay, J.A. Zapien, W.J. Zhang, "Synthesis and characterization of hard ternary AlMgB composite films prepared by sputter deposition," Thin Solid Films, **518** (2010) 5372.

[169] C. Yan, J.C. Qian, T.W. Ng, Z.F. Zhou, K.Y. Li, W.J. Zhang, I. Bello, L. Martinu, J.E. Klemberg-Sapieha, "Sputter deposition of hard quaternary Al–Mg–B–Ti nanocomposite films," Surf Coat Tech, **232** (2013) 535.

[170] A.Y. Liu, R.M. Wentzcovitch, M.L. Cohen, "Atomic arrangement and electronic structure of BC_2N," Phys Rev B, **39** (1989) 1760.

[171] H. Sun, S.-H. Jhi, D. Roundy, M.L. Cohen, S.G. Louie, "Structural forms of cubic BC_2N," Phys Rev B, **64** (2001) 094108.

[172] V.L. Solozhenko, D. Andrault, G. Fiquet, M. Mezouar, D.C. Rubie, "Synthesis of superhard cubic BC_2N," Appl Phys Lett, **78** (2001) 1385.

[173] Y. Zhang, H. Sun, C. Chen, "Superhard Cubic BC_2N Compared to Diamond," Phys Rev Lett, **93** (2004) 195504.

[174] Z.F. Zhou, I. Bello, M.K. Lei, K.Y. Li, C.S. Lee, S.T. Lee, "Synthesis and characterization of boron carbon nitride films by radio frequency magnetron sputtering," Surf Coat Tech, **128–129** (2000) 334.

[175] E. Byon, J.-K. Kim, S. Lee, J.-H. Hah, K. Sugimoto, "Mechanical properties of B-C-N films deposited by dual cesium ion beam sputtering system," Surf Coat Tech, **169–170** (2003) 340.

[176] F.C. Jia, C.Q. Zhuang, C.Y. Guan, J.J. Zhao, Y.Z. Bai, X. Jiang, "Preparation of B-C-N films by magnetron sputtering with different N_2/Ar flow ratio," Vacuum, **85** (2011) 887.

[177] L. Filipozzi, A. Derre, J. Conard, L. Piraux, A. Marchand, "Local order and electrical properties of boron carbonitride films," Carbon, **33** (1995) 1747.

[178] S. Ulrich, H. Ehrhardt, T. Theel, J. Schwan, S. Westermeyr, M. Scheib, P. Becker, H. Oechsner, G. Dollinger, A. Bergmaier, "Phase separation in magnetron sputtered superhard BCN thin films," Diam Relat Mater, **7** (1998) 839.

[179] A. Lousa, J. Esteve, S. Muhl, Martı, amp, x, E. nez, "BCN thin films near the B_4C composition deposited by radio frequency magnetron sputtering," Diam Relat Mater, **9** (2000) 502.

[180] R. Gago, I. Jimenez, J.M. Albella, L.J. Terminello, "Identification of ternary boron-carbon-

nitrogen hexagonal phases by x-ray absorption spectroscopy," Appl Phys Lett, **78** (2001) 3430.

[181] T. Yuki, S. Umeda, T. Sugino, "Electrical and optical characteristics of boron carbon nitride films synthesized by plasma-assisted chemical vapor deposition," Diam Relat Mater, **13** (2004) 1130.

[182] M.O. Watanabe, S. Itoh, K. Mizushima, T. Sasaki, "Electrical properties of BC_2N thin films prepared by chemical vapor deposition," J Appl Phys, **78** (1995) 2880.

[183] M.O. Watanabe, S. Itoh, T. Sasaki, K. Mizushima, "Visible-light-emitting layered BC_2N semiconductor," Phys Rev Lett, **77** (1996) 187.

[184] G. Bräuer, B. Szyszka, M. Vergöhl, R. Bandorf, "Magnetron sputtering – Milestones of 30 years," Vacuum, **84** (2010) 1354.

[185] W.D. Sproul, D.J. Christie, D.C. Carter, "Control of reactive sputtering processes," Thin Solid Films, **491** (2005) 1.

[186] Y. Leng, Materials Characterization: Introduction to Microscopic and Spectroscopic Methods, Wiley, 2008.

[187] P. Hendra, C. Jones, G. Warnes, Fourier transform Raman spectroscopy: instrumentation and chemical applications, Ellis Horwood, 1991.

[188] "Instrument X-ray Optics: I. Reflection Geometry," Available: http://pd.chem.ucl.ac.uk/pdnn/inst1/optics1.htm

[189] A. Fischer-Cripps, Nanoindentation Testing, in: Nanoindentation, Springer New York, 2011, 21.

[190] W.C. Oliver, G.M. Pharr, "An improved technique for determining hardness and elastic modulus using load and displacement sensing indentation experiments," J Mater Res, **7** (1992) 1564.

[191] J. Musil, F. Kunc, H. Zeman, H. Poláková, "Relationships between hardness, Young's modulus and elastic recovery in hard nanocomposite coatings," Surf Coat Tech, **154** (2002) 304.

[192] V. Domnich, Y. Gogotsi, M. Trenary, T. Tanaka, "Nanoindentation and Raman spectroscopy studies of boron carbide single crystals," Appl Phys Lett, **81** (2002) 3783.

[193] H. Werheit, "On the influence of the atomic ratio of boron to carbon on the phonon energies and the electronic properties of boron carbide," Journal of the Less Common Metals, **67** (1979) 143.

[194] I. Bar, D. Zemsky, R. Shneck, P.J. Dagdigian, "Structure and morphology of pulsed laser deposited boron carbide films: Influence of deposition geometry," J Appl Phys, **102** (2007)

[195] J. Podder, M. Rusop, T. Soga, T. Jimbo, "Boron doped amorphous carbon thin films grown by r.f. PECVD under different partial pressure," Diam Relat Mater, **14** (2005) 1799.

[196] O. Postel, J. Heberlein, "Deposition of boron carbide thin film by supersonic plasma jet CVD with secondary discharge," Surf Coat Tech, **108** (1998) 247.

[197] H.Y. Chen, J. Wang, H. Yang, W.Z. Li, H.D. Li, "Synthesis of boron carbide films by ion beam sputtering," Surf Coat Tech, **128** (2000) 329.

[198] H.S. Ahn, P.D. Cuong, K.H. Shin, K.S. Lee, "Tribological behavior of sputtered boron carbide coatings and the influence of processing gas," Wear, **259** (2005) 807.

[199] T. Eckardt, K. Bewilogua, G. van der Kolk, T. Hurkmans, T. Trinh, W. Fleischer, "Improving tribological properties of sputtered boron carbide coatings by process modifications," Surf Coat Tech, **126** (2000) 69.

[200] M. Azzi, M. Paquette, J.E. Klemberg-Sapieha, L. Martinu, in: the 52th annual SVC conference, Society of Vacuum Coaters, Santa-Clara USA., 2009.

[201] O. Conde, A.J. Silvestre, J.C. Oliveira, "Influence of carbon content on the crystallographic structure of boron carbide films," Surf Coat Tech, **125** (2000) 141.

[202] R.M. Mohanty, K. Balasubramanian, S.K. Seshadri, "Multiphase formation of boron carbide in B2O3–Mg–C based micropyretic process," J Alloy Compd, **441** (2007) 85.

[203] K. Yamamoto, M. Keunecke, K. Bewilogua, Z. Czigany, L. Hultman, "Structural features of thick c-boron nitride coatings deposited via a graded B-C-N interlayer," Surf Coat Tech, **142** (2001) 881.

[204] B. Todorovi-Markovic, I. Draganic, D. Vasiljevic-Radovic, N. Romcevic, M. Romcevic, M. Dramicanin, Z. Markovic, "Synthesis of amorphous boron carbide by single and multiple charged boron ions bombardment of fullerene thin films," Appl Surf Sci, **253** (2007) 4029.

[205] A.C. Ferrari, J. Robertson, "Interpretation of Raman spectra of disordered and amorphous carbon," Phys Rev B, **61** (2000) 14095.

[206] H. Neuhauser, U. Harms, M. Gaertner, A. Schutze, K. Bewilogua, "Elastic and anelastic properties, internal stress and thermal expansion coefficient of cubic boron nitride films on silicon," Thin Solid Films, **385** (2001) 275.

[207] W. Cermignani, T.E. Paulson, C. Onneby, C.G. Pantano, "Synthesis and characterization of boron-doped carbons," Carbon, **33** (1995) 367.

[208] S. Jacques, A. Guette, X. Bourrat, F. Langlais, C. Guimon, C. Labrugere, "LPCVD and characterization of boron-containing pyrocarbon materials," Carbon, **34** (1996) 1135.

[209] C. Ronning, D. Schwen, S. Eyhusen, U. Vetter, H. Hofsäss, "Ion beam synthesis of boron carbide thin films," Surf Coat Tech, **158–159** (2002) 382.

[210] S. Vepřek, A.S. Argon, "Mechanical properties of superhard nanocomposites," Surf Coat Tech, **146** (2001) 175.

[211] R.F. Zhang, S.H. Sheng, S. Vepřek, "Stability of Ti-B-N solid solutions and the formation of nc-TiN/a-BN nanocomposites studied by combined ab initio and thermodynamic calculations," Acta Mater, **56** (2008) 4440.

[212] P. Jedrzejowski, A. Amassian, E. Bousser, J.E. Klemberg-Sapieha, L. Martinu, "Real-time in situ growth study of TiN- and TiCxNy-based superhard nanocomposite coatings using spectroscopic ellipsometry," Appl Phys Lett, **88** (2006)

[213] P. Karvankova, M.G.J. Vepřek-Heijman, D. Azinovic, S. Vepřek, "Properties of superhard nc-TiN/a-BN and nc-TiN/a-BN/a-TiB2 nanocomposite coatings prepared by plasma induced chemical vapor deposition," Surf Coat Tech, **200** (2006) 2978.

[214] F. Thévenot, "Boron carbide—A comprehensive review," J Eur Ceram Soc, **6** (1990) 205.

[215] J.C. Qian, Z.F. Zhou, C. Yan, D.J. Li, K.Y. Li, S. Descartes, R. Chromik, W.J. Zhang, I. Bello, L. Martinu, J.E. Klemberg-Sapieha, "Tailoring the mechanical and tribological properties of sputtered boron carbide films via the $B_{1-x}C_x$ composition," Surf Coat Tech, **267** (2015) 2.

[216] J.C. Sánchez-López, M.D. Abad, A. Justo, R. Gago, J.L. Endrino, A. García-Luis, M. Brizuela, "Phase composition and tribomechanical properties of Ti–B–C nanocomposite coatings prepared by magnetron sputtering," J Phys D: Appl Phys, **45** (2012) 375401.

[217] Y.H. Lu, Y.G. Shen, Z.F. Zhou, K.Y. Li, "Effects of nitrogen content on microstructure and oxidation behaviors of Ti–B–N nanocomposite thin films," J Vac Sci Technol A, **24** (2006) 340.

[218] C.D. Wagner, G.E. Muilenberg, Handbook of x-ray photoelectron spectroscopy, Physical Electronics Division, Perkin-Elmer Corp., 1979.

[219] T.D. Shen, C.C. Koch, T.Y. Tsui, G.M. Pharr, "On the elastic moduli of nanocrystalline Fe, Cu, Ni, and Cu–Ni alloys prepared by mechanical milling/alloying," J Mater Res, **10** (1995) 2892.

[220] F. Lofaj, T. Moskalewicz, G. Cempura, M. Mikula, J. Dusza, A. Czyrska-Filemonowicz, "Nanohardness and tribological properties of nc-TiB2 coatings," J Eur Ceram Soc, **33** (2013) 2347.

[221] Y. Sun, "Tribological rutile-TiO2 coating on aluminium alloy," Appl Surf Sci, **233** (2004) 328.

[222] M.O. Watanabe, S. Itoh, K. Mizushima, T. Sasaki, "Bonding characterization of BC2N thin films," Appl Phys Lett, **68** (1996) 2962.

[223] M. Kawaguchi, T. Kawashima, T. Nakajima, "Syntheses and Structures of New Graphite-

like Materials of Composition BCN(H) and BC3N(H)," Chem Mater, **8** (1996) 1197.

[224] H. Sota, C. Kimura, H. Aoki, T. Sugino, "Influence of atomic bonds on electrical property of boron carbon nitride films synthesized by remote plasma-assisted chemical vapor deposition," Diam Relat Mater, **19** (2010) 1441.

[225] Q. Yang, C.B. Wang, S. Zhang, D.M. Zhang, Q. Shen, L.M. Zhang, "Effect of nitrogen pressure on structure and optical properties of pulsed laser deposited BCN thin films," Surf Coat Tech, **204** (2010) 1863.

[226] H. Aoki, T. Masuzumi, M. Hara, D. Watanabe, C. Kimura, T. Sugino, "Effect of the radio-frequency power on the dielectric properties of hydrogen-containing boron carbon nitride films deposited by plasma-assisted chemical vapor deposition using tris(dimethylamino)boron gas," Thin Solid Films, **518** (2010) 2102.

[227] H. Ahn, L. Alberts, J. Wöhle, K.T. Rie, "Transparent BCN coatings by RF PACVD at low temperature using metallo-organic precursors," Surf Coat Tech, **142–144** (2001) 894.

[228] M. Watanabe, K. Mizushima, S. Itoh, M. Mashita, "Semiconductor device using semiconductor BCN compounds," US5895938 A, 1999.

[229] N.C. Anthony, B.B. Ravi, B. Snjezana, I.B. Jennifer, P.A. Dowben, "The heteroisomeric diode," J Phys: Condens Matter, **16** (2004) L139.

[230] G.D. Yuan, W.J. Zhang, J.S. Jie, X. Fan, J.X. Tang, I. Shafiq, Z.Z. Ye, C.S. Lee, S.T. Lee, "Tunable n-Type Conductivity and Transport Properties of Ga-doped ZnO Nanowire Arrays," Adv Mater, **20** (2008) 168.

[231] C. Levy-Clement, R. Tena-Zaera, M.A. Ryan, A. Katty, G. Hodes, "CdSe-Sensitized p-CuSCN/nanowire n-ZnO heterojunctions," Adv Mater, **17** (2005) 1512.

[232] S.K. Jha, C. Luan, C.H. To, O. Kutsay, J. Jaroslav KovaC, J.A. Zapien, I. Bello, S.T. Lee, "ZnO-nanorod-array/p-GaN high-performance ultra-violet light emitting devices prepared by simple solution synthesis," Appl Phys Lett, **101** (2012) 211116.

[233] M. Law, L.E. Greene, J.C. Johnson, R. Saykally, P.D. Yang, "Nanowire dye-sensitized solar cells," Nat Mater, **4** (2005) 455.

[234] C.P. Liu, Z.H. Chen, H.E. Wang, S.K. Jha, W.J. Zhang, I. Bello, J.A. Zapien, "Enhanced performance by incorporation of zinc oxide nanowire array for organic-inorganic hybrid solar cells," Appl Phys Lett, **100** (2012) 243102.

[235] S.K. Jha, O. Kutsay, I. Bello, S.T. Lee, "ZnO nanorod based low turn-on voltage LEDs with wide electroluminescence spectra," J Lumin, **133** (2013) 222.

[236] M. Law, L.E. Greene, J.C. Johnson, R. Saykally, P. Yang, "Nanowire dye-sensitized solar cells," Nat Mater, **4** (2005)

[237] X.M. Yang, X.M. Wu, L.J. Zhuge, F. Zhou, "Influence of assisted ion energy on surface roughness and mechanical properties of boron carbon nitride films synthesized by DIBSD," Appl Surf Sci, **255** (2009) 4279.

[238] H. Ling, J.D. Wu, J. Sun, W. Shi, Z.F. Ying, F.M. Li, "Electron cyclotron resonance plasma-assisted pulsed laser deposition of boron carbon nitride films," Diam Relat Mater, **11** (2002) 1623.

[239] E. Ech-chamikh, A. Essafti, Y. Ijdiyaou, M. Azizan, "XPS study of amorphous carbon nitride (a-C:N) thin films deposited by reactive RF sputtering," Sol Energ Mat Sol C, **90** (2006) 1420.

[240] D. Marton, K.J. Boyd, A.H. Al-Bayati, S.S. Todorov, J.W. Rabalais, "Carbon Nitride Deposited Using Energetic Species: A Two-Phase System," Phys Rev Lett, **73** (1994) 118.

[241] M.O. Watanabe, T. Sasaki, S. Itoh, K. Mizushima, "Structural and electrical characterization of BC2N thin films," Thin Solid Films, **281–282** (1996) 334.

[242] S. Jha, J.C. Qian, O. Kutsay, J. Kovac, C.Y. Luan, J.A. Zapien, W.J. Zhang, S.T. Lee, I. Bello, "Violet-blue LEDs based on p-GaN/n-ZnO nanorods and their stability," Nanotechnology, **22** (2011) 8.

[243] L. Schmidt-Mende, J.L. MacManus-Driscoll, "ZnO – nanostructures, defects, and devices," Materials Today, **10** (2007) 40.

[244] Y. Gong, T. Andelman, G. Neumark, S. O'Brien, I. Kuskovsky, "Origin of defect-related green emission from ZnO nanoparticles: effect of surface modification," Nanoscale Res Lett, **2** (2007) 297.

[245] N. Bano, I. Hussain, O. Nur, M. Willander, P. Klason, "Study of Radiative Defects Using Current-Voltage Characteristics in ZnO Rods Catalytically Grown on 4H-p-SiC," J Nano Mat, **2010** (2010)

[246] H.C. Casey, J. Muth, S. Krishnankutty, J.M. Zavada, "Dominance of tunneling current and band filling in InGaN/AlGaN double heterostructure blue light‐emitting diodes," Appl Phys Lett, **68** (1996) 2867.

[247] J.M. Shah, Y.L. Li, T. Gessmann, E.F. Schubert, "Experimental analysis and theoretical model for anomalously high ideality factors ($n \gg 2.0$) in AlGaN/GaN p-n junction diodes," J Appl Phys, **94** (2003) 2627.